
Experimental Investigation of Wind Farm Effects using Model Wind Turbines

Jannik Schottler

Von der Fakultät für Mathematik und Naturwissenschaften
der Carl von Ossietzky Universität Oldenburg
zur Erlangung des Grades und Titels eines

DOKTORS DER NATURWISSENSCHAFTEN
DR. RER. NAT.

angenommene Dissertation

von Herrn Jannik Schottler
geboren am 12.05.1989 in Bad Segeberg



Gutachter: Prof. Dr. Joachim Peinke

Zweitgutachter: Prof. Dr. Raúl Bayoán Cal

Tag der Abgabe: 12.01.2018

Tag der Disputation: 21.03.2018

„Experience, the best teacher“

— Keith Edward Elam a.k.a. Guru
Above the Clouds, 1998

Contents

Abstract / Zusammenfassung	1
Preface	5
1 Introduction	9
2 Wind energy systems	11
2.1 Energy conversion	11
2.2 Control principles	13
2.3 Wind turbine wakes	14
3 Model wind turbine	19
3.1 Introduction	19
3.2 Turbine design	20
3.3 Load control	21
3.4 Characterization	23
3.5 Improvements and outlook	25
4 This thesis	29
4.1 Motivation for wind tunnel experiments	29
4.2 Summary and context of papers	30
4.3 Outlook and recommendations	31
PAPER 1:	
<i>On the impact of non-Gaussian wind statistics on wind turbines - an experimental approach</i>	35
1 Introduction	37
2 Atmospheric flows	38
3 Methods	41
3.1 Experimental setup	41
3.1.1 Wind tunnel and active grid	41
3.1.2 Model wind turbine	42
3.2 Data preprocessing	44
3.3 Choice of scales	45

4 Results	45
4.1 Inflow	45
4.2 Turbine reaction	47
5 Discussion	48
6 Conclusion	50
Appendices	51

PAPER 2:
Wind tunnel experiments on wind turbine wakes in yaw: Redefining the wake width **57**

1 Introduction	59
2 Method	61
2.1 Experimental methods	61
2.2 Wake center detection	63
2.3 Examined quantities	64
3 Results	65
3.1 The non-yawed wakes	65
3.2 Wakes during yaw-misalignment	70
4 Discussion	73
5 Conclusions	75
Appendices	76

PAPER 3:
Wind tunnel tests on controllable model wind turbines in yaw **83**

1 Introduction	85
2 Model wind turbines	86
2.1 Pitching Mechanism	86
2.2 Load Control	87
3 Experimental Setup	89
4 Results	90
5 Discussion	91
6 Conclusion and Future Work	92

PAPER 4:

<i>Brief Communications: On the influence of vertical wind shear on the combined power output of two model wind turbines in yaw</i>	95
1 Introduction	97
2 Methods	98
3 Results	98
4 Discussion and conclusion	99
A Software	105
A.1 Hierarchy	105
A.2 Data acquisition	105
A.3 State machine architecture & application	111
B Blade specifications	119
C Technical drawings	123
Acknowledgements / Danksagung	125
Curriculum	127
Erklärung	129
List of publications	131

Abstract

Wind farms are complex systems, entailing challenges for scientists and engineers: The turbines are subjected to atmospheric turbulence throughout their life time, whereas the interactions of turbulent wind conditions with the rotors are yet to be fully understood and need investigation. Next, the individual turbines in a wind farm arrangement interact through their wakes, which feature an increased turbulence level and a decreased mean wind velocity. The former is connected to loads and therewith to a turbine's life time, while the latter is directly linked to the energy yield. Thus, the so-called *wake effects* become a very important aspect in wind energy research. In recent years, concepts of active wake control strategies have been discussed throughout the research community, whereas a lateral wake deflection by intentional yaw misalignment gained great attention. In order to successfully apply this concept to future wind farms, a detailed understanding of wind turbine wakes, the effect of yaw misalignment and the impact on downstream turbines is needed. This work aims to contribute to the mentioned discussions by wind tunnel experiments using controllable model wind turbines, which were conducted in three different wind tunnels in Oldenburg, Germany and Trondheim, Norway. Therefore, two model turbines were developed and characterized, including control strategies. In a first experiment, an active grid was used to create two different inflow conditions, being nearly equal regarding mean wind velocities and turbulence intensities, but strongly different regarding two-point statistics. More precisely, one flow showed Gaussian distributed velocity increments, the other one strongly non-Gaussian, heavy-tailed increment probability density functions (PDFs). The impact on the model wind turbine was investigated. Thrust, torque and power data were analyzed, showing that the model turbine does not smooth out intermittency. Intermittent inflow is converted to similarly intermittent turbine data on all scales considered, reaching down to sub-rotor scales in space. Next, full-plane wake measurements were performed using Laser-Doppler-Anemometry (LDA) and two significantly different model wind turbines, isolating turbine specific effects. It was found that areas of intermittent flows surround the velocity deficit of a wake. Besides being deflected laterally, a wake's shape is deformed to a curled „kidney“ shape during yaw misalignment, whereas a vertical momentum transport could be observed that is dependent on the direction of yaw misalignment and rotor rotation. Ultimately, the effect of yaw misalignment on the power output of a two-turbine array was investigated. Firstly, the total power could be increased by yawing the upstream turbine. Additionally, it was shown that the downstream turbine's power and the total power of the array are both asymmetric with respect to the upstream turbine's angle of yaw misalignment. The reasons for this asymmetry were further investigated and could be linked to the vertical shear in the inflow, that interacts with the rotating wake.

Zusammenfassung

Windparks sind komplexe Systeme, die diverse Herausforderungen für Wissenschaftler und Ingenieure mit sich bringen: Windenergieanlagen sind während ihrer gesamten Lebenszeit atmosphärischer Turbulenz ausgesetzt, wobei die Interaktionen turbulenter Windfelder mit den Rotoren noch nicht gänzlich verstanden sind. Die individuellen Anlagen in einem Windpark interagieren durch deren Nachlaufströmungen, die sich durch erhöhte Turbulenz und eine vermindernde mittlere Strömungsgeschwindigkeit auszeichnen. Ersteres beeinflusst die Lasten und somit die Lebensdauer einer Windenergieanlage, letzteres ist direkt mit dem Leistungsertrag verknüpft. Somit sind die sogenannten *Windparkeffekte* aktuell enorm wichtige Aspekte der Windenergieforschung. In den letzten Jahren wurden unterschiedliche Ansätze zur aktiven Beeinflussung von Nachlaufströmungen in der Forschungsgemeinde verfolgt, wobei eine horizontale Ablenkung der Nachlaufströmung durch eine gezielte Gier-Fehlstellung des Rotors ein vielversprechendes Konzept darstellt. Um den Ansatz in zukünftigen Windparks erfolgreich umsetzen zu können, ist zunächst ein detailliertes Verständnis der Nachlaufströmungen, der Effekte einer Gier-Fehlstellung und die Auswirkungen auf im Nachlauf operierende Anlagen notwendig. Ziel dieser Arbeit ist es, einen Beitrag zu den beschriebenen Fragestellungen durch Windkanalexperimente mit regelbaren Modell-Windenergieanlagen zu leisten, die in drei verschiedenen Windkanälen in Oldenburg und Trondheim durchgeführt wurden. Hierzu wurden zwei Modell-Windenergieanlagen entwickelt, charakterisiert und Regelstrategien wurden entwickelt.

In einem ersten Experiment wurden zwei verschiedene Strömungen mittels eines aktiven Gitters erzeugt, mit nahezu identischen Mittelwerten und Turbulenzintensitäten der Windgeschwindigkeit, zugleich jedoch stark unterschiedlicher Zweipunktstatistiken. Eine Strömung wies eine Gauß'sche Verteilung von Geschwindigkeitsinkrementen auf, während die andere deutlich nicht-Gauß'sche, intermittente Inkrementverteilungen zeigte. Der jeweilige Einfluss auf eine Modell-Windenergieanlage wurde untersucht, wobei Schub-, Drehmoment- und Leistungsdaten analysiert wurden. Es konnte gezeigt werden, dass die Modellturbine die Intermittenzen nicht glättet oder filtert. Intermittente Einströmungen werden zu ähnlich intermittenden Anlagendaten konvertiert, und zwar auf allen untersuchten Skalen, bis hin zu räumlichen Skalen kleiner als der Rotordurchmesser. Als nächstes wurden Querschnitte von Nachlaufströmungen mittels Laser-Doppler-Anemometrie (LDA) hinter zweier grundsätzlich verschiedenen Modell-Windenergieanlagen vermessen, wodurch anlagenspezifische Effekte isoliert wurden. Es wurde gezeigt, dass ein ringförmiger Bereich stark intermitterter Strömung das Geschwindigkeitsdefizit einer Nachlaufströmung umgibt. Zusätzlich zur lateralen Ablenkung wird eine Nachlaufströmung bei Gier-Fehlstellung zu einer Bohnen- bzw. Nierenform verformt. Außerdem wurde ein vertikaler Momentumtransport festgestellt, der von der Rotationsrichtung des Rotors sowie der Richtung der Gier-Fehlstellung abhängt. Letztlich wurde der Einfluss einer Gier-Fehlstellung auf die Leistungsausbeute einer Konfiguration bestehend aus zwei Anlagenmodellen untersucht. Es wurde gezeigt, dass die Gesamtleistung durch Gieren gesteigert werden konnte. Des Weiteren ist die Leistung der im Nachlauf betriebenen Anlage, sowie die Gesamtleistung beider Anlagen asymmetrisch bezüglich des Gierwinkels des vorderen Rotors. Die Gründe hierfür wurden untersucht, wobei eine starke Abhängigkeit der Asymmetrie vom vertikalen Gradienten in der Einströmung gefunden wurde, der mit der rotierenden Nachlaufströmung interagiert.

Preface

This thesis consists of two parts. The first part introduces the general topic, introducing the basic concepts of wind energy, allowing the reader to follow this thesis. Within the scope of this work, two model wind turbines were developed along with the respective software for data acquisition and turbine control. Chapter 3 describes the technical aspects as well as the characterization of a single turbine. Chapter 4 motivates wind tunnel experiments, summarizes the papers this thesis consists of and puts them in context of the broader topic. Additionally, an outlook on future work and follow up questions is given.

The second part consists of the four papers presenting the scientific content of this thesis. Details about the software and further technical aspects are presented in the appendix.

Introduction

Chapter 1

Introduction

Wind as energy source had a significant impact on the development of human societies and civilization for centuries. Sail boats provided increased mobility that had great impact on exploration, trade and fishing. Wind pumps allowed for water access and irrigation in arid regions, making crop grow and animal farming possible. Wind mills were used to grind grain. Electricity generating wind turbines were introduced to the world in the late 19th century, when the first wind turbine of larger scale was installed in 1888 in Ohio, USA [1, 2]. Nowadays wind energy is the fastest growing energy source, reaching approximately 500 GW of globally installed capacity in 2016 at a growth rate of 12.5 %, whereas growth rates are significantly larger for offshore wind energy compared to onshore. Globally installed capacity is believed to exceed 700 GW by 2020 [3]. Despite this promising development, large numbers of scientific and engineering challenges are yet to be solved as summarized by von Kuik et al. [4], some of which being content of this thesis.

Wind turbines convert the kinetic energy in the wind to electrical energy. Generally, the electric power P is proportional to the third power of the wind velocity u , $P \propto u^3$. This simple relation shows that knowledge about the wind as source of energy is a key aspect when designing, understanding and improving modern wind turbines and wind energy utilization. First, having a profound knowledge of the expected wind speed distribution throughout a year allows for an estimation of the energy yield. However, „knowing the wind“ involves much more than estimating annual wind speed distributions. Modern wind turbines operate in the atmospheric boundary layer and are therewith exposed to atmospheric turbulence for an expected life time of 20 years and longer. Naturally, a detailed knowledge of the impact of certain wind characteristics on the rotors need to be understood. It is well-known that a correct description of turbulence is scale-dependent and not universal [5]. The smaller the scales considered, the more abnormal and significant wind fluctuations become, which is known as the intermittency problem. Which scales are of importance for the wind energy conversion process, and the extent to which those are transferred to turbines are key questions, which are currently discussed throughout the research community [4]. This question is addressed in **paper 1** of this thesis in an experimental study. To achieve an economic optimum and therewith minimize the cost of energy (COE), wind turbines are commonly installed in wind farms consisting of multiple turbines with a typical spacing of 4 to 7 rotor diameters, depending on the site. Although wind farm arrangements undoubtedly feature many advantages, the complex and challenging phenomenon of *wake effects* is introduced. Due to changing wind directions and the finite spacing between turbines, an interaction of the rotors through their wakes is inevitable, causing a great challenge for researchers and engineers. Further details about wake effects are described in Section 2.3.

This thesis aims to contribute to the ongoing challenge of improving the understanding of wind

energy utilization in wind farms. This includes the impact of atmospheric turbulence on wind turbines, the interaction of multiple turbines through their wakes and active methods to mitigate wake effects by means of active wake control strategies. Those aspects were investigated using model wind turbines in laboratory environments, which is motivated in Chapter 4. The experiments were performed in three different wind tunnels of varying size in Oldenburg, Germany and in Trondheim, Norway.

Bibliography

- [1] T. Burton, D. Sharpe, N. Jenkins, and E. Bossanyi. *Wind Energy Handbook*. John Wiley and Sons, 2001.
- [2] J. K. Kaldellis and D. Zafirakis. The wind energy (r)evolution: A short review of a long history. *Renewable Energy*, 36(7):1887–1901, 2011.
- [3] G. W. E. Council. Global wind report 2016. *Brussels, Belgium*, 2016.
- [4] G. A. M. van Kuik, J. Peinke, R. Nijssen, D. Lekou, J. Mann, J. N. Sørensen, C. Ferreira, J. W. van Wingerden, D. Schlipf, P. Gebraad, H. Polinder, A. Abrahamsen, G. J. W. van Bussel, J. D. Sørensen, P. Tavner, C. L. Bottasso, M. Muskulus, D. Matha, H. J. Lindeboom, S. Degraer, O. Kramer, S. Lehnhoff, M. Sonnenschein, P. E. Sørensen, R. W. Künneke, P. E. Morthorst, and K. Skytte. Long-term research challenges in wind energy – a research agenda by the european academy of wind energy. *Wind Energy Science*, 1(1):1–39, 2016.
- [5] U. Frisch. *Turbulence : the legacy of A.N. Kolmogorov*, volume 1. Cambridge university press, 1995.

Chapter 2

Wind energy systems

This chapter introduces fundamentals of wind energy systems that are necessary for following this thesis. Various different concepts of wind turbines exist, differing in their axes' orientations, control approaches, number of blades and other aspects. This chapter does not aim to give a complete overview of design concepts and physical principles. Moreover, the background of this thesis is described. The focus hereby is on the to date most common wind turbine concept, being a three-bladed, horizontal axis machine, featuring a variable-speed and variable-pitch control system.

2.1 Energy conversion

Wind turbines convert energy from the wind, whereas the electric power is

$$P(u_\infty) = P_{air} \cdot c_P , \quad (2.1)$$

with

$$P_{air} = \frac{1}{2} \rho A u_\infty^3 . \quad (2.2)$$

The so-called power coefficient c_P expresses the efficiency of the machine, including all losses and physical limitations. ρ is the air density and A the swept area of the rotor. u_∞ refers to the apparent wind speed far upstream of the turbine. Using the actuator disc concept^a, the presence of the turbine is modeled by a disc extracting energy from the flow. Thereby, the velocity u_∞ is reduced to u_d at the disc's position. Downstream, the velocity is further reduced to u_w . Betz's momentum theory shows that the power coefficient has a theoretical maximum of $c_{P,max} = 16/27 \approx 0.59$, which occurs when $u_w/u_\infty = 1/3$ [3]. Following the Froude-Rankine-Theorem, the velocity at the rotor disc for optimal turbine operation according to Betz is

$$u_d = 2/3 \cdot u_\infty , \quad (2.3)$$

which is the velocity experienced by a rotor blade element interacting with the flow as described in the following.

Simply spoken, modern wind turbines consist of a finite number of aerodynamically shaped rotor blades, that experience lift forces when exposed to airflow in favorable conditions. Those result in a torque at the rotor shaft causing rotation. This mechanical power is ultimately converted

^aThe actuator disc concept is thoroughly described in text books such as [1] or [2]. The reader is referred to the primary literature.

to electricity by a generator. In simplified terms, rotor blades can be seen as concatenated two-dimensional airfoils. Those experience wind velocity components from the apparent wind speed at the rotor disc, which is $2/3 u_\infty$ according to Equation (2.3) and its rotational component $u_{rot} = \omega r$. Thus, the resulting velocity is u_{res} , as sketched in Figure 2.1. ω is the angular velocity of the blade and r the distance to the center of rotation. The drag force vector F_d acts in the direction of u_{res} , while the lift force F_l acts orthogonally. The sum of both force components is projected onto the plain of rotation, resulting in F_{rot} , inducing the torque on the rotor shaft and therewith rotation. An optimal rotor design maximizes the lift-to-drag ratio $F_l(\alpha)/F_d(\alpha)$, whereby both force components depend on the angle of attack α . As a result, an optimal rotor performance is achieved under constant angle of attack and thus a constant relation between the apparent wind velocity u_∞ and the rotational speed ω . To account for the dependence of α on the distance r , rotor blades are twisted, so that α is solely dependent on the ratio u_{rot}/u_∞ . At the rotor tips, where r is equal to the rotor radius R , this ratio becomes the tip speed ratio (TSR)

$$\lambda = \omega R / u_\infty , \quad (2.4)$$

which is commonly used in literature and throughout this thesis. As shown above, F_l and F_d are dependent on the apparent wind speed u_d and angle of attack α . Thus, properties of atmospheric turbulence such as changing wind velocities and directions directly affect the acting forces on rotor blades. Due to inertia, however, the angular velocity of the rotor cannot instantaneously follow fast velocity changes. How different turbulent inflow conditions affect a rotor on different time scales is further investigated in **paper 1**.

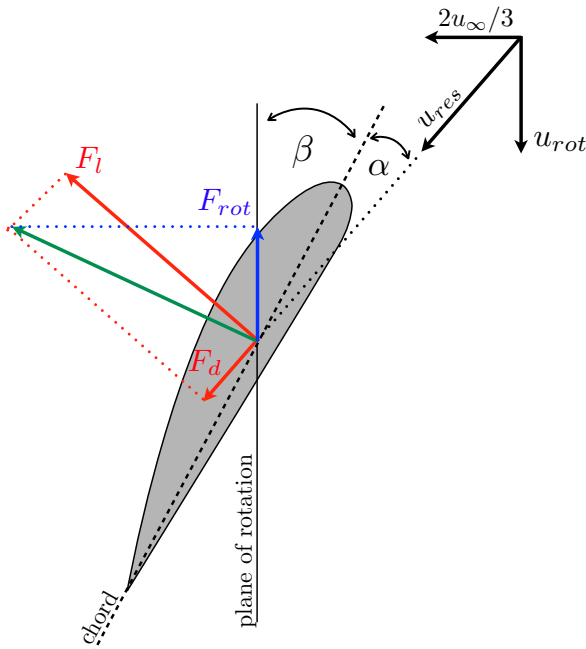


Figure 2.1: Schematic sketch of the forces acting on rotor blade element. α is the angle of attack and β the pitch angle.

2.2 Control principles

A very simple aspect of a wind turbine control system is the yaw controller. The objective is to align the turbine's rotation axis with the prevailing wind direction. The yaw angle γ denotes the misalignment of wind direction and turbine axis, so that the control objective is to keep $\langle \gamma(t) \rangle = 0^\circ$, $\langle \cdot \rangle$ denoting a mean value. Recent studies investigate active wake control strategies, where a turbine's yaw controller is used to deflect the velocity deficit behind the rotor laterally by an intentional yaw misalignment, $\gamma \neq 0^\circ$. The concept is introduced in Section 2.3. **Papers 2-4** investigate the wake deflection by yaw misalignment and its effect on downstream turbines.

Besides yawing, control objectives for operating a wind turbine vary with the apparent wind speed. Generally, a turbine generates power in the wind speed range $u_{cut-in} \leq u_\infty \leq u_{cut-out}$ as shown in Figure 2.2. Below the cut-in wind speed u_{cut-in} , the velocity is too low for power generation and/or the minimum rotor speed, that avoids certain eigenfrequencies, cannot be reached. The rotor is not in motion. Above the cut-out speed $u_{cut-out}$, aerodynamic and mechanical

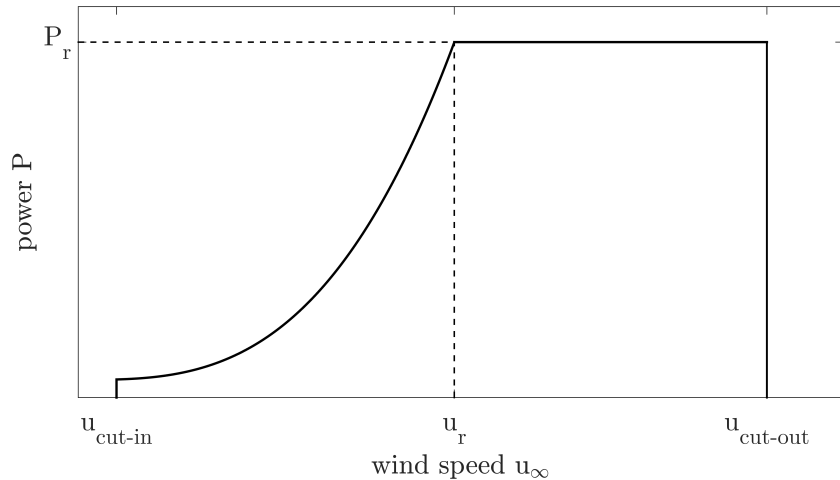


Figure 2.2: Typical power curve $P(u)$ of a modern wind turbine. P_r is the rated power that is generated at the rated wind velocity u_r . u_{cut-in} is the cut-in wind speed and $u_{cut-out}$ the cut-out speed, setting the operational range of a turbine.

safety mechanisms stop the turbine to prevent damage. The resulting range of operation can be divided in two regions. In the range $u_{cut-in} \leq u_\infty \leq u_r$, the control objective is the maximization of power. u_r is the rated wind speed, corresponding to the rated power of the turbine, P_r . As previously described, an optimal turbine operation is achieved at a constant angle of attack and thus at constant TSR. As R is a (turbine) constant and u_∞ is subject to change, the controller has to adapt the rotor's rotational speed ω to achieve a constant TSR, and therewith a constant angle of attack at the rotor blades. In the following, the principle of achieving this control objective is outlined, details are reported e.g. in [1] or [4].

Inserting Equation (2.4) in Equation (2.1) yields

$$P = \frac{1}{2} \rho A c_{P_{max}} R^3 \lambda_*^{-3} \omega^3 , \quad (2.5)$$

where λ_* is the TSR resulting in the maximum power coefficient, $c_{P_{max}}$. Since the aerodynamic torque applied to the rotor is

$$T_{aero} = P \omega^{-1} , \quad (2.6)$$

the rotor torque achieving λ_* and therewith $c_{P_{max}}$ becomes

$$T_{aero} = \underbrace{\frac{1}{2} \rho A R^3 c_{P_{max}} \lambda_*^{-3} \cdot \omega^2}_K . \quad (2.7)$$

In steady-state operation, the aerodynamic torque has to be balanced by the generator torque T_{gen} ,

$$T_{aero} - T_{gen} = 0 , \quad (2.8)$$

indicating that the total torque applied to the system becomes zero [1]. Thus, the desired generator torque is

$$T_{gen} = K \omega^2 , \quad (2.9)$$

with

$$K = \frac{1}{2} \rho A R^3 \lambda_*^{-3} c_{P_{max}} . \quad (2.10)$$

Equation (2.9) shows that the rotor speed ω is the only non-constant variable defining the desired generator torque necessary to optimize the aerodynamic performance, whereas K is a machine constant. Mechanical losses and an eventual gear box ratio are not included here for simplicity. The resulting block diagram of a variable-speed torque controller is shown schematically in Figure 2.3. Controller inputs are the rotational speed of the rotor and machine constants, including λ_* . In this simple form, the only manipulated variable is the generator torque T_{gen} . \dot{u} symbolizes wind speed changes over time that act as a disturbance input to the system. An implementation of the load control for the model wind turbines used in this thesis is described in Chapter 3.

For higher velocities, $u_r \leq u_\infty \leq u_{cut-out}$, the controller objective is to limit the power and

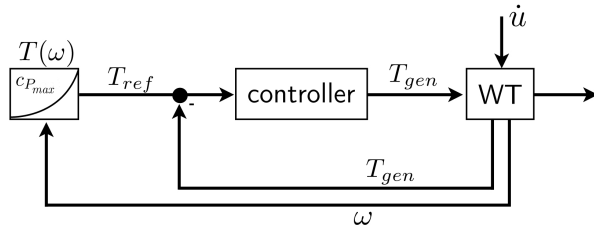


Figure 2.3: Schematic illustration of the load control principle for variable speed wind turbines. \dot{u} refers to changing inflow conditions acting as disturbance to the system.

therewith the rotational speed of the rotor so that $P = P_r$. This is achieved aerodynamically by pitching the rotor blades along the lateral axes, changing the pitch angle β . For the vast majority of modern wind turbines, pitching the blades „to feather“ decreases the angle of attack α and therewith the aerodynamic performance. Thus, the power coefficient is reduced to $c_P < c_{P_{max}}$ limiting the power output and the rotational speed. At $u \geq u_{cut-out}$, safety mechanism stop the turbine. The rotor blades are pitched to feather in order to minimize the acting forces. No power is generated, some turbine types stop the rotor by mechanical breaks.

The experimental implementation of the control strategies is described in Chapter 3.

2.3 Wind turbine wakes

Wind turbines extract kinetic energy from air flows. Naturally, this decreases the contained energy, changing the flow that passes through a wind turbine rotor. Downstream of the rotor, the

affected flow is called the *wake*. Generally, wind turbine wakes can be divided in two parts, near and far wake [5], which motivate different aspects of scientific interest. The near wake is the area in close proximity to the rotor, roughly up to one rotor diameter downstream. Here, the presence of the rotor itself determines the flow field. Thus, the number of blades, tip and root vortices as well as blade aerodynamics are of importance. Scientific interest in the near wake is mainly motivated by the power extraction process at the rotor and therewith its aerodynamic behavior and performance. The region beyond the near wake is the far wake, where the wake developed self-similarity, the velocity deficit is Gaussian-shaped and tip and root vortices have decayed [5]. Mainly, the interest in far wake properties arises from wake effects affecting downstream turbines in wind farm arrangements. Those include a velocity deficit and an increased turbulence intensity, which directly impact the energy yield and loads of downstream turbines. In order to understand the impact on energy yield, turbine longevity, layout optimization and thus the cost of energy, (far) wake models are of great importance. To date models vary in complexity, ranging from simple models as proposed by Jensen [6], assuming a linear wake expansion restricted to one flow component to more sophisticated models as proposed by Bastankhah and Porté-Agel [7, 8] or the FLORIS model [9], requiring a CFD (Computational Fluid Dynamics) based and/or experimental tuning and parametrization. Numerous studies and text books give a thorough overview of rotor wake aerodynamics and modeling methods (see e.g. [1, 5, 2]).

As mentioned in Chapter 1, wake effects are introduced due to the finite distance in wind farm layouts. Consequently, the (mostly far) wakes of rotors become the inflow conditions of further turbines, causing power losses and increased turbulence levels. As the wake is dependent on a turbine's performance, active wake control strategies allow for a manipulation of a wind turbine's wake by altering the operation point. One concept that gained much attention throughout the research community is the lateral wake deflection by an intentional yaw misalignment. By misaligning the rotation axis with the inflow, the thrust exerted by the rotor gains a horizontal component. The result of balancing this cross-wind component is a wake deflection as illustrated in Figure 2.4. To finalize this chapter, Figure 2.5 shows a aerial photograph of the Danish Horns Rev wind farm, where favorable meteorologic conditions make wind turbine wakes visible.

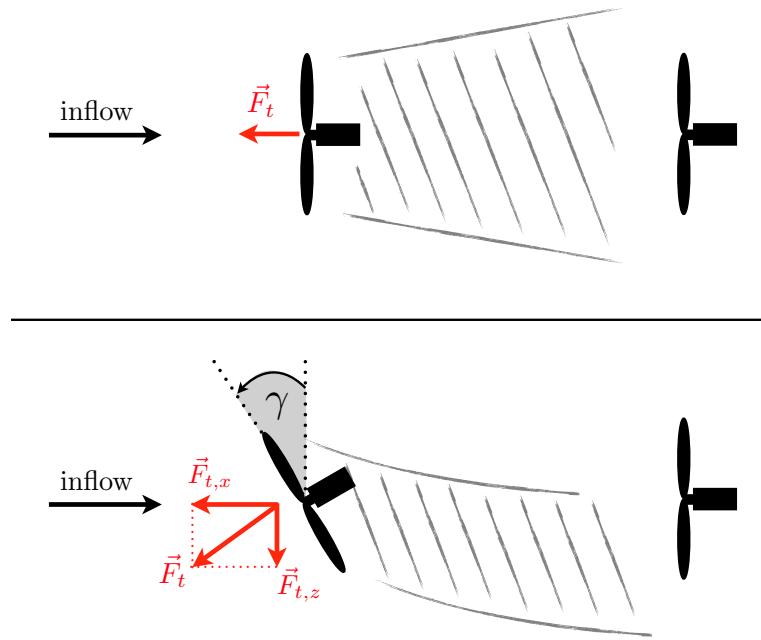


Figure 2.4: Principle illustration of the wake deflection during yaw misalignment, where F_t is the thrust force.



Figure 2.5: Aerial photograph of the Horns Rev wind farm in Denmark, taken on January 25th, 2016. Photo by Bel Air Aviation Denmark, permission granted.

Bibliography

- [1] T. Burton, D. Sharpe, N. Jenkins, and E. Bossanyi. *Wind Energy Handbook*. John Wiley and Sons, 2001.
- [2] J. F. Manwell, J. G. McGowan, and A. L. Rogers. *Wind energy explained: theory, design and application*. 2009.
- [3] A. Betz. Das maximum der theoretisch möglichen ausnützung des windes durch windmotoren. *Zeitschrift für das gesamte Turbinenwesen*, 26(307-309):8, 1920.
- [4] K. E. JOHNSON, L. Y. Pao, M. J. Balas, and L. J. E. E. J. FINGERSH. Control of Variable Speed Wind Turbines. *Ieee Control Systems Magazine*, 26(3):70–81, 2006.
- [5] L. Vermeer, J. N. Sørensen, and A. Crespo. Wind turbine wake aerodynamics. *Progress in aerospace sciences*, 39(6):467–510, 2003.
- [6] N. O. Jensen. A note on wind generator interaction, 1984.
- [7] M. Bastankhah and F. Porté-Agel. A new analytical model for wind-turbine wakes. *Renewable Energy*, 70:116–123, 2014.
- [8] M. Bastankhah and F. Porté-Agel. Experimental and theoretical study of wind turbine wakes in yawed conditions. *Journal of Fluid Mechanics*, 806(1):506–541, nov 2016.
- [9] P. M. O. Gebraad, F. W. Teeuwisse, J. W. van Wingerden, P. A. Fleming, S. D. Ruben, J. R. Marden, and L. Y. Pao. Wind plant power optimization through yaw control using a parametric model for wake effects-a CFD simulation study. *Wind Energy*, 19(1):95–114, jan 2014.

Chapter 3

Model wind turbine^a

This chapter describes the design and characteristics of the model wind turbines that were used for the experiments throughout this thesis^b. It presents a condensed version of the content published in [2], with minor alterations and additional sections.

3.1 Introduction

In order to meet the increasing need for scientific research in the field of wind energy, three different approaches can be distinguished. First, field measurements capture what actually happens in the real world, restricted to measurement limitations. However, costs are high, availability is limited and boundary conditions are subject to change and not controllable. Next, numeric simulations can give insight in further details. Since computational costs remain an issue, especially for high fidelity CFD simulations, not all scales can be resolved and a certain share of a problem needs to be modeled. This raises the question of validation of the results. As third approach, wind tunnel experiments allow an investigation of various effects in a controlled laboratory environment, complementing and validating field measurements and numeric simulations.

In recent years, model wind turbines of different sizes and designs were used to study various effects. The following outline lists some selected examples, without claims of completeness. For instance, in 2001 a two bladed turbine of 10 m rotor diameter, *Phase VI*, was tested in the NASA Ames wind tunnel [3]. The turbine was used in downwind and upwind configuration in order to investigate aerodynamic and structural effects. A 4.5 m diameter, three bladed turbine was used within the MEXICO project [4]. Amongst other aspects, up- and downstream induction, blade root bending moments and tip vortex trajectories were studied to establish a database for model improvement and validation. More recently, smaller models were tested in experiments focusing on several aspects. For instance, Medici and Alfredsson used a two bladed turbine of 0.18 m rotor diameter to investigate wake characteristics such as the wake's rotation and its deflection by yaw misalignment [5]. Further, wake meandering was investigated with varying blade numbers [6]. At the Norwegian University of Science and Technology (NTNU) in Trondheim, two models of 0.9 m rotor diameter are being used to study various aspects. For instance, Krogstad and Adaramola [7] investigated the general performance and near wake

^aTo a large part, this chapter is published as JANNIK SCHOTTLER, AGNIESZKA HÖLLING, JOACHIM PEINKE and MICHAEL HÖLLING: Design and implementation of a controllable model wind turbine for experimental studies, *Journal of Physics: Conference Series*. Vol. 753, 7, 72030, 2016.

^bAdditionally, a second model wind turbine designed by the Norwegian University of Science and Technology (NTNU) in Trondheim, Norway was used in **paper 2**. Details about the design are given in [1].

characteristics of a single turbine. Also, wake effects were studied in tandem configuration, quantifying power losses of a turbine operating in the wake of an upstream turbine [8], while Bartl et al. [9] examined wake properties of a two turbine array. In a boundary layer wind tunnel, Cal et al. [10] used a 3×3 array of models with a diameter of 0.12 m. Here, the vertical transport of momentum and kinetic energy was in focus. To isolate the effect of a fore-aft pitching motion, Rockel et al. investigated wake properties of fixed and oscillating model turbines of 0.2 m rotor diameter [11]. Similarly, this study was expanded to a tandem setup, where wake to wake interactions were examined [12]. Probably some of the most comprehensive model wind turbines are being used at the Politenico di Milano. With a rotor diameter of 2 m and active individual pitch and torque control, applications include aerodynamics, aeroelasticity and control [13].

3.2 Turbine design

Figure 3.1 shows a photograph of the three bladed, horizontal axis model wind turbine. At a rotor diameter of $D = 0.58$ m, the turbine features pitch and load controls, which are further described in Section 3.2 and 3.3. The nacelle, tower and foot of the turbine are made of aluminum. Acquiring thrust data is possible when placing the turbine on a force balance. Along with the pitching mechanism, the nacelle comprises a DC motor (*Faulhaber 3863H048CR*) used as generator, which is equipped with a two-channel magnetic encoder, resolving 4096 edges per revolution that allows for rotational velocity measurements. The generator torque T is proportional to the electric current I according to the generator's specifications [14], $T = k \cdot I$ with $k = 79.9 \text{ mN A}^{-1}$. I is obtained by measuring the voltage drop across a shunt resistor of $R_{sh} = 0.1 \Omega$, so that

$$T = k \cdot I = k \cdot \frac{U_{sh}}{0.1 \Omega} \quad (3.1)$$

and

$$P = T \cdot \omega . \quad (3.2)$$

The rotor blades are based on a SD7003 airfoil profile and were designed using the Blade Element Momentum (BEM) [15] method with Glauert optimization within the work of Odemark and Fransson [16], which lists further details on the blade design. The blades were manufactured by a vacuum casting method using a MG804 synthetic (isocyanate-polyol) compound. During the casting procedure, a T-shaped aluminum bolt is inserted at the blade root for fixation at the blade mountings.

Data acquisition and turbine control are realized by a *National Instruments cRIO-9074* real time controller. Analog and counter based data (rotational velocity) are being recorded fully synchronous, whereby two different sampling frequencies can be set. While analog data is typically recorded at $f_s \leq 10 \text{ kHz}$ (depending on the application), a trade-off between speed and



Figure 3.1: The model wind turbine.
Photo: Hendrik Heiselmann.

accuracy is necessary when measuring the rotational speed. Limiting the sampling rate of ω to 200 Hz gave satisfying results.

Pitching mechanism

The pitching of the blades is initiated by a stepper motor (*Faulhaber AM2224-R3-4.8-36*) equipped with an optical encoder for monitoring and closed-loop control. The shaft of the stepper motor is connected to a thread, whose counterpart is placed in a slider on the main shaft. The principle is adapted from a swash plate mechanism known from helicopter flight control. By rotating the motor shaft, a movement of the slider parallel to the main shaft is initiated, as sketched in Figure 3.2. Via joint links, this motion is transferred to a rotation of the blade mountings. This principle allows a collective pitching of the blades of $\Delta\beta \leq 30^\circ$, β being the blade pitch angle. A calibration of the pitching mechanism is achieved using a laser diode

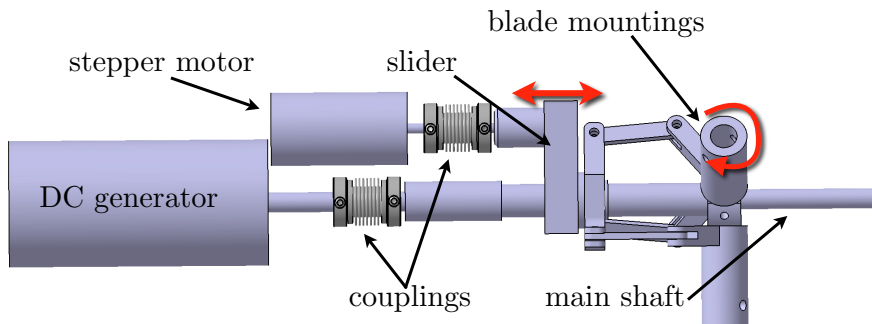


Figure 3.2: Working principle of the pitching mechanism.

mounted to a blade mounting. At a distance y to a screen normal to the rotor plane, a change in the stepper motor's angle in a variation of the length z , being the distance from the laser spot's original position on the screen to its location after a certain change in pitch. Therewith, a variation of the motor's shaft angle is related to a pitch angle alteration by

$$\Delta\beta = \arctan\left(\frac{z}{y}\right). \quad (3.3)$$

3.3 Load control

As described in Section 2.2, the generator torque is the controller output for the vast majority of model wind turbines. On the laboratory scale, however, the torque is not directly adjustable using small DC motors. The workaround solving this discrepancy is described in the following. The closed-loop load control of the model wind turbine is achieved using a field effect transistor (FET) within the electric circuit. By applying an external voltage U_{FET} to the transistor, the electric load is varied, thus controlling the torque. The closed-loop control is based on a reference velocity upstream of the rotor as the tip speed ratio (TSR) λ is the process variable of a PI-controller, and therewith the constant set point. The manipulative variable is the voltage U_{FET} , altering the torque. With this approach, the model turbine automatically reacts to changing inflow conditions, keeping its TSR constant, which allows convenient, time efficient and reproducible experiments. Figure 3.3 shows tests of the load control during step-like wind speed changes and constant pitch angle. The reference velocity u_{ref} , based on hot wire measurements

$2/3 D$ upstream of the rotor at hub height, is shown in red, which is used to calculate λ , the controller process variable. The turbine's reaction in terms of power, TSR and power coefficient $c_P^* = 2P/A\rho u_{ref}^3$ are shown for inactive (left column) and active (right column) torque control. u_{ref} is affected by the rotor's blockage, consequently, λ and c_P^* are biased similarly. The setup during the tests is sketched in Figure 3.4. Looking at the left column of Figure 3.3 (inactive control with constant U_{FET}), it becomes obvious that the model turbine cannot follow the sudden decrease in wind speed at $t \approx 15$ s, as the power, TSR and c_P^* drop to zero. When the wind speed increases again at $t \approx 40$ s, it takes roughly 35 s until the turbine data recovers to initial values. The right column of Figure 3.3 shows that, with active control, the model turbine follows the velocity changes with certain time lags and typical overshoots due to inflow dynamics and the anemometer placed upstream of the rotor. As expected, the TSR is kept constant, while the power follows the velocity pathway. As the power coefficient is based on hot wire data upstream of the rotor and the power, unphysical overshoots are observed, because the power and wind speed face a controller and distance caused time lag. Summarizing, Figure 3.3 shows that the described load control principle allows an automatic adaption of the turbine's point of operation during changing inflow conditions.

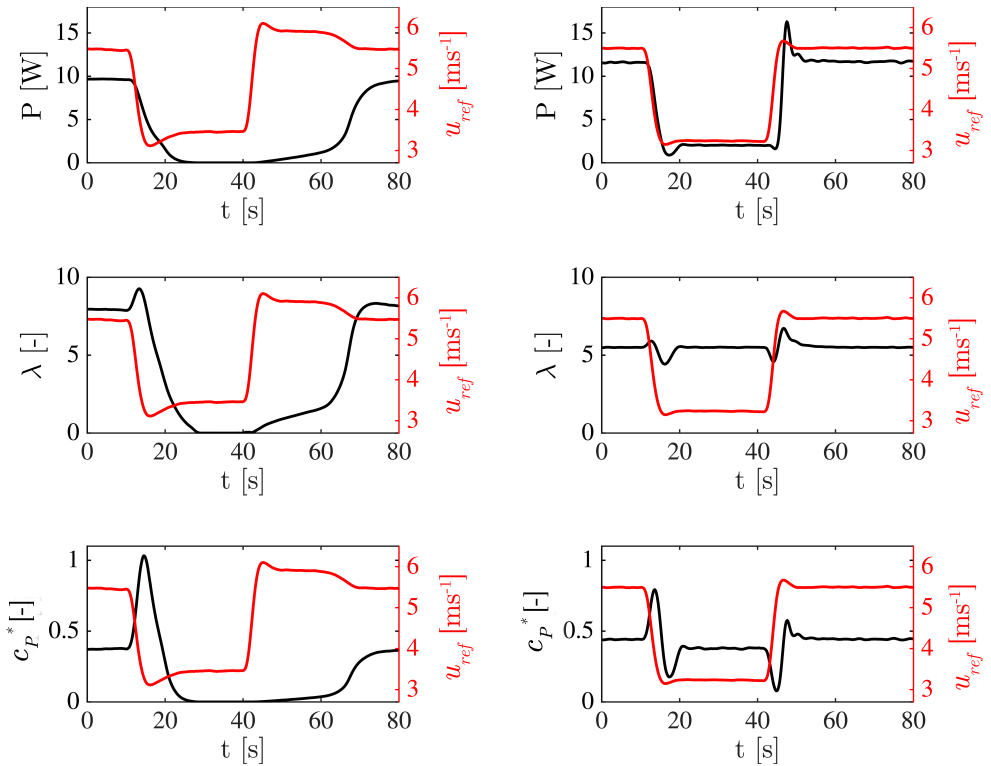


Figure 3.3: Tests of the load control during step-like velocity changes and constant pitch angle. The wind speed u_{ref} (red) is based on a hot wire probe $2/3 D$ upstream of the rotor. *Left column:* inactive control, with $U_{FET} = \text{const.} = 2.21 \text{ V}$. *Right column:* active control, with $\lambda_{set} = 5.5$.

3.4 Characterization

In this section, a characterization of the model turbine is described. The turbine was placed on a three component force balance (*ME-Systems K3D120-50N*) in order to record thrust data. Measurements were conducted in a wind tunnel of the University of Oldenburg with an outlet of $0.8 \text{ m} \times 1 \text{ m}$ (height \times width) in open jet configuration as sketched in Figure 3.4. Throughout

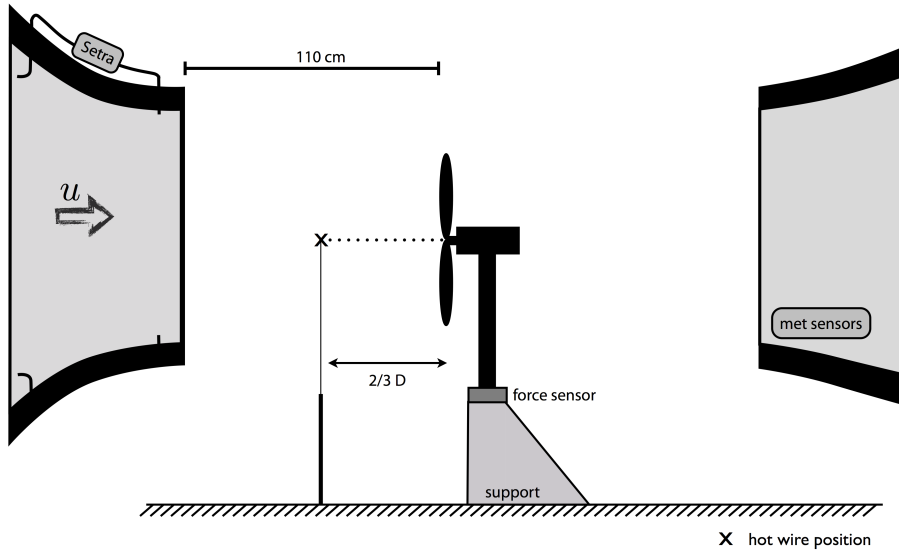


Figure 3.4: Experimental setup of the model turbine's characterization.

the following analysis, the inflow velocity u_∞ is defined by the rotational speed of the wind tunnel fan, resulting in a certain wind speed in the test section *without* the model turbine being installed. Prior to the experiments, the relation between the fan's rotation and the wind speed at the rotor's position without the turbine was determined by means of pressure measurements and used to define u_∞ during turbine operation. Accordingly, quantities depending on the wind speed are based on this velocity unless stated differently.

For characterizing of the model wind turbine, U_{FET} was systematically increased in steps of 5 mV for wind speeds ranging from $u_\infty \approx 4.3 \text{ m s}^{-1}$ to $u_\infty \approx 8.8 \text{ m s}^{-1}$. Increasing U_{FET} decreases the rotor speed and therewith the TSR until stall. For each configuration, data was recorded for 30 s at a sampling rate of $f_s = 2 \text{ kHz}$. A waiting time of 15 s between a change of U_{FET} ensured stationary operating conditions. Exemplary, Figure 3.5 shows the influence of varying U_{FET} on the torque for different wind speeds. Clearly, it can be seen that increasing the voltage applied to the FET is directly increasing the torque until stall of the turbine, which is the basis of the closed-loop control described in Section 3.3.

Next, Figure 3.6 shows the power coefficient $c_P = 2P/A\rho u_\infty^3$ and the thrust coefficient $c_T = 2F_x/A\rho u_\infty^2$ [15] over λ at constant pitch angle and $u_\infty \approx 8.3 \text{ m s}^{-1}$, whereas F_x is the thrust force in main flow direction, ρ the air density and A the swept area of the rotor. When increasing U_{FET} , the rotational speed and therewith λ and the thrust decrease, while the power increases until the maximal power coefficient is reached at $\lambda_{opt} \approx 5$, where $c_P = c_{P,max} \approx 29\%$. It should be noted that the absolute values of power are facing uncertainties due to the definition of the torque, cf. Eq. (3.1).

Based on the same measurements, $T - \omega$ curves for the examined wind speeds are obtained and shown in Figure 3.7. Values of maximal power coefficient are marked in red for each wind speed.

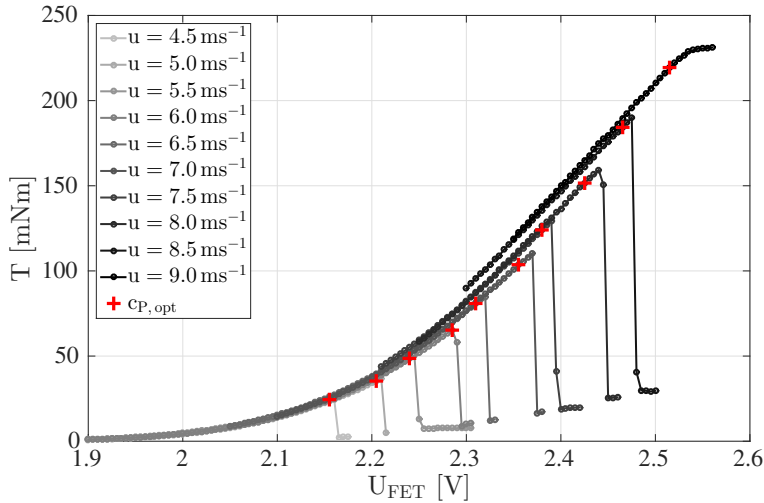


Figure 3.5: Mean torque values for increasing voltages U_{FET} for different inflow velocities, which are rounded to the next multiples of 0.5 m s^{-1} . Red crosses mark the maximal c_P for each wind speed.

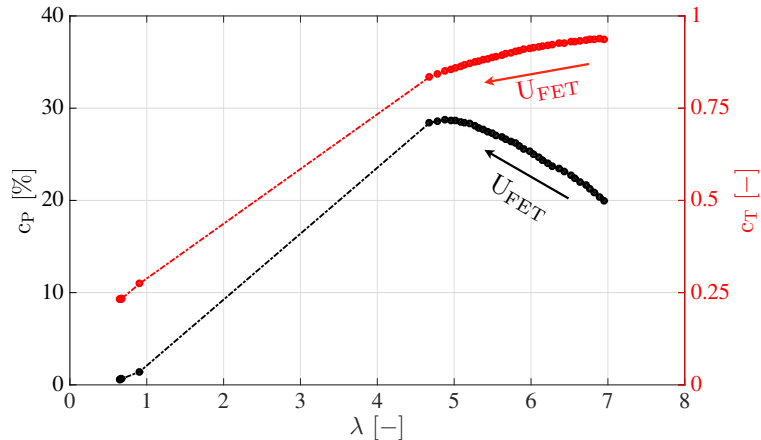


Figure 3.6: Power coefficient c_P (black) and thrust coefficient c_T (red) over TSR λ for $u_\infty \approx 8.3 \text{ m s}^{-1}$. The arrows indicate increasing values of U_{FET} during characterization.

The resulting curve, based on the $c_{P,max}$ values, is typically used for torque control strategies [15], which in principle is possible based on the present data. This approach, which does not require a reference wind speed as controller input, will be further pursued in future work in order to establish an alternative to the present concept described in Section 3.3. Especially when using multiple model turbines, e.g. for investigating wind farm effects, an automatic control without further measurements becomes beneficial. At the time of writing, this concept is realized and tested, which is further described in Section 3.5.

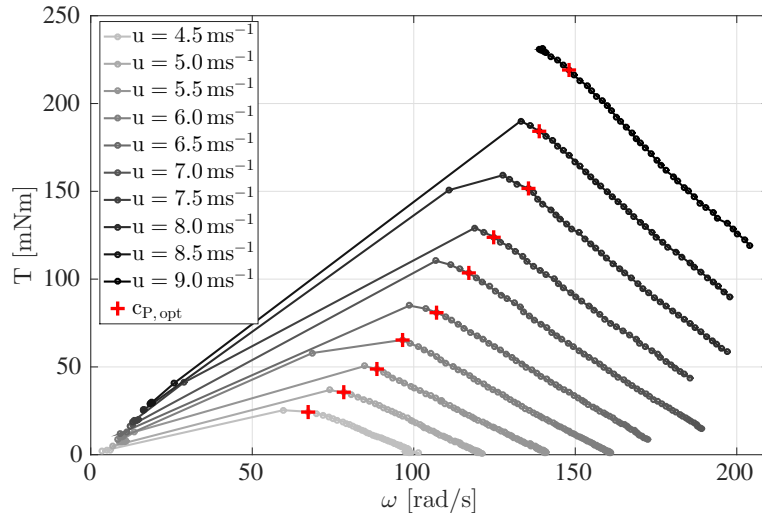


Figure 3.7: Mean values of torque and rotational velocity for different wind speeds. The red crossed indicate the values of maximal power coefficient. Velocity values in the legend are rounded to multiples of 0.5 m s^{-1} .

3.5 Improvements and outlook

This chapter describes the design, control and characteristics of the model wind turbines used within this thesis. At the time of writing, improvements of the load control principle were investigated and partially implemented, which are outlined here. This section is not part of the publication [2].

The load control system of the model turbine described in Section 3.3 was used through the experiments of this thesis and can be illustrated as done in Figure 3.8. This approach requires the apparent wind speed as controller input since the TSR is the process variable of the controller. Depending on the application, this can be beneficial: When studying wakes as done in **paper 2**, constant TSR during constant inflow velocity is a favorable condition, making the described approach very convenient. However, during changing inflow conditions and wind farm applications, a stand-alone system bears significant advantages, which has been implemented after the experiments described in this thesis were performed. The new approach is based on the turbine's characterization that needs to be recorded before using the controller. The characteristic $T(\omega)$ -curve maximizing the power for each wind speed investigated (cf. Figure 3.7) is used as a basis, whereas the data points are fitted with a polynomial function. Based on the $T(\omega)$ -fit, the current rotational speed defines a torque set point T_{set} , which is the process variable of a PID controller. Analogous to Figure 3.8, U_{FET} is the manipulative variable affecting the turbine. The main advantage is that this approach works totally independent of any sensors that are not part of the turbine's data acquisition system. The control is fully based on the operation conditions and the previously recorded characterization, Figure 3.9 shows the block diagram. Within the implementation of the concept, software was developed that automatically records the required data, fits a polynomial function and exports a characterization file. Figure A.5 shows a screen shot. The software used for turbine operation can simply import this file to use the implemented controller.

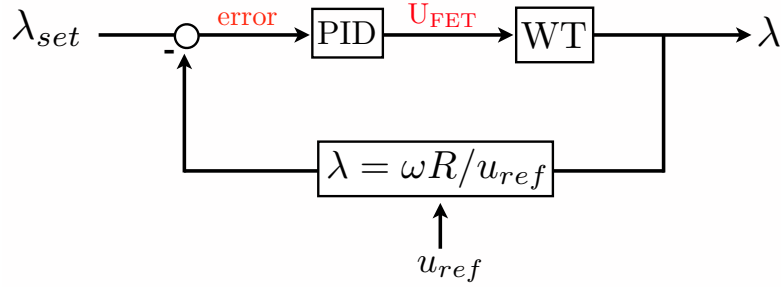


Figure 3.8: Principle block diagram of the load control used throughout this thesis.

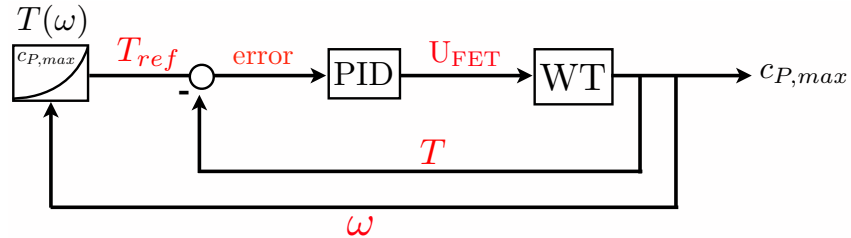


Figure 3.9: Principle block diagram of the stand-alone load control based on the turbine's characterization. The left block represents the characteristic $T - \omega$ curve.

The approach was successfully tested for the partial load region $u_{cut-in} \leq u_\infty \leq u_r$ while this thesis was written. In future work, the pitch control system has to be combined with the load control. Consequently, the characterization will have to be performed for various pitch angles so that the whole parameter space of wind speed, torque, rotational speed and pitch angles is covered in a combined controller. Furthermore, the design of the model turbines as described in Chapter 3 is being improved regarding minor mechanical issues. Most importantly, the pitching mechanism is redesigned, adding ball bearings in each blade mountings to minimize mechanical friction. For the same reason, the swash plate mechanism shown in Figure 3.2 is redesigned, replacing the slider with a linear ball screw. Sketches of the re-designed blade mountings and the improved pitching mechanism are shown in Figures 3.10 and 3.11. As another improvement of the pitching system, a closed loop pitch controller should be implemented on the real time system or the FPGA directly. Ultimately, the pitch controller should then be combined with the partial load controller, allowing for a stand alone turbine operation for all operational wind speeds.

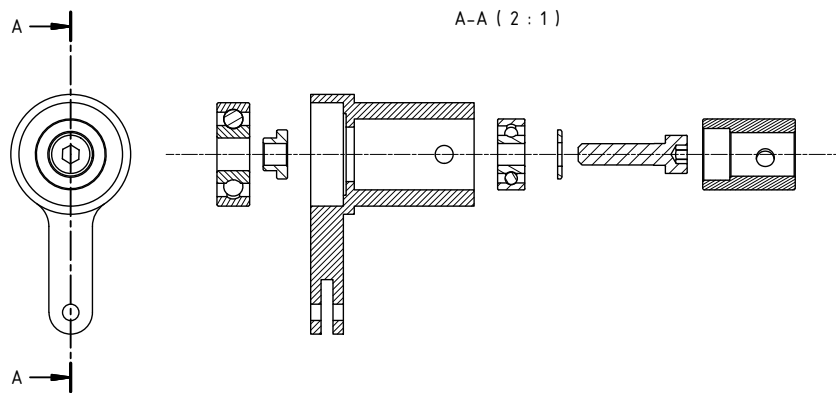


Figure 3.10: Technical sketch of the re-designed blade mountings, whereas mechanical friction during pitch actuation is minimized by two ball bearings.

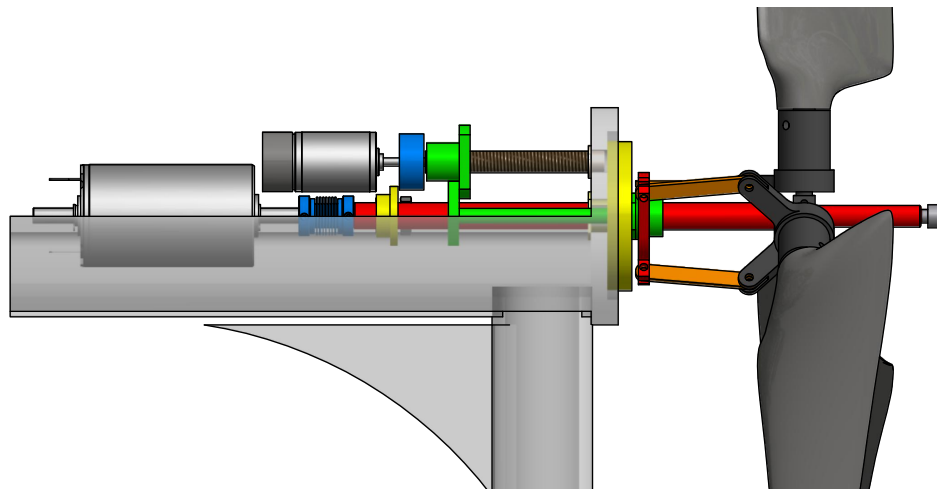


Figure 3.11: Visualization of the new pitching mechanism, whereas the swash plate is not based on a threat but on linear ball bearings and sliding supports shown in green.

Bibliography

- [1] J. Schottler, F. Mühle, J. Bartl, J. Peinke, M. S. Adaramola, L. Sætran, and M. Hölling. Comparative study on the wake deflection behind yawed wind turbine models. *Journal of Physics: Conference Series*, 854:012032, may 2017.
- [2] J. Schottler, A. Hölling, J. Peinke, and M. Hölling. Design and implementation of a controllable model wind turbine for experimental studies. *Journal of Physics: Conference Series*, 753:072030, sep 2016.
- [3] M. M. Hand, D. a. Simms, L. J. Fingersh, D. W. Jager, J. R. Cotrell, S. Schreck, and S. M. Larwood. Unsteady Aerodynamics Experiment Phase VI : Wind Tunnel Test Configurations and Available Data Campaigns. *Data Processing*, (July 2015):292.
- [4] J. G. Schepers and H. Snel. Model Experiments in Controlled Conditions - Final Report. *ECN Report: ECN-E-07-042*, page 54, 2008.

- [5] D. Medici and P. Alfredsson. Measurements on a wind turbine wake: 3d effects and bluff body vortex shedding. *Wind Energy*, 9(3):219–236, 2006.
- [6] D. Medici and P. H. Alfredsson. Measurements behind Model Wind Turbines: Further Evidence of Wake Meandering. *Wind Energy*, 11(October 2007):211–217, 2008.
- [7] P.-Å. Krogstad and M. S. Adaramola. Performance and near wake measurements of a model horizontal axis wind turbine. *Wind Energy*, 15(5):743–756, 2012.
- [8] M. Adaramola and P.-Å. Krogstad. Experimental investigation of wake effects on wind turbine performance. *Renewable Energy*, 36(8):2078–2086, 2011.
- [9] J. Bartl, F. Pierella, and L. Sætran. Wake measurements behind an array of two model wind turbines. *Energy Procedia*, 24(1876):305–312, 2012.
- [10] R. B. Cal, J. Lebrón, L. Castillo, H. S. Kang, and C. Meneveau. Experimental study of the horizontally averaged flow structure in a model wind-turbine array boundary layer. *Journal of Renewable and Sustainable Energy*, 2(1):013106, 2010.
- [11] S. Rockel, E. Camp, J. Schmidt, J. Peinke, R. B. Cal, and M. Hölling. *Experimental study on influence of pitch motion on the wake of a floating wind turbine model*, volume 7. 2014.
- [12] S. Rockel, J. Peinke, M. Hölling, and R. B. Cal. Wake to wake interaction of floating wind turbine models in free pitch motion: An eddy viscosity and mixing length approach. *Renewable Energy*, 85:666–676, 2016.
- [13] C. L. Bottasso, F. Campagnolo, and V. Petrović. Wind tunnel testing of scaled wind turbine models: Beyond aerodynamics. *Journal of Wind Engineering and Industrial Aerodynamics*, 127:11–28, 2014.
- [14] Online data sheet. Accessed 17.05.2016.
- [15] T. Burton, D. Sharpe, N. Jenkins, and E. Bossanyi. *Wind Energy Handbook*. John Wiley and Sons, 2001.
- [16] Y. Odemark and J. H. M. Fransson. The stability and development of tip and root vortices behind a model wind turbine. *Experiments in Fluids*, 54(9), 2013.

Chapter 4

This thesis

4.1 Motivation for wind tunnel experiments

A wind farm is a very complex system. Atmospheric turbulence and precipitation interact with wind turbines, rotors weighing multiple tens of tons rotate with an expected life time of decades and multiple machines interact through their wakes. From a scientific point of view, the exact situation within a wind farm or a certain component is of interest to gain an understanding of the prevailing phenomena, which can be aerodynamic, mechanic, electric or others. However, field measurements are not only costly but also make it very difficult to systematically study certain effects, as boundary conditions are subject to change and not controllable. Various limitations restrict the data availability. An alternative are numeric simulations. Those vary in complexity from simple models to complex CFD (computational fluid dynamics) simulations. Compared to field studies, CFD simulations offer a great flexibility, are comparatively inexpensive (financially) and allow for an isolated investigation of single parameters. However, finite computational power limits the applicability. Using Direct Numeric Simulations (DNS), the governing Navier-Stokes equations can be numerically solved for low Reynolds numbers

$$Re = \frac{u \cdot l}{\nu} , \quad (4.1)$$

where u is a typical velocity, l a typical length scale and ν the kinematic viscosity. However, as the computational costs are proportional to Re^3 [1], it is practically impossible to fully resolve all scales in a wind energy application. Consequently, a certain share has to be modeled. Naturally, turbulence models introduce an uncertainty relating reality to simulation results, which raises the question of validation. As third approach, wind tunnel experiments offer a flexible and inexpensive alternative when studying wind farm effects. Depending on the application, wind turbines are modeled on laboratory scale with varying complexity, ranging from non-rotating porous disc models as e.g. used in [2] or [3], to highly sensor-equipped models featuring advanced control systems as performed in [4]. The main advantages of wind tunnel experiments include the possibility to isolate certain parameters, reproducing situations and a large accessible parameter space. Despite the great flexibility, much smaller length scales cause a Reynolds number mismatch between experiments and full scale cases.^a Furthermore, most models are not aero elastically scaled making the question of upscaling a major drawback of wind tunnel tests using model wind turbines.

^aFew exceptions manage to increase the Reynolds number to be comparable to full scale cases by Miller et al. [5]. However, this involves large experimental challenges and costs.

4.2 Summary and context of papers

In this work, a wind farm is modeled in a simplistic way, using either a single model wind turbine or two aligned turbines. This model on laboratory scale is used to investigate different wind farm phenomena. Those include turbulent inflow conditions, wakes of wind turbines and the interaction of two turbines. This thesis consists of four papers that focus on one or more of the above aspects. Figure 4.1 shows a schematic sketch of the papers' context and the relation to the wind farm model. In the following, the contents of the papers are summarized.

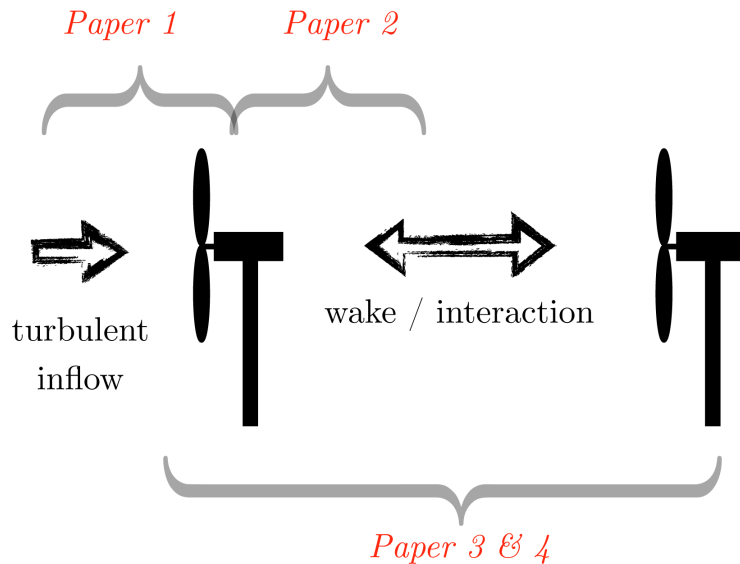


Figure 4.1: Sketch of the papers in the context of a simplified wind farm model consisting of two in-line turbines.

Paper 1 investigates the effect of turbulent inflow conditions on a wind turbine. Therefore, an active grid is used to create different turbulent flow conditions in a wind tunnel, to which the model wind turbine is exposed. Two inflow conditions were created that are nearly equal regarding their mean wind velocities and turbulent intensities, but strongly differ in the distribution of velocity increments. It is shown that the difference in the increment PDFs on sub-rotor scales is transferred to turbine data such as thrust, torque and power. The results suggest that heavy-tailed distributions of velocity increments are not smoothed out by the rotor, making those characteristics important for wind turbine designs, load simulations and grid stability.

Paper 2 examines the wakes behind two different model wind turbines during yaw misalignment angles of $\gamma = \{0^\circ, \pm 30^\circ\}$. Their wakes are compared, isolating effects of boundary conditions and turbine specifications. Laser Doppler Anemometry was used to scan a full plane of a wake normal to the main flow direction, 6 rotor diameters downstream of the respective turbine. The wakes of both turbines are compared in terms of the time averaged main flow component, the turbulent kinetic energy and the distribution of velocity increments. Areas of strongly heavy-tailed distributed velocity increments are found to surround the velocity deficit in all cases examined. Thus, a wake is significantly wider when including two-point statistics as opposed to a description limited to one-point quantities. As non-Gaussian distributions of velocity increments are believed to affect loads of downstream rotors as shown in **paper 1**, this finding impacts the application of active wake steering through yaw misalignment as well as wind farm layout optimization. Further, the velocity deficits behind both turbines are deformed to a kidney-

like curled shape during yaw misalignment, for which parameterization methods are introduced. Additionally, the lateral wake deflection during yaw misalignment is investigated.

In **paper 3**, the impact of yaw misalignment of a turbine three rotor diameters upstream of a second, in-line turbine was investigated. To do so, a partial load control was utilized by the downstream turbine, maximizing its power coefficient during changing inflow conditions. It was shown that the power of the downstream turbine and the total power of the array is asymmetric with respect to the upstream turbine's yaw angle. Further, the total power of the array could be increased by yaw misalignment of the upstream turbine.

Paper 4 investigates the reasons for the asymmetry in power found in **paper 3**, using a comparable setup. An active grid is used statically, creating two different shear flows, whereas the vertical orientation of the shears differ. The results show a strong linkage of the asymmetry in power and the sheared inflow, as the direction of the power asymmetry changed with the changing direction of vertical shear. It is believed that an interaction of the wake's rotation with the ground, the tower shadow and the vertical shear deflects the wakes differently for positive and negative angles of yaw misalignment. Similar effects have been observed in **paper 2** during wake measurements.

Authors contributions

Paper 1: J. Peinke, J. Whale and M. Hölling had a supervising function. A. Hölling designed the model wind turbine as well as the active grid. N. Reinke created the excitation protocol of the active grid that was used to create the „intermittent“ flow conditions. J. Schottler performed the scientific analyses and wrote the manuscript.

Paper 2: J. Peinke, M. Hölling and L. Sætran had a supervising function. J. Bartl, F. Mühlé and J. Schottler performed the experiments. J. Schottler performed the scientific analyses and wrote the manuscript.

Paper 3: J. Peinke and M. Hölling had a supervising function. A. Hölling designed the model wind turbine. J. Schottler performed the scientific analyses and wrote the manuscript.

Paper 4: J. Peinke and M. Hölling had a supervising function. A. Hölling designed the model wind turbine as well as the active grid. J. Schottler performed the scientific analyses and wrote the manuscript.

4.3 Outlook and recommendations

The model wind turbines used throughout this thesis proved to be a suitable tool for wind tunnel experiments investigating wind farm effects. The content shown in **papers 2-4** motivates further investigations of single turbine wakes and turbine-turbine interactions in wind farm arrangements. More precisely, wake measurements as done in **paper 2** should be performed for different downstream distances during more realistic inflow conditions. Especially the findings of areas featuring intermittent flow structures surrounding the velocity deficit of a wake should be investigated further. That is, during varying inflow conditions, turbine settings and downstream development. A systematic investigation should allow for a wake model development including the statistics of two point quantities.

The present setup of a two turbine array will be extended to a total of 9 model turbines in

the near future. At the time of writing, 7 new model turbines are being built within the project „Ventus Efficiens“. In combination with a new active grid based on the same principles as used in **paper 1**, this new model wind farm will allow for more realistic investigations of the turbines’ interactions, offering the opportunity to experimentally test wind farm control strategies discussed and developed throughout the research community. Also, the impact and development of realistic, turbulent inflow conditions on and within the model wind farm can be examined. This infrastructure could hence serve as test environment for various groups developing wind farm controls, offering a comparatively realistic setup relative to state of the art wind tunnel facilities.

The experiments described in **paper 1** show the model turbine’s response to different turbulent inflow conditions. Beyond the scope of the paper, the dependency of controller settings on the turbine’s response was investigated, showing that the developed methods offer the opportunity to further examine the controller dependency, of e.g. gust responses. The methodology and main idea of the experiment can further be transferred to an aero elastically scaled turbine model as built in Oldenburg in combination with the mentioned larger active grid. While repeating similar experiments as performed in **paper 1**, more information about tower and blade loads can be acquired, giving further insight in the impact of different turbulent inflows on a wind turbine.

Bibliography

- [1] J. H. Ferziger and M. Peric. *Numerische Strömungsmechanik*. Springer-Verlag, 2008.
- [2] G. España, S. Aubrun, S. Loyer, and P. Devinant. Wind tunnel study of the wake meandering downstream of a modelled wind turbine as an effect of large scale turbulent eddies. *Journal of Wind Engineering and Industrial Aerodynamics*, 101:24–33, 2012.
- [3] M. F. Howland, J. Bossuyt, L. A. Martínez-Tossas, J. Meyers, and C. Meneveau. Wake structure in actuator disk models of wind turbines in yaw under uniform inflow conditions. *Journal of Renewable and Sustainable Energy*, 8(4), 2016.
- [4] C. L. Bottasso, F. Campagnolo, and V. Petrović. Wind tunnel testing of scaled wind turbine models: Beyond aerodynamics. *Journal of Wind Engineering and Industrial Aerodynamics*, 127:11–28, 2014.
- [5] M. Miller, J. Kiefer, C. Westergaard, and M. Hultmark. Model Wind Turbines Tested at Full-Scale Similarity. *Journal of Physics: Conference Series*, 753:032018, sep 2016.

Papers

Paper 1

On the impact of non-Gaussian wind statistics on wind turbines – an experimental approach^a

JANNIK SCHOTTLER, NICO REINKE, AGNIESZKA HÖLLING, JONATHAN WHALE, JOACHIM PEINKE and MICHAEL HÖLLING

Abstract. The effect of intermittent and Gaussian inflow conditions on wind energy converters is studied experimentally. Two different flow situations were created in a wind tunnel using an active grid. Both flows exhibit nearly equal mean velocity values and turbulence intensities but strongly differ in their two point statistics, namely their distribution of velocity increments on a variety of timescales, one being Gaussian distributed, and the other one being strongly intermittent. A horizontal axis model wind turbine is exposed to both flows, isolating the effect on the turbine of the differences not captured by mean values and turbulence intensities. Thrust, torque and power data were recorded and analyzed, showing that the model turbine does not smooth out intermittency. Intermittent inflow is converted to similarly intermittent turbine data on all scales considered, reaching down to sub-rotor scales in space. This indicates that it is not correct to assume a smoothing of intermittent wind speed increments below the size of the rotor.

1 Introduction

Wind energy converters (WECs) work in a turbulent environment and are therefore turbulence-driven systems. The turbulent wind interacts with the *system dynamics*, resulting in the output parameters of a wind energy converter system such as power, mechanical loads or other quantities of interest.

Generally, the characteristics of the output dynamics of a WEC need to be understood in detail for multiple reasons. Power fluctuations have been reported in numerous studies, causing challenges in grid stability [1, 2, 3]. Drivetrain and gearbox failure rates remain high, adding to the cost of energy since gearboxes are among the most expensive parts of WECs. These types of failures are likely to be linked to torque fluctuations [4, 5]. Next, turbulent wind affects extreme and fatigue loads, which is clearly related to the lifetime of WECs [6].

Wind dynamics in the atmospheric boundary layer have been investigated extensively. Here, one has to differentiate between analyses concerning the statistics of the wind speed *values* and velocity *increments*. The wind velocities might become anomalously distributed due to large-scale meteorological events like downbursts or thunderstorms [7]. Velocity increments, on the other hand, statistically characterize the temporal aspect of fluctuations, whose non-Gaussian statistics are well-known from small-scale turbulence [8]. Active systems, like wind turbines discussed here, adapt to actual wind situations. Thus, in this paper we focus on wind speed changes within seconds, i.e., by the corresponding increments. Numerous studies have reported on non-Gaussian characteristics of wind speed increments; see, e.g., [9], [10], [11], and [12].

^aPublished as JANNIK SCHOTTLER, NICO REINKE, AGNIESZKA HÖLLING, JONATHAN WHALE, JOACHIM PEINKE and MICHAEL HÖLLING: On the impact of non-Gaussian wind statistics on wind turbines – an experimental approach, *Wind Energ. Sci.*, **2**, 1-13, 2017

Furthermore, findings of non-Gaussian wind statistics have been implemented in simulations by a variety of methods; see, e.g., [13], [14], and [15].

In the field of wind energy research, it is still unclear to what extent wind dynamics transfer to the parameters of a WEC such as loads, power etc. This most likely depends on the relevant timescales, which change with the system dynamics. Therewith, the conversion from wind to power, loads etc. vary with the turbine type. Consequently, it is important what scales in time and space are relevant to quantify the impact of turbulent wind on WECs [16], and scale-dependent analyses become necessary. Mücke et al. [14] found that intermittent inflow conditions do not significantly affect rain flow distributions of the torque. However, similarly intermittent torque increments based on a numeric wind turbine model used in the aeroelastic tool FAST [17] in combination with AeroDyn [18] were found. Gong et al. [15] investigated the short- and long-term extreme response distributions of a wind turbine during Gaussian and non-Gaussian inflow conditions using FAST. The extreme turbine responses to non-Gaussian inflow were considerably larger than the responses to Gaussian wind. However, Berg et al. [19] recently reported a vanishing effect of non-Gaussian turbulence on extreme and fatigue loads based on wind fields generated by large-eddy simulation (LES) in combination with aeroelastic load simulations using HAWC2 [20]. It was concluded that non-Gaussianity in sub-rotor-sized eddies is filtered by the rotor. Using field data, Milan et al. [21] showed that multi-MW WECs convert intermittent wind speeds to turbulent-like intermittent power with fluctuations down to the scale of seconds. Even on the scale of an entire wind farm, intermittent power output was reported. To summarize, different simulations and data from real turbines deliver an inconclusive answer to our question about the conversion from turbulent inflow to wind turbine data. It is not clear to what extent non-Gaussian flow conditions transfer to turbine parameters. At the same time, this is a very important aspect in the design process of wind turbines and in the wind field models used. Wrong assumptions about the conversion from turbulence characteristics to turbine data might lead to faulty dimensions and problems in the integration of wind energy in the power grid. Using wind tunnel experiments, we contribute to the ongoing discussion on the conversion process of non-Gaussian wind statistics to wind turbine data such as power, thrust and torque. A model wind turbine and an active grid for flow manipulation were used in order to examine to what extent Gaussian-distributed and highly intermittent wind speeds affect the model turbine dynamics differently. This paper is organized as follows: Sect. 2 gives an overview of commonly used methods for characterizing wind speed time series, parts of which are applied to offshore measurement data and simulated wind speed time series. Mathematical tools used throughout this paper are introduced here. Next, Sect. 3.1 describes the experimental methods used, including the setup, the definition of examined quantities and their processing. Section 4 shows the results of the experiments, which are discussed in Sect. 5. Finally, Sect. 6 gives the conclusion of the findings.

2 Atmopsheric flows

Since WECs work in turbulent wind conditions, a proper characterization of these conditions becomes necessary [16]. The industry standard IEC 61400-1 defines procedures for wind field description [22]. Power spectral densities, along with 10 min mean values and turbulence intensities, are considered. Therewith, only the first two statistical moments of a velocity time

series are taken into account. In this section, we give a brief overview of the methods used in the industry standard and beyond, along with their mathematical background, without claims of completeness. Furthermore, the methods of data analysis used in this study are introduced. We refer to Morales et al. [11] for a more detailed elaboration.

A general first step in characterizing a time series of wind velocities, $u(t)$, is the definition of velocity fluctuations [6],

$$u'(t) = u(t) - \langle u \rangle, \quad (2.1)$$

where $\langle u \rangle$ denotes the mean value of $u(t)$. A commonly used quantification of the general level of turbulence is the turbulence intensity (TI),

$$\text{TI} = \frac{\sigma_{\tilde{T}}}{\langle u \rangle_{\tilde{T}}}, \quad (2.2)$$

with $\sigma_{\tilde{T}}$ being the standard deviation of $u(t)$ during the time \tilde{T} [6]. Accordingly, $\langle u \rangle_{\tilde{T}}$ denotes the mean value over the same time span, which is typically 10 min in industry standards. Notice, since $\sqrt{\langle u'^2(t) \rangle_{\tilde{T}}} = \sigma_{\tilde{T}}$, only the first two statistical moments of the one point quantity u' are considered when describing a velocity time series by its fluctuations and/or turbulence intensity as previously defined.

Going one step further in the sense of two point quantities, we will consider velocity changes during a time lag τ and refer to them as velocity increments,

$$u_\tau(t) = u(t + \tau) - u(t), \quad (2.3)$$

throughout this paper. It is important to distinguish between a statistical description of the fluctuations and the increments. In stationary turbulence, $u'(t)$ is close to a Gaussian distribution, whereas increment statistics increasingly deviate from Gaussianity [8], which is also shown by Morales et al. [11] for offshore data. The n th-order moments of $u_\tau(t)$ are commonly referred to as n th-order structure functions [12]. The second-order structure function

$$\langle u_\tau(t)^2 \rangle = \langle (u(t + \tau) - u(t))^2 \rangle \quad (2.4)$$

is directly linked to the autocorrelation function $R_{uu}(\tau)$,

$$\langle u_\tau(t)^2 \rangle = 2\langle u(t)^2 \rangle - 2\langle u(t)u(t + \tau) \rangle \quad (2.5)$$

$$= 2\langle u(t)^2 \rangle (1 - R_{uu}(\tau)), \quad (2.6)$$

with the assumption that $\langle u(t)^2 \rangle = \langle u(t + \tau)^2 \rangle$. The autocorrelation function

$$R_{uu}(\tau) = \frac{1}{\sigma_u^2} \langle u(t)u(t + \tau) \rangle \quad (2.7)$$

is connected to the power spectral density (PSD) by the Fourier transformation.^a Therewith, the PSD, which is used broadly in wind field models such as the well-known Kaimal model [24], comprises the same information as the second-order structure function.

In order to include all higher-order structure functions, $\langle u_\tau^n \rangle$, we will consider the probability density functions (PDFs) of velocity increments, $p(u_\tau)$, for different time lags τ and refer to them as *increment PDF*. We normalize u_τ by its standard deviation,

$$\sigma_\tau = \sqrt{\frac{1}{N-1} \sum_{i=1}^N (u_{\tau_i} - \langle u_\tau \rangle)^2}, \quad (2.8)$$

^a $\mathcal{F}\{R_{uu}(\tau)\} = S(f)$, with $\sigma_u^2 = \int S(f)df$ and $S(f)$ being the power spectral density [23].

for better visual comparison. The statistical error of each bin of the PDF is estimated by $1/\sqrt{\tilde{n}}$, where \tilde{n} is the number of events in the respective bin. Throughout our analyses, values with a statistical error exceeding 10 % are marked with a red \times .

For design load calculations, different turbulence models are used. One, which is suggested by the IEC standard, is the Kaimal model, which considers power spectral densities and features merely Gaussian statistics. In this paper, we investigate to what extent wind characteristics not captured by standard models impact wind turbines. Furthermore, we consider a synthetic wind speed time series based on the Kaimal turbulence model, created using the software TurbSim [25], and compare it to offshore wind speed measurements taken from the FINO1 offshore measurement platform at 80 m height. The offshore data set is documented by Westerhellweg et al. [26]. We considered 10 Hz data for 1 year, and 10 min records of $7 \text{ m s}^{-1} \leq \langle u(t) \rangle_{10 \text{ min}} \leq 8 \text{ m s}^{-1}$ were selected. The approximately 3700 records were then combined and used in this analysis in order to ensure close-to-stationary conditions. It was shown by Morales et al. [11] that such a constraint filters out intermittency effects caused by nonstationary conditions on large scales and thus enables us to more properly study small-scale turbulence effects. It should be noted that only the mean value of one 10 min block is within $7.5 \pm 0.5 \text{ m s}^{-1}$. During this time span, samples outside of this interval are included. Table 2.1 shows the mean values, standard deviations and turbulence intensities of both data sets. As can be seen, the synthetic time series and the field measurements are very similar regarding their mean values and turbulence intensities (see Table 2.1). Going further, Fig. 2.1 shows $p(u_\tau)$ of both data sets, showing distinct differences regarding their distributions of increments. The Kaimal model comprises purely Gaussian statistics, while the offshore data features intermittent increment distributions. As shown in Fig. 2.1, certain characteristics of a wind speed time series, in particular extreme velocity increments, are not reflected correctly using standard methods. In this paper, we elaborate if and to what extent flow characteristics that are *not* captured by the standards (e.g., the first two statistical moments) impact wind turbines. We follow an experimental approach using a model wind turbine in a wind tunnel equipped with an active grid, allowing the generation of various turbulent inflow conditions. By tuning the intermittency while preserving mean wind speeds and turbulence intensities, the effect of intermittency is isolated.

Time series	$\langle u \rangle [\text{m s}^{-1}]$	$\sigma_u [\text{m s}^{-1}]$	TI [%]
Kaimal	7.51	0.54	7.21
FINO1	7.50	0.54	7.18

Table 2.1: First two statistical moments and turbulence intensities of a synthetic wind speed time series based on the Kaimal model and offshore data (FINO1). Values are rounded to two decimal places.

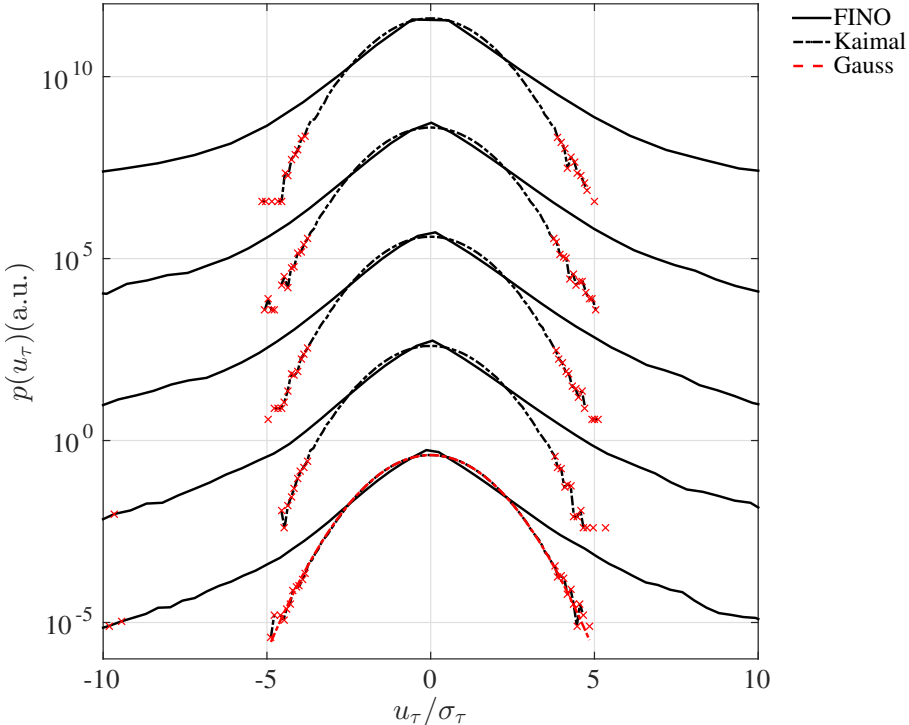


Figure 2.1: $p(u_\tau)$ for data sets based on the Kaimal model (dashed black line) and for offshore measurements, conditioned so that $\langle u \rangle = 7.5 \pm 0.5 \text{ m s}^{-1}$ (solid black). The PDFs for each scale are shifted vertically for better comparison, which is done throughout this paper. Scales from top to bottom $\tau = \{1, 5, 10, 30, 60 \text{ s}\}$.

3 Methods

3.1 Experimental setup

3.1.1 Wind tunnel and active grid

The experiments were conducted in a wind tunnel of the University of Oldenburg in open jet configuration. The outlet of $0.8 \text{ m} \times 1 \text{ m}$ (height \times width) was equipped with an active grid for turbulence generation with a similar design as described by Weitemeyer et al. [27]. The grid is made of nine vertical and seven horizontal axes with square metal plates attached. To allow an individual motion of the axes and thus flow manipulation, 16 stepper motors were used. However, throughout the experiments, all axes were excited simultaneously. We define a flap angle α , whereas $\alpha = 0^\circ$ is in alignment with the main flow direction (open) and $\pm 90^\circ$ corresponds to maximum blockage. At $\alpha = 0^\circ$, the blockage of the grid is approximately 6 %, considering the

cross-sectional area of the grid in relation to the wind tunnel outlet.

The excitation protocols of the motors were designed so that two different flow situations with the same mean wind velocities and comparable turbulence intensities were realized. At the same time, they strongly differ in their distributions of increments: one flow (A) being Gaussian distributed, the other one (B) being highly intermittent on a broad range of timescales, which shows a distinctly heavy-tailed distribution of velocity increments. The resulting time series are discussed in Sect. 4.1. The excitation protocol resulting in the intermittent flow featured an *active* flow modulation, where α was changed appropriately at a maximal rate of 50 Hz. For the Gaussian flow, the axes were not moved dynamically so that $\dot{\alpha} = 0^\circ$.

The flows considered were characterized using three single-wire hot-wire probes simultaneously in one plane normal to the main flow direction. The probes were arranged so that one was located at the position of the model wind turbine's hub and the other two in 0.6 D distance displaced in y and z directions (see Fig. 3.1). It should be noted that the turbine was not installed during flow characterization. The hot wires are 1.25 mm long with a diameter of 5 μm . A constant-temperature anemometry (CTA) module (Dantec 9054N0802) with a built-in low-pass filter set to 5 kHz was used. Data were recorded at 10 kHz for 25 min using a National Instruments cRIO-9074 real-time controller with in-house built LabVIEW software. When analyzing the flows, spatially averaged mean values of the three simultaneous measurements,

$$u(t) = \frac{1}{3} \sum_{i=1}^3 u_i(t), \quad (3.1)$$

are considered, where the index i denotes the respective hot wire. Following the concept of a rotor-effective wind speed as used by Schlipf et al. [28], this approach is more appropriate for describing the wind speed affecting the rotor than a single-point measurement. It should be noted that our results are hardly affected by using averaged measurements as opposed to data of the central hot wire. The distance from the active grid to the rotor and hence the hot wires was 1.1 m, which was set as a compromise between two aspects: first, the further away from the outlet, the greater the influence of the emerging shear layer [29], which should be limited. Second, the interaction of the rotor's blockage with the active grid increases with shorter distances. The evolution of the turbulence intensity and intermittency was also found to decay constantly around 1 m behind the grid [27]. Consequently, a distance of 1.1 m was chosen to balance the effects described.

3.1.2 Model wind turbine

A three-bladed horizontal-axis model wind turbine with a rotor diameter of $D = 0.58$ m was used. The vacuum-casted rotor blades are based on a SD7003 airfoil profile. The turbine is dynamically controlled with an operating tip speed ratio (TSR) comparable to modern full-scale turbines. Further details on the turbine design are described by Schottler et al. [30]. For details about the blade design, see Odemark et al. [31]. We consider the electrical power

$$P = P_{\text{el}} = U_{\text{gen}} \cdot I, \quad (3.2)$$

where U_{gen} is the generator voltage and I is the electric current of the circuit. I is obtained by measuring the voltage drop U_{sh} across a shunt resistor of $R_{\text{sh}} = 0.1 \Omega$, so that Eq. (3.2) becomes

$$P = U_{\text{gen}} \cdot \frac{U_{\text{sh}}}{R_{\text{sh}}}. \quad (3.3)$$

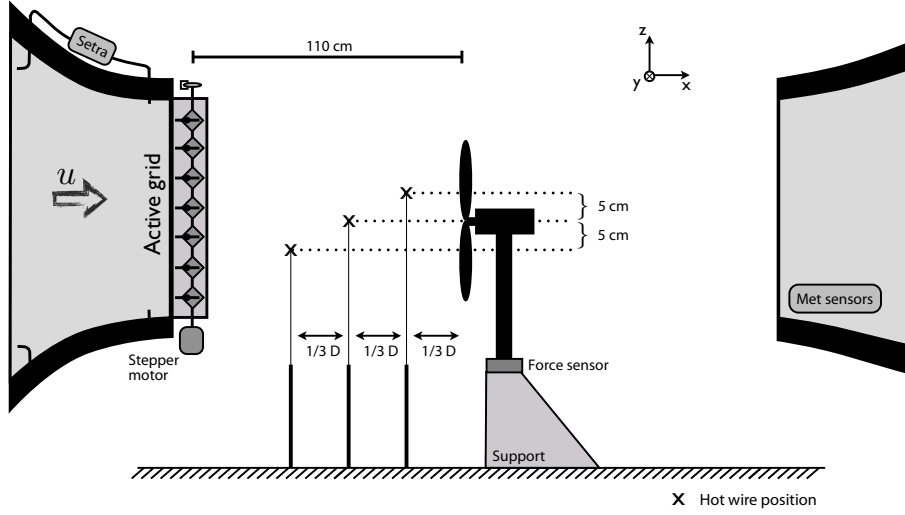


Figure 3.1: Schematic drawing of the experimental setup, side view. Scales do not match, $D = 0.58$ m.

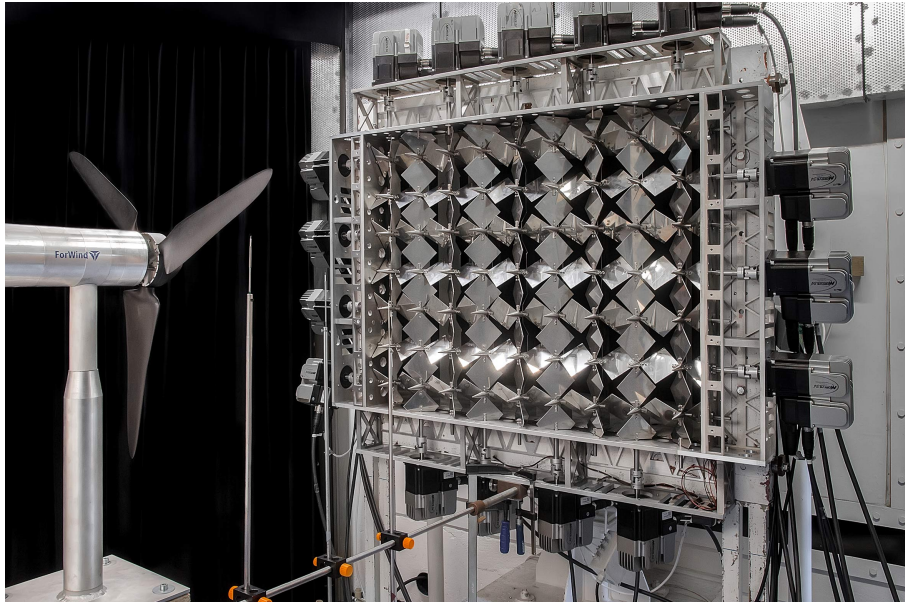


Figure 3.2: The model wind turbine and the active grid installed in a wind tunnel of the University of Oldenburg.

According to the generator's specifications, the torque T is proportional to the electric current I ,

$$T = k \cdot I, \quad (3.4)$$

with $k = 79.9 \text{ mN A}^{-1}$. The turbine features an automatic load control, with the process variable of the controller being the TSR based on hub-height wind speed measurements using a hot-wire probe two-thirds of D upstream of the rotor; see Fig. 3.1. The generator's load is controlled using an external voltage applied to a field-effect transistor (FET) within the electric circuit; see Schottler et al. [30] for details. Throughout this study, the TSR was set to $\lambda_{\text{set}} = 7$ to ensure a stable point of operation (not in stall) during the experiments.

To measure the thrust force acting on the turbine, it was placed on a three-component force balance (ME-Meßsysteme K3D120-50 N). Only the thrust force in main flow direction is considered; thus,

$$F = F_{\text{thrust},x} . \quad (3.5)$$

The setup is sketched in Fig. 3.1; Fig. 3.2 shows a photograph. As shown in Fig. 3.1, three hot wires were installed upstream of the rotor during turbine operation. In contrast to the flow characterization, only the center hot-wire signal at hub height was used when comparing inflow data to turbine data as done in Sect. 4.2.

3.2 Data preprocessing

For each experiment, data were recorded simultaneously. During flow characterization the three hot-wire probes were synchronized and during turbine data acquisition the thrust force, power, torque and hot-wire signals were recorded synchronously. Generally, all data sets are superimposed with some kind of measurement noise, which we generally want to exclude from our analyses, while preserving the fluctuations of the turbine signals resulting from the inflow. The data sets are filtered using a sixth-order Butterworth low-pass filter at a cutoff frequency of 15 Hz for the thrust data and 45 Hz for the power and torque data. Further details about the approach are shown in the Appendix. Figure 3.3 shows examples of the time series of the four different signals, filtered and unfiltered. The graph in Fig. 3.3a shows the wind speed during the intermittent inflow upstream of the turbine. The other graphs show the simultaneously recorded signals of the turbine. Only the filtered data sets are used for further analyses.

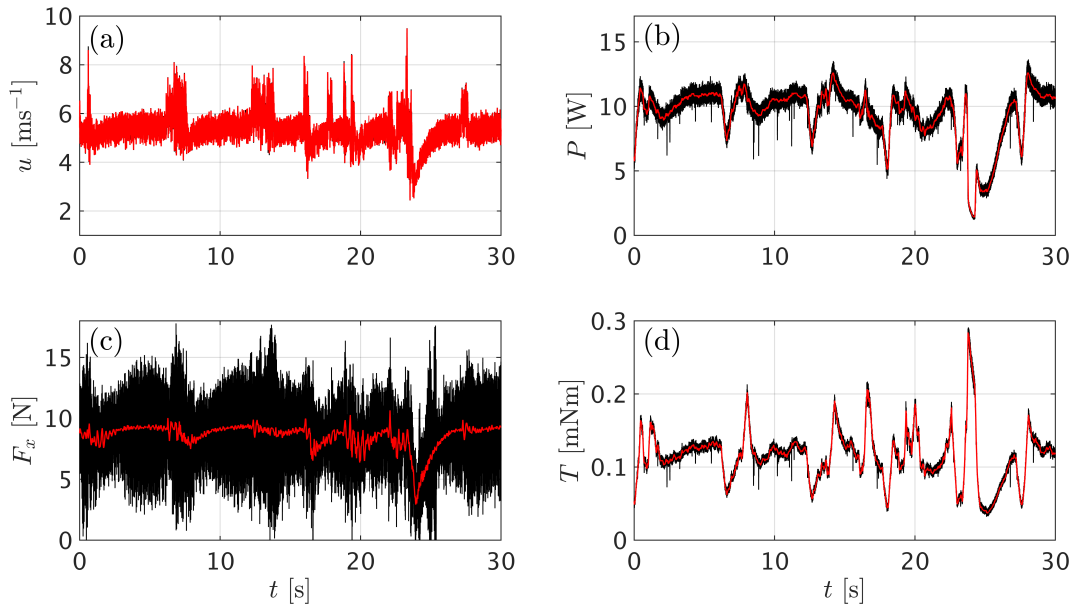


Figure 3.3: Original (black) and filtered (red) example time series of the wind speed **(a)**, power **(b)**, thrust force **(c)** and torque **(d)**. The wind speed was filtered using a sixth-order Butterworth low-pass filter at 2 kHz. In a similar way, the power and torque signals were filtered at 45 Hz and the thrust force at 15 Hz.

3.3 Choice of scales

As previously described, we will consider increment PDF of different timescales, $p(u_\tau)$. Defining relevant scales for WECs is not trivial and is the subject of discussion throughout the research community [16]. Therefore, a broad spectrum of timescales were chosen, ranging from the order of seconds to the smallest scale possible while applying the described filtering. By using Taylor's hypothesis of frozen turbulence [29], the chosen timescales are related to length scales of the model turbine, with $\langle u \rangle \approx 7 \text{ m s}^{-1}$. The largest scale considered is $\tau = 2 \text{ s}$. Thus, the turbine experiences a flow situation corresponding to a 14 m structure in the wind field impacting the model turbine. Smaller timescales are based on turbine dimensions and the filter frequencies. Table 3.1 gives an overview of the different scales considered. When analyzing thrust data, the smallest timescale, $\tau = 25 \text{ ms}$, was excluded due to the filtering of the data.

	Scale 1	Scale 2	Scale 3	Scale 4
Timescale τ [s]	2	0.08	0.067	0.025
Length/ D [-]	≈ 24	1	≈ 0.8	0.3
Physical object	– rotor diameter	–	order of blade length	

Table 3.1: Overview of scales considered in relation to certain characteristic turbine lengths. The timescales τ were used in the analyses. To get an idea of the spatial dimension, Taylor's hypothesis is used to transfer from time to space with $\langle u \rangle \approx 7 \text{ m s}^{-1}$. The obtained length scales are expressed as multiples of the rotor diameter for better comparison. The lengths are further related to physical objects of the turbine to get a sense of the dimensions.

4 Results

4.1 Inflow

Throughout the following analyses, two different flow situations will be considered and used as inflow conditions for the model wind turbine. Figure 4.1 shows the two wind speed time series as defined in Eq. (3.1) with $\langle u(t) \rangle \pm \sigma_u$ indicated. Additionally, Table 4.1 lists the mean values, standard deviations and turbulence intensities for the two cases and Fig. 4.2 shows a 30 s excerpt. We refer to the time series as inflow A and inflow B, according to Fig. 4.1. It is noteworthy that in describing the wind fields by their mean values and turbulence intensities, as it is widely done, both conditions A and B are virtually equivalent, as can be seen in Table 4.1.

However, just by looking at the time series, a difference becomes obvious, which will be investigated further. Therefore, Fig. 4.3 shows the increment PDF $p(u_\tau)$ of both time series for the scales listed in Table 3.1. Clearly, both flows are significantly different regarding intermittency. While inflow A follows a Gaussian trend, inflow B shows a strongly heavy-tailed, highly intermittent distribution of increments. Therefore, extreme events occur significantly more frequently in inflow B as compared to inflow A. Similar discrepancies as shown in Fig. 2.1 for offshore measurements and simulated data become obvious. It should be noted that the flows do not aim to

reproduce atmospheric wind speed time series. We focus on the statistical properties for chosen timescales as shown in Fig. 4.3.

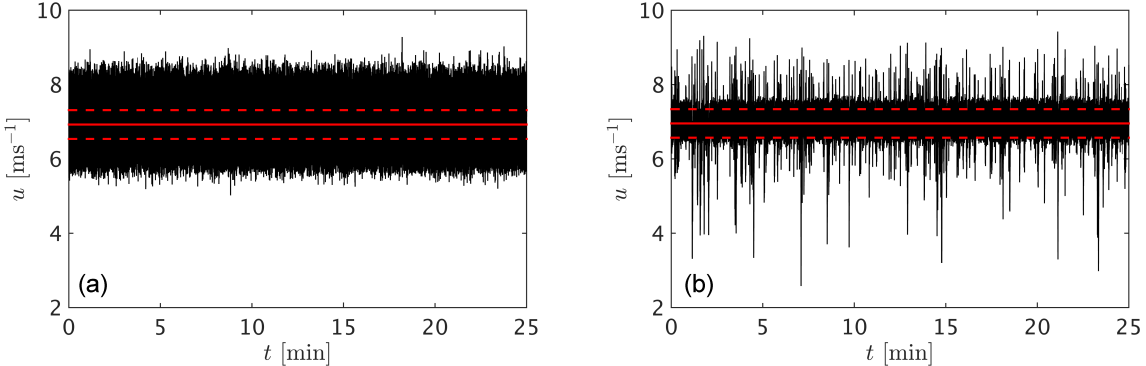


Figure 4.1: Velocity time series as defined in Eq. (3.1) of the two inflows considered, A (Gaussian, **a**) and B (intermittent, **b**). Further information is shown in Table 4.1. Solid red lines mark $\langle u(t) \rangle$ and dashed red lines indicate $\langle u(t) \rangle \pm \sigma_u$.

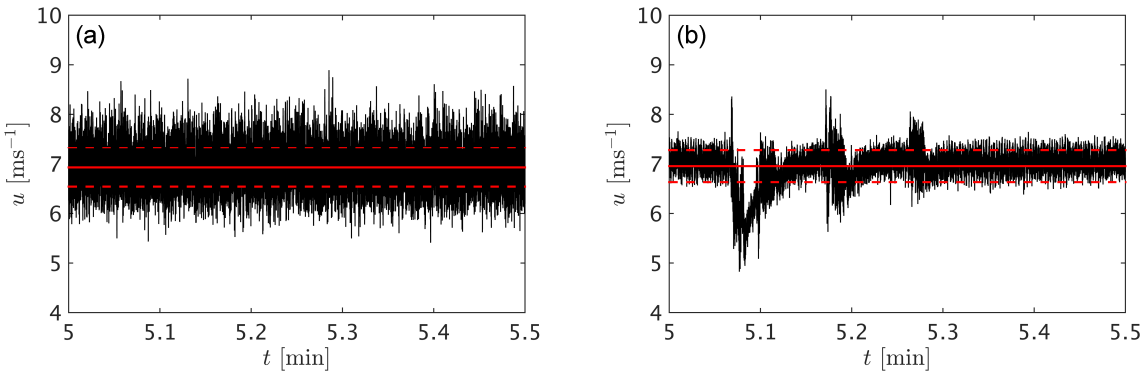


Figure 4.2: Excerpts of both time series shown in Fig. 4.1.

Time series	$\langle u(t) \rangle$ [m s^{-1}]	σ_u [m s^{-1}]	TI [%]
A	6.92	0.39	5.59
B	6.96	0.38	5.50

Table 4.1: First two statistical moments of the time series shown in Fig. 4.1 and their turbulence intensities. Values are rounded to two decimal places.

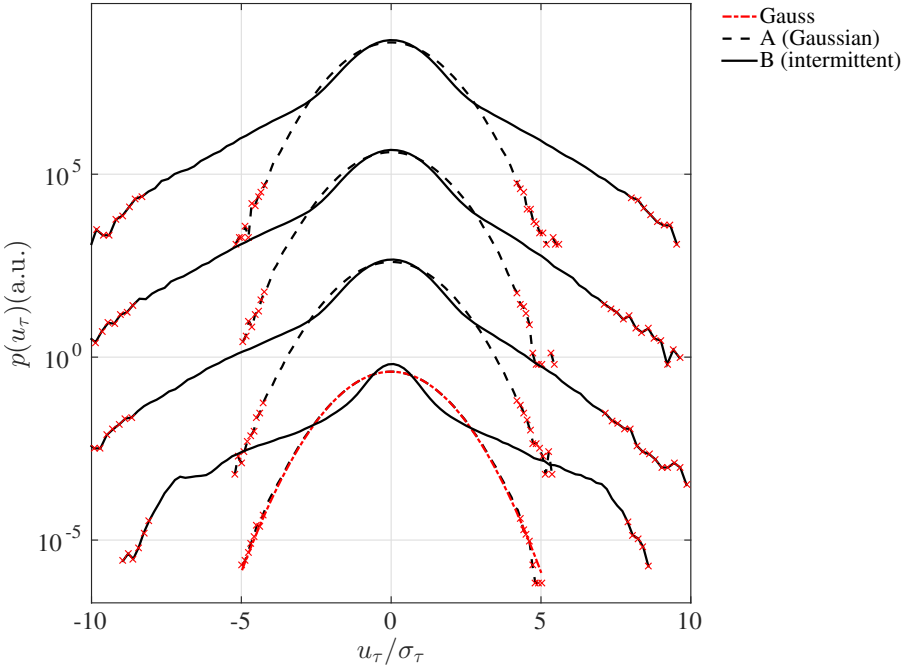


Figure 4.3: $p(u_\tau)$ of both velocity time series shown in Fig. 4.1, A (dashed) and B (solid), for $\tau = \{25, 67, 80 \text{ ms}, 2 \text{ s}\}$ from top to bottom. The different scales are shifted vertically for presentation. A Gaussian fit (dashed red line) of $p(u_{\tau=2 \text{ s}})$ for inflow A is added to guide the eye.

4.2 Turbine reaction

Next, we investigate the performance data of the model wind turbine when exposed to both A and B flows. To begin with, we consider the thrust force in main flow direction, $p(F_\tau)$, in Fig. 4.4. Clearly, the difference between Gaussian and non-Gaussian inflow conditions remains present in the thrust data for all timescales considered. Non-Gaussian increments are not filtered by the rotor. Going further, we directly compare the normalized quantities, $p(F_\tau)$ and $p(u_\tau)$, separately for both flow conditions in Fig. 4.5. Neither for the Gaussian nor for the intermittent case can a change in the forms of the increment PDF be observed. Thus, we conclude that the non-Gaussian character of the inflow is not averaged out by the rotor. In Figs. 4.4 and 4.5, the smallest timescale of $\tau = 25 \text{ ms}$ is not shown for the thrust data since that scale interferes with the previously applied low-pass filter as described in Sect. 3.2.

So far, we have considered the thrust force of the turbine as an example, showing a transfer of intermittency from u_τ to F_τ by the system dynamics of the turbine. For the power and torque we obtain similar results as for the thrust; thus, we present all quantities for the intermittent inflow together in Fig. 4.6. None of the quantities smooth out the intermittent inflow to a close-to-Gaussian distribution. Minor deviations of the respective increment PDFs are discussed in Sect. 5.

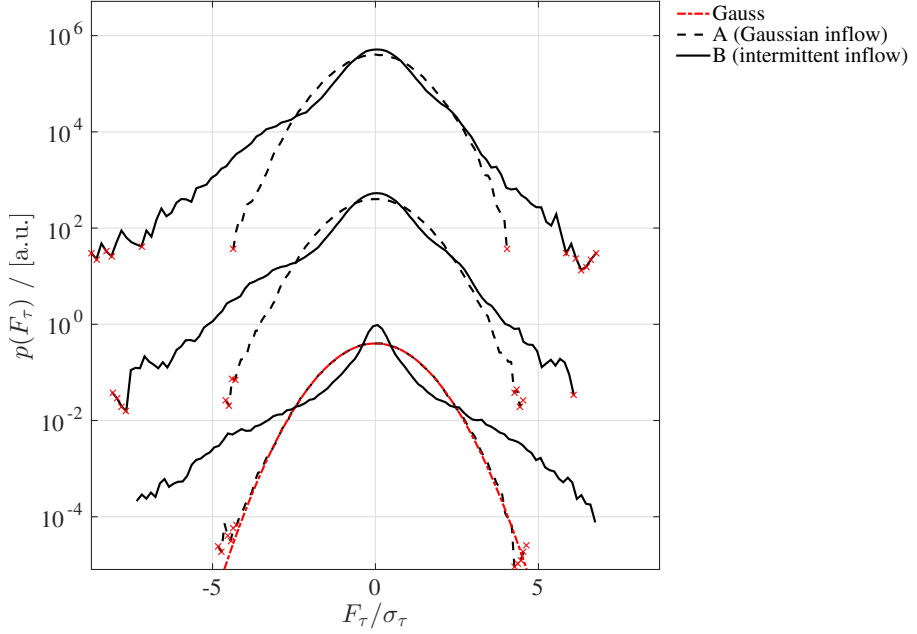


Figure 4.4: $p(F_\tau)$ of the turbine's thrust force (in main flow direction) exposed to the inflow conditions A (dashed) and B (solid) for $\tau = \{67, 80 \text{ ms}, 2 \text{ s}\}$ from top to bottom. The different scales are shifted vertically for presentation.

5 Discussion

To what extent non-Gaussian wind statistics impact WECs is an ongoing discussion throughout the wind energy research community. Using an active grid to create different turbulent inflow conditions allows experimental investigations of the impact of turbulence on wind turbines. This study can therefore supplement present approaches in the literature that investigate the impact of non-Gaussianity based on numerical simulations [14, 15, 19] or field measurements [21]. However, when using the model wind turbine to grasp the impact of the different inflows considered, we do not claim full scalability. There is a Reynolds number mismatch between the scaled laboratory model and full-scale turbines. Furthermore, the model is not aero-elastically scaled. Therefore, a detailed study of the (time-) scale dependency of the results is not included here, but chosen timescales as described in Sect. 3.3 are analyzed. The flows described in Sect. 4.1 were generated with a focus on their statistical properties on those scales. The focus is not on details of the time sequences or spectral properties. They aim to reproduce the discrepancy between industry standards and atmospheric wind data in terms of increment statistics.

When processing the experimental data, signal fluctuations not resulting from the inflow are excluded from the analysis by previously applied low-pass filters. While noise is only a minor issue considering the power and torque, the thrust data from the force balance are significantly

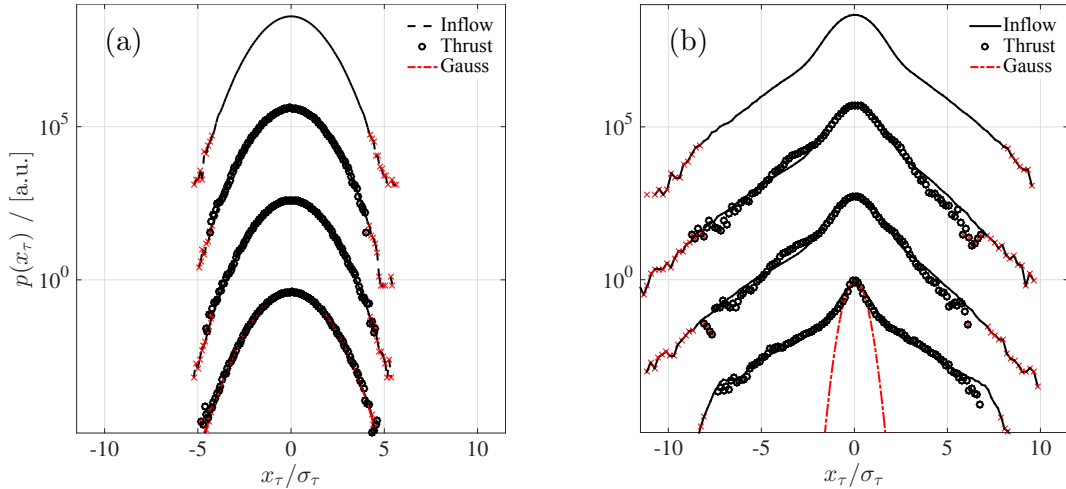


Figure 4.5: $p(u_\tau)$ (lines) and $p(F_\tau)$ (circles) for both Gaussian (a) and intermittent (b) inflow conditions. Scales as in Fig. 4.4 from top to bottom, $\tau = \{25, 67, 80 \text{ ms}, 2 \text{ s}\}$, shifted vertically for presentation.

superimposed by signal fluctuations resulting from the setup itself; see Fig. 3.3c. These most likely arise from vibrations of the whole setup during turbine operation, ranging from the turbine itself and the support to the fixation in the ground. These fluctuations are of an amplitude that would influence the analysis; however, they are of a higher frequency than the cutoff frequency of the applied low-pass filter. Therefore, they are indeed excluded from the analysis. At the same time, the procedure described in Appendix 6 might filter fluctuations of higher frequency than the respective cutoff, which are actually directly related to wind speed variations. As a result, minimal timescales have to be set, potentially excluding interesting results for smaller scales. Considering Fig. 6.2a, the coherence of the hot-wire signal and the thrust data is almost lost completely at approximately 10 Hz. Since this corresponds to a timescale of $\tau = 0.1 \text{ s}$ or a length scale of 0.7 m ($\approx 1.2 D$), a cutoff frequency of 15 Hz was chosen in order to include a scale between the rotor diameter and the blade length. From the analysis of other intermittent data, it can be shown that our filtering does not affect the intermittency effects in a significant way. Thus, the filtering only suppresses noise effects.

There might also be aerodynamic effects that are of even higher frequency than the inflow fluctuations and are therefore not captured due to the filtering. Such effects at the rotor are possibly excluded by the low-frequency filtering. This study, however, focuses on dynamics caused by the inflow turbulence.

Considering Fig. 4.6, some minor deviations between the increment PDF of the inflow and the turbine data can be observed. The torque and the power as defined in Eqs. (3.4) and (3.3) are part of the electrical circuit and are therefore directly linked to the manipulative variable of the controller, being the voltage applied to the FET, U_{FET} . Thus, an analysis of those quantities includes not only fluctuations caused by the inflow but also those resulting from the controller. As overshoots are typical for closed-loop control systems [32, 33], they likely bias the present analysis, especially for small timescales regarding the power and the torque. This most likely causes the asymmetric distributions of power and torque increments in Fig. 4.6. Because of this, the focus of the analysis is on the thrust data. Nonetheless, the main finding that *all* quantities feature strongly intermittent distributions of increments remains, despite differences among the parameters, as Fig. 4.6 shows.

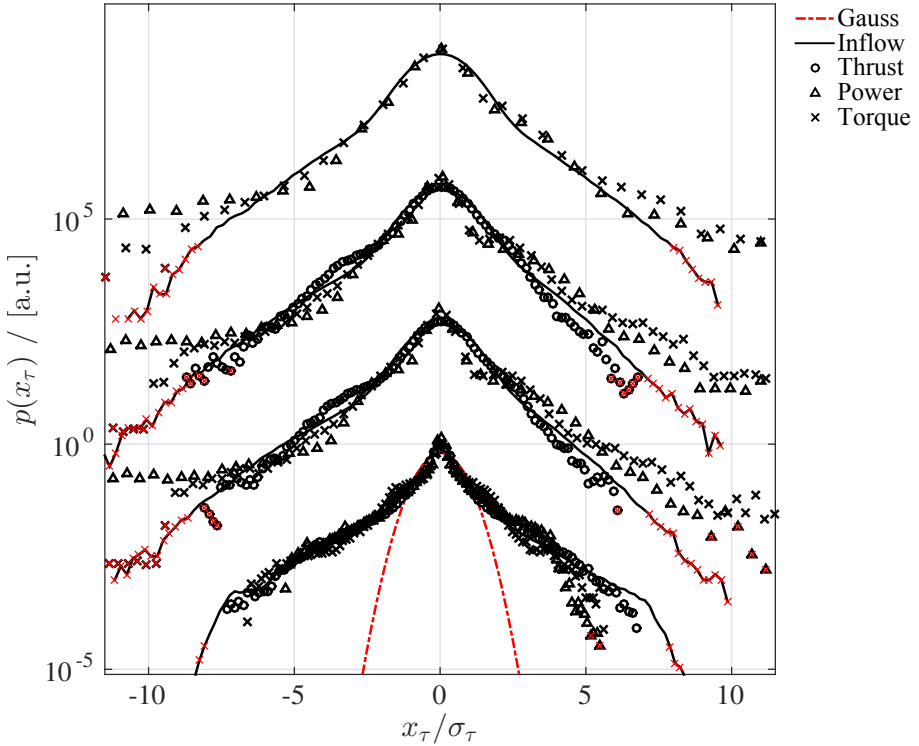


Figure 4.6: $p(x_\tau)$ for the intermittent inflow condition (line, see Fig. 4.1a), thrust (circles), power (triangles) and torque (crosses). Scales as in Fig. 4.4 from top to bottom, $\tau = \{25, 67, 80 \text{ ms}, 2 \text{ s}\}$, shifted vertically for presentation.

6 Conclusion

In this study, an experimental setup that allows the investigation of interactions between various turbulent flows with a model wind turbine was realized. Experiments were performed in order to elaborate on the impact of non-Gaussian wind statistics on WECs. Our results do not show any filtering of the intermittent features of wind fields found in the atmosphere by the turbine. Consequently, one should be aware that wind characteristics, which are not reflected in standard wind field descriptions, the IEC 61400-1 for example, have a significant impact on wind turbines. Intermittent inflow is converted to similarly intermittent turbine data on all scales considered, ranging down to sub-rotor scales. Thus, statistical properties of the inflow time series that are not captured by describing them using one-point statistics are of relevance and should be included in standards characterizing inflow conditions. If intermittent inflows lead to intermittent loading, including extreme loads that occur much more frequently than currently modeled in the standards, then this has implications for the use of the current standards in designing wind turbines to withstand the wind conditions experienced.

Appendix

Data processing – coherence analysis

As described in Sect. 3.2, the raw data sets are superimposed by measurement noise, which should be excluded from the analyses. Since we analyze different parameters, an appropriate filtering of the different raw signals should, nonetheless, allow a comparison of their statistics. This section shows the procedure of choosing appropriate filter frequencies. To begin with, $u(t)$ during the intermittent inflow B is filtered using a sixth-order Butterworth low-pass filter. The cutoff frequency is set to 2 kHz since high-frequency noise, which is typical for hot-wire anemometers [34], should be filtered. Furthermore, the resolved length scales corresponding to 2 kHz (\sim mm, using Taylor's hypothesis; [29]) are reasonably small for our purposes. Figure 6.1 shows the PSD of both flows based on raw and filtered data. Since we want to concentrate on the fluctuations of turbine data caused by the inflow, we estimate a maximal frequency for which the fluctuations of the respective turbine data are coherent with the fluctuations of the filtered velocity signal. Therefore, we consider the magnitude-squared coherence,

$$\gamma_{u'x'}^2 = \frac{|P_{u'x'}(f)|^2}{P_{u'u'}(f)P_{x'x'}(f)} , \quad (6.1)$$

of the filtered wind speed fluctuations of the intermittent inflow (B) and the fluctuations of the respective turbine quantity x' [35], with x being the power, torque or thrust. $P_{u'x'}$ denotes the

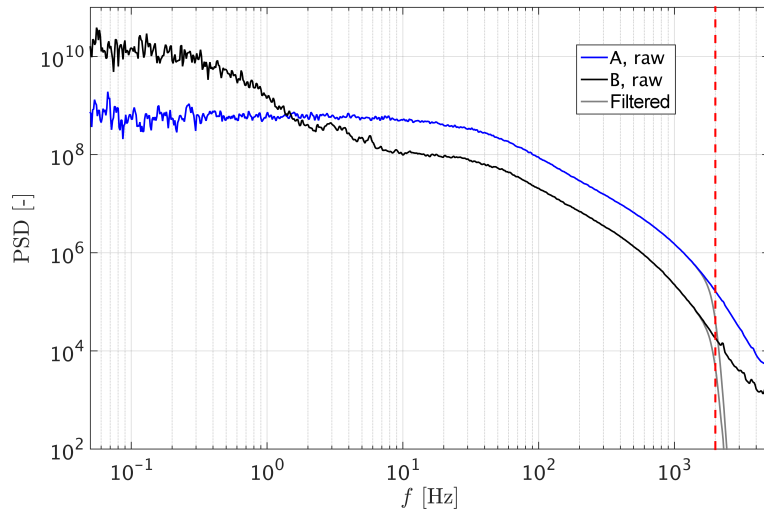


Figure 6.1: Power spectral density (PSD) of $u(t)$ for the Gaussian inflow A (blue) and the intermittent inflow B (black). The effect of a sixth-order Butterworth low-pass filter at $f_{\text{cut}} = 2$ kHz is shown in gray. The dashed red line marks $f_{\text{cut}} = 2$ kHz.

cross-spectral density; $P_{u'u'}$ and $P_{x'x'}$ denote the autospectra. The results are shown in Fig. 6.2. At the values indicated by the dashed red lines in Fig. 6.2, the coherence of the signals is almost completely lost. Therefore, we choose a cutoff frequency of 15 Hz for the thrust data and 45 Hz for the power and torque data to filter the raw data using a sixth-order Butterworth low-pass filter. Hereby, higher frequencies are excluded, as only fluctuations resulting from the inflow should be considered.

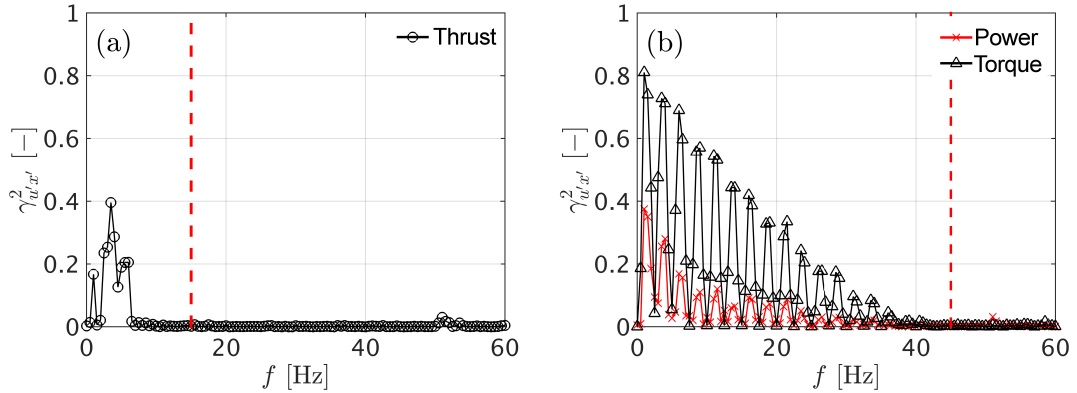


Figure 6.2: Magnitude-squared coherence of filtered hot-wire data and thrust (a) as well as power and torque (b). Used here were 500 Hanning windows with 50% overlap, as suggested by Carter et al. [35]. Panel (b) shows regular drops of γ^2 , which are caused by a filter function within the control algorithm of the model turbine. Since the controller affects the electrical circuit, there is a direct connection to the electrical current and therewith to the power and torque. Consequently, the effect of the filter is clearly visible in this graph.

Variances of increment PDF

For completeness, the variances σ_τ^2 of every time series of increments, x_τ , are shown in Table 6..1 for the synthetic and offshore data (see Fig. 2.1) and for the experimental data in Table 6.2.

Timescale τ [s]	1	5	10	30	60
$\text{var}(u_\tau)$, Kaimal [$\text{m}^2 \text{s}^{-2}$]	0.25	0.47	0.53	0.58	0.58
$\text{var}(u_\tau)$, FINO1 [$\text{m}^2 \text{s}^{-2}$]	0.04	0.11	0.15	0.24	0.31

Table 6..1: Variances of each increment time series, $u_\tau(t)$, for synthetic data based on the Kaimal model and field data.

Timescale τ [s]	0.025	0.067	0.08	2
$\text{var}(u_\tau)$, Inflow A [$\text{m}^2 \text{s}^{-2}$]	0.30	0.30	0.30	0.30
$\text{var}(u_\tau)$, Inflow B [$\text{m}^2 \text{s}^{-2}$]	0.06	0.08	0.09	0.252
$\text{var}(F_\tau)$, Inflow A [$\text{m}^2 \text{s}^{-2}$]	—	0.03	0.06	0.13
$\text{var}(F_\tau)$, Inflow B [$\text{m}^2 \text{s}^{-2}$]	—	0.11	0.14	0.86
$\text{var}(P_\tau)$, Inflow A [$\text{m}^2 \text{s}^{-2}$]	0.03	0.12	0.16	3.31
$\text{var}(T_\tau)^*$, Inflow B [$\text{m}^2 \text{s}^{-2}$]	1.17	6.28	8.48	133.72

$* \times 10^{-5}$.

Table 6.2: Variances of each increment time series for the experimental data. $\text{var}(u_\tau)$ corresponds to the graphs shown in Fig. 4.3, $\text{var}(F_\tau)$ to the graphs in Fig. 4.4, $\text{var}(P_\tau)$ and $\text{var}(T_\tau)$ to $p(P_\tau)$ and $p(T_\tau)$, respectively, as shown in Fig. 4.6.

Bibliography

- [1] Z. Chen and E. Spooner. Grid power quality with variable speed wind turbines. *Energy Conversion, IEEE Transactions on*, 16(2):148–154, 2001.
- [2] J. M. Carrasco, L. G. Franquelo, J. T. Bialasiewicz, S. Member, E. Galván, R. C. P. Guisado, S. Member, M. Ángeles, M. Prats, J. I. León, and N. Moreno-alfonso. Power-Electronic Systems for the Grid Integration of Renewable Energy Sources : A Survey. *Ieee Transactions on Industrial Electronics*, 53(4):1002–1016, 2006.
- [3] P. Sørensen, N. A. Cutululis, A. Vigueras-Rodriguez, L. E. Jensen, J. Hjerrild, M. H. Donovan, and H. Madsen. Power Fluctuations From Large Wind Farms. *IEEE Transactions on Power Systems*, 22(3):958–965, 2007.
- [4] W. Musial, S. Butterfield, and B. McNiff. Improving Wind Turbine Gearbox Reliability Preprint. *European Wind Energy Conference*, pages 1–13, 2007.
- [5] Y. Feng, Y. Qiu, C. J. Crabtree, H. Long, and P. J. Tavner. Monitoring wind turbine gearboxes. *Wind Energy*, 16(5):728–740, jul 2013.
- [6] T. Burton, D. Sharpe, N. Jenkins, and E. Bossanyi. *Wind Energy Handbook*. John Wiley and Sons, 2001.
- [7] P. De Gaetano, M. P. Repetto, T. Repetto, and G. Solari. Separation and classification of extreme wind events from anemometric records. *Journal of Wind Engineering and Industrial Aerodynamics*, 126:132–143, mar 2014.
- [8] U. Frisch. *Turbulence : the legacy of A.N. Kolmogorov*, volume 1. Cambridge university press, 1995.
- [9] F. Boettcher, C. Renner, H. P. Waldl, and J. Peinke. On the statistics of wind gusts. *Boundary-Layer Meteorology*, 108(1):163–173, 2003.
- [10] L. Liu, F. Hu, X.-L. Cheng, and L.-L. Song. Probability Density Functions of Velocity Increments in the Atmospheric Boundary Layer. *Boundary-Layer Meteorology*, 134(2):243–255, 2010.

- [11] A. Morales, M. Wächter, and J. Peinke. Characterization of wind turbulence by higher-order statistics. *Wind Energy*, 15(3):391–406, 2012.
- [12] M. Wächter, H. Heißelmann, M. Hölling, A. Morales, P. Milan, T. Mücke, J. Peinke, N. Reinke, and P. Rinn. The turbulent nature of the atmospheric boundary layer and its impact on the wind energy conversion process. *Journal of Turbulence*, 13:N26, 2012.
- [13] M. Nielsen, G. Larsen, and K. Hansen. Simulation of inhomogeneous, non-stationary and non-Gaussian turbulent winds. *Journal of Physics: Conference Series*, 75(1):12060, 2007.
- [14] T. Mücke, D. Kleinhans, and J. Peinke. Atmospheric turbulence and its influence on the alternating loads on wind turbines. *Wind Energy*, 14(2):301–316, 2011.
- [15] K. Gong and X. Chen. Influence of non-Gaussian wind characteristics on wind turbine extreme response. *Engineering Structures*, 59:727–744, 2014.
- [16] G. A. M. van Kuik, J. Peinke, R. Nijssen, D. Lekou, J. Mann, J. N. Sørensen, C. Ferreira, J. W. van Wingerden, D. Schlipf, P. Gebraad, H. Polinder, A. Abrahamsen, G. J. W. van Bussel, J. D. Sørensen, P. Tavner, C. L. Bottasso, M. Muskulus, D. Matha, H. J. Lindeboom, S. Degraer, O. Kramer, S. Lehnhoff, M. Sonnenschein, P. E. Sørensen, R. W. Künneke, P. E. Morthorst, and K. Skytte. Long-term research challenges in wind energy – a research agenda by the european academy of wind energy. *Wind Energy Science*, 1(1):1–39, 2016.
- [17] J. M. Jonkman and M. L. Buhl Jr. Fast user’s guide. *National Renewable Energy Laboratory, Golden, CO, Technical Report No. NREL/EL-500-38230*, 2005.
- [18] P. J. Moriarty and A. C. Hansen. *AeroDyn theory manual*. Citeseer, 2005.
- [19] J. Berg, A. Natarajan, J. Mann, and E. G. Patton. Gaussian vs non-Gaussian turbulence: impact on wind turbine loads. *Wind Energy*, 17(April 2013):n/a–n/a, 2016.
- [20] T. J. Larsen and A. M. Hansen. *How 2 HAWC2, the user’s manual*. Risø National Laboratory, 2007.
- [21] P. Milan, M. Wächter, and J. Peinke. Turbulent character of wind energy. *Phys. Rev. Lett.*, 110:138701, Mar 2013.
- [22] International Electrotechnical Commission. Iec 61400-1: Wind turbines part 1: Design requirements. 2005.
- [23] W. H. Press, S. A. Teukolsky, W. T. Vetterling, and B. P. Flannery. *Numerical Recipes in C (2Nd Ed.): The Art of Scientific Computing*. Cambridge University Press, New York, NY, USA, 1992.
- [24] J. C. J. Kaimal, J. C. J. Wyngaard, Y. Izumi, O. R. Coté, and O. R. Cote. Spectral Characteristics of Surface-Layer Turbulence. *Quarterly Journal of the ...*, 98(417):563–589, 1972.
- [25] B. J. Jonkman. Turbsim user’s guide: Version 1.50, 2009.
- [26] A. Westerhellweg, T. Neumann, and V. Riedel. Fino1 mast correction. *Dewi magazin*, 40:3, 2012.

- [27] S. Weitemeyer, N. Reinke, J. Peinke, and M. Hölling. Multi-scale generation of turbulence with fractal grids and an active grid. *Fluid Dynamics Research*, 45:061407, 2013.
- [28] D. Schlipf, D. J. Schlipf, and M. Kühn. Nonlinear model predictive control of wind turbines using LIDAR. *Wind Energy*, 16(7):1107–1129, oct 2013.
- [29] J. Mathieu and J. Scott. *An introduction to turbulent flow*. Cambridge University Press, 2000.
- [30] J. Schottler, A. Hölling, J. Peinke, and M. Hölling. Design and implementation of a controllable model wind turbine for experimental studies. *Journal of Physics: Conference Series*, 753:072030, sep 2016.
- [31] Y. Odemark. Wakes behind wind turbines-studies on tip vortex evolution and stability. 2012.
- [32] B. A. Ogunnaike and W. H. Ray. *Process dynamics, modeling, and control*, volume 1. Oxford University Press New York, 1994.
- [33] I.-l. Chien and Y. Chung. Simple PID controller tuning method for processes with inverse response plus dead time or large overshoot response plus dead time. *Industrial & engineering ...*, pages 4461–4477, 2003.
- [34] F. E. Jørgensen and M. Hammer. Hot-wire anemometry behaviour at very high frequencies. *Measurement Science and Technology*, 8(3):221–221, 1999.
- [35] G. C. Carter, C. H. Knapp, and A. H. Nuttall. Estimation of the Magnitude-Squared Coherence Function Via Overlapped Fast Fourier Transform Processing. *IEEE Transactions on Audio and Electroacoustics*, 21(4):337–344, 1973.

Paper 2

Wind tunnel experiments on wind turbine wakes in yaw: Redefining the wake width^a

JANNIK SCHOTTLER, JAN BARTL, FRANZ MÜHLE, LARS SÆTRAN, JOACHIM PEINKE and MICHAEL HÖLLING

Abstract. This paper presents an investigation of wakes behind model wind turbines, including cases of yaw misalignment. Two different turbines were used and their wakes are compared, isolating effects of boundary conditions and turbine specifications. Laser Doppler anemometry was used to scan full planes of wakes normal to the main flow direction, six rotor diameters downstream of the respective turbine. The wakes of both turbines are compared in terms of the time-averaged main flow component, the turbulent kinetic energy and the distribution of velocity increments. The shape of the velocity increments' distributions is quantified by the shape parameter λ^2 . The results show that areas of strongly heavy-tailed distributed velocity increments surround the velocity deficits in all cases examined. Thus, a wake is significantly wider when two-point statistics are included as opposed to a description limited to one-point quantities. As non-Gaussian distributions of velocity increments affect loads of downstream rotors, our findings impact the application of active wake steering through yaw misalignment as well as wind farm layout optimizations and should therefore be considered in future wake studies, wind farm layout and farm control approaches. Further, the velocity deficits behind both turbines are deformed to a kidney-like curled shape during yaw misalignment, for which parameterization methods are introduced. Moreover, the lateral wake deflection during yaw misalignment is investigated.

1 Introduction

Due to the installation of wind turbines in wind farm arrangements, the turbine wakes become inflow conditions of downstream rotors, causing wake effects. Those include a reduced wind velocity and an increased turbulence level. The former causes power losses of up to 20 % [1] in wind farms, while the latter is linked to increased loads of downstream turbines, affecting fatigue and lifetime [2]. In order to mitigate wake effects, various concepts of active wake control strategies have been proposed and investigated. One concept is an active wake steering by an intentional yaw misalignment, where the velocity deficit behind a rotor is deflected laterally by misaligning it with the mean inflow direction. The possibility of wake re-direction by yawing was observed and investigated by means of numeric simulations [e.g., 3, 4], in wind tunnel experiments [e.g., 5, 6] and in full-scale field measurements by Trujillo et al. [7]. Further, the potential of increasing the power yield in a wind farm configuration has been explored experimentally [8], numerically [e.g., 4, 9] and in a field test in a full-scale wind farm [10], showing promising results as the total power yield could be increased in the mentioned studies. As the applicability of the concept to future wind farms requires a thorough understanding of the wakes behind yawed wind

^aPublished as JANNIK SCHOTTLER, JAN BARTL, FRANZ MÜHLE, LARS SÆTRAN, JOACHIM PEINKE and MICHAEL HÖLLING: Wind tunnel experiments on wind turbine wakes in yaw: redefining the wake width, *Wind Energ. Sci.*, **3**, 257–273, 2018

turbines, this study examines the wakes behind model wind turbines during yaw misalignment. Experimental studies are necessary to validate numeric results, to tune engineering models and to gain a deeper understanding of the present effects in a controlled laboratory environment. However, when examining wake effects experimentally, varying turbine models are used. Those models strongly differ in their complexity and design, including blade design, geometry or control concepts. The simplest model is a drag disc concept, where a wind turbine is modeled by a porous disk in the flow as done by Espa a et al. [11] and Howland et al. [12]. Moreover, rotating turbine models have been used in numerous studies, where the design and complexity of the models vary significantly. Examples include Medici et al. [5], Bottasso et al. [13], Abdulrahim et al. [14], Rockel et al. [15] or Bastankhah et al. [16]. In contrast to numerical studies, where the vast majority of the research community uses consistent turbine models (NREL 5 MW [17] or DTU 10 MW [18] reference turbines for example), experiments lack certain systematics and comparability due to varying turbine models, facilities and measurement techniques. The present study aims to compare the wakes of two different model wind turbines in the same facility, using comparable boundary conditions as far as possible. In doing so, a separation between general wake effects and turbine specific observations can be achieved.

We present wake analyses ranging from mean quantities to higher-order statistics. Average mean flow components are of relevance when assessing the energy yield of potential downstream turbines. An investigation of turbulence parameters such as the turbulent kinetic energy (TKE) is linked to fluctuating inflow conditions, which is important for loads of downstream turbines and thus their lifetime [2]. To gain a deeper insight, we extend our analyses to two-point statistics. More precisely, velocity increments are analyzed, allowing for a scale-dependent analysis of flows. Non-Gaussianity of the distributions of velocity increments has been reported not only in small-scale turbulence [19] but also in the atmospheric boundary layer [e.g., 20, 21, 22]. To what extent statistical characteristics of velocity increments are transferred to wind turbines is of current interest throughout the research community [23]. Schottler et al. [24] found a transfer of intermittency from wind to torque, thrust and power data in a wind tunnel experiment using a model wind turbine. Similarly, M cke et al. [25] found a transfer of intermittency to torque data using a generic turbine model. Milan et al. [26] reported intermittent power data in a full-scale wind farm. We thus believe that distributions of velocity increments in wakes are of importance for potential downstream turbines as non-Gaussian characteristics are likely to be transferred to wind turbines in terms of fluctuating loads and power output. Consequently, investigations of velocity increments in wakes are extremely relevant for active wake control concepts as well as for wind farm layout optimization approaches. A further elaboration on the connection between non-Gaussian velocity increments and loads as well as power fluctuations is given in Sect. 4.

This work is organized as follows. Section 2 introduces the methods used throughout the study, including the experimental methods, a concept for quantifying a wake's deflection and a definition of the examined parameters. Section 3 shows the results of the study. First, results of the non-yawed rotors are investigated and compared in Sect. 3.1. Wakes during yaw misalignment are analyzed in Sect. 3.2, including a quantification of the wake deflection. Section 4 discusses the findings before Sect. 5 summarizes this work and states the conclusions. This work is part of a joint experimental campaign by the Norwegian University of Science and Technology (NTNU) in Trondheim and ForWind in Oldenburg, Germany. While this paper compares the wakes behind two different model wind turbines, a second paper by Bartl et al. [27] examines the influence of varying inflow conditions on the wake of one model wind turbine.

2 Method

2.1 Experimental methods

The experiments were performed in the wind tunnel of the NTNU in Trondheim, Norway. The closed-loop wind tunnel has a closed test section of $2.71\text{ m} \times 1.81\text{ m} \times 11.15\text{ m}$ (width \times height \times length). The inlet to the test section was equipped with a turbulence grid having a solidity of 35 % and a mesh size of 0.24 m. Further details on the grid are described by Bartl et al. [28].

Two different model wind turbines were used that vary in geometry, blade design and direction of rotation. Those deliberate distinctions allow for an isolation of general effects of wake properties. The turbines will be denoted NTNU and ForWind. Table 2.1 summarizes the main features and differences of both turbines, further details are described by Schottler et al. [29]. Figure 2.1 shows technical drawings. As can be seen, the ForWind turbine was placed on four cylindrical poles to lift the rotor above the wind tunnel boundary layer to a hub height of 820 mm above the wind tunnel floor. One turbine at a time was placed on a turning table allowing for yaw misalignment, denoted by the angle γ , which is positive for a clockwise rotation of the rotor when observed from above as sketched in Fig. 2.2.

For the NTNU turbine, the reference velocity measured in the empty wind tunnel was $u_{\text{ref,NTNU}} = 10\text{ m s}^{-1}$ at a turbulence intensity of $\text{TI} = \sigma_u/\langle u \rangle = 0.1$. For the ForWind turbine, the inflow velocity was $u_{\text{ref,ForWind}} = 7.5\text{ m s}^{-1}$ and $\text{TI} = 0.05$. In both cases, $u(t)$ was homogeneous within $\pm 6\%$ and the TI within $\pm 3\%$ on a vertical line at the turbine's position.

In this study we consider two-dimensional cuts through the wake, normal to the main flow direction at a downstream distance of $x/D = 6$ for both turbines as illustrated in Fig. 2.2. Data were acquired using a Dantec FiberFlow two-component laser Doppler anemometer (LDA) system, recording the u and v component of the flow. The accuracy is stated to be 0.04 % by

Turbine	Rotor diameter	Hub diameter	Blockage	TSR	Re_{tip}	Rotation	c_T
ForWind	0.580 m	0.077 m	5.4 %	6	$\approx 6.4 \times 10^4$	cw	0.87
NTNU	0.894 m	0.090 m	13 %	6	$\approx 1.1 \times 10^5$	ccw	0.87

Table 2.1: Summary of main turbine characteristics. The tip speed ratio (TSR) is based on the free-stream velocity u_{ref} at hub height. The Reynolds number at the blade tip, Re_{tip} , is based on the chord length at the blade tip and the effective velocity during turbine operation. For the ForWind turbine, $0.96 R$ was chosen as the radial position to account for the rounded blade tips. The blockage corresponds to the ratio of the rotor's swept area to the wind tunnel's cross-sectional area. The direction of rotation refers to observing the rotor from upstream, with (c)cw meaning (counter)clockwise. The thrust coefficients were measured at $\gamma = 0^\circ$ and corrected for thrust on the tower and support structure.

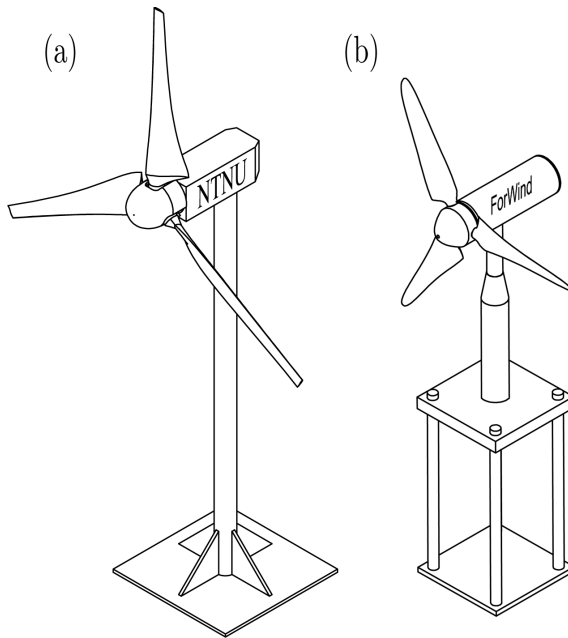


Figure 2.1: Technical drawings of the NTNU turbine (a) and the ForWind turbine (b).

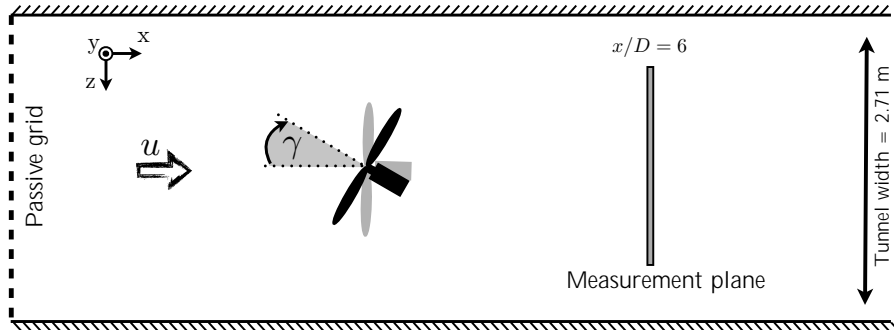


Figure 2.2: Sketch of the setup, top view. D denotes the respective rotor diameter as listed in Table 2.1.

the manufacturer. During turbine operation, the LDA system was traversed in the $y-z$ plane, normal to the main flow direction. Each measured plane consists of 357 points, 21 in the z direction ranging from $-D$ to $+D$ and 17 points in the y direction ranging from $-0.8 D$ to $0.8 D$; see Fig. 2.3. The resulting distance separating two points of measurement is thus $0.1 D$. For one location, 5×10^4 samples were recorded, resulting in time series of varying lengths of approximately 30 s. As can be seen, the NTNU turbine has a slimmer tower and nacelle relative to its rotor diameter than the ForWind turbine.

The grid of physically measured values was interpolated to a grid of $401 \times 321 \approx 129\,000$ points for further analyses. The distance between the interpolated grid points is thereby reduced to $0.005 D$. Natural neighbor interpolation is used, resulting in a smoother approximation of the distribution of data points [30].

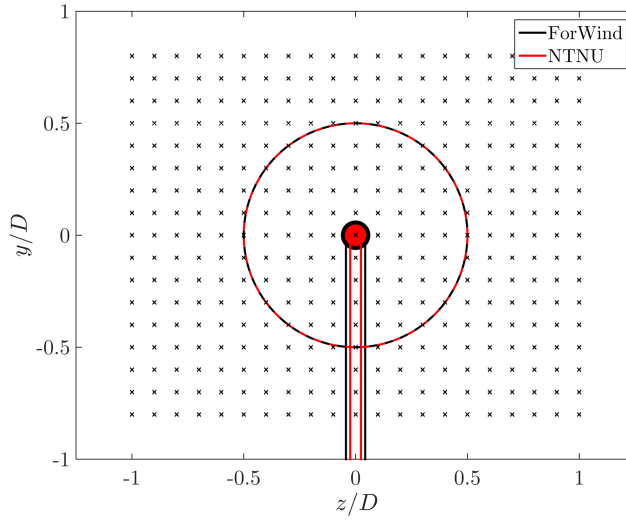


Figure 2.3: Non-dimensional measurement grid behind the rotor for $\gamma = 0^\circ$. The respective contours of the turbines are shown in black (ForWind) and red (NTNU). For the NTNU turbine the wind tunnel walls are located at $z/D = \pm 1.5$ and $y/D = \pm 1.0$; for the ForWind turbine they are located at $z/D = \pm 2.34$ and $y/D = \pm 1.56$.

2.2 Wake center detection

In order to quantify the lateral wake position, we compute the power of a potential downstream turbine as described by Schottler et al. [29]. A similar approach was shown by Vollmer et al. [31]. We define the potential power of a downstream turbine to be

$$P^* = \sum_{i=1}^{10} \rho A_i \langle u_i(t) \rangle_{A_i,t}^3. \quad (2.1)$$

The rotor area is divided into 10 ring segments. A_i is the area of the i th ring segment, and $\langle u_i(t) \rangle_{A_i,t}$ denotes the temporally and spatially averaged velocity in mean flow direction within the area A_i . P^* is estimated for 50 different hub locations in the range $-0.5 D \leq z \leq 0.5 D$, at hub height. We define the horizontal wake center as the z position resulting in the minimum of P^* . The procedure is illustrated in Fig. 2.4.

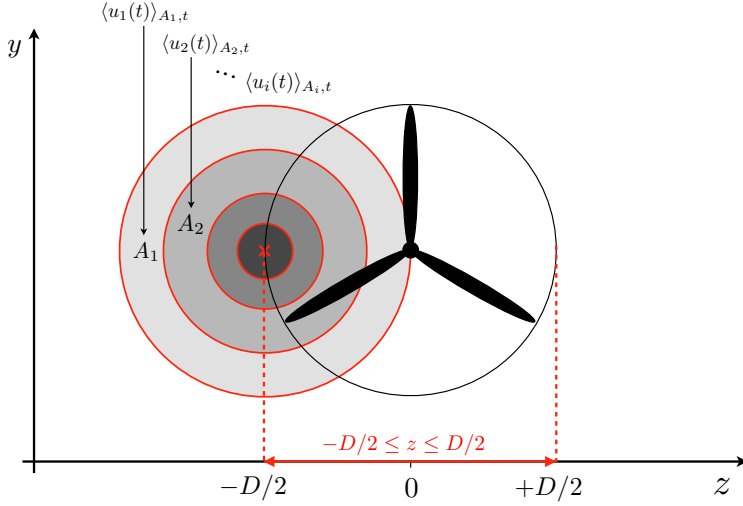


Figure 2.4: Illustration of the wake center detection method. The hub of a potential downstream turbine is located at the red \times . $\langle u_i(t) \rangle_{A_i,t}$ is the spatially and temporarily averaged u component of the velocity. The potential power P^* is calculated for each ring segment and then added up. This procedure is repeated for 50 horizontal hub locations \times , while the position resulting in the lowest value of P^* is interpreted as the wake center.

2.3 Examined quantities

TKE is defined by the fluctuations of the three velocity components as

$$k = 0.5 (\langle u'(t)^2 \rangle + \langle v'(t)^2 \rangle + \langle w'(t)^2 \rangle) , \quad (2.2)$$

where $u'(t)$ is the fluctuation around the mean of $u(t)$ so that

$$u(t) = \langle u(t) \rangle + u'(t) . \quad (2.3)$$

For brevity, we write $\langle u \rangle$ instead of $\langle u(t) \rangle$. As the third flow component w was not recorded, we assume $\langle w'(t)^2 \rangle \approx \langle v'(t)^2 \rangle$ so that Eq. (2.2) becomes

$$k^* = 0.5 (\langle u'(t)^2 \rangle + 2\langle v'(t)^2 \rangle) , \quad (2.4)$$

which will be used in further analyses. This approximation is discussed in Sect. 4 and supported by Fig. 4.1. For a thorough analysis of the wake turbulence, we examine velocity changes during a time lag τ and refer to them as velocity increments:

$$u_\tau(t) := u(t) - u(t + \tau) . \quad (2.5)$$

Investigating their probability density function (PDF) allows for scale-dependent analyses of turbulent flows, including all higher-order moments of u_τ , and hence all structure functions of order n , $S_\tau^n = \langle u_\tau^n \rangle$ of a velocity time series [19]. The impact of certain properties of velocity increment PDFs on wind turbines is to date a widely discussed topic in wind energy research [see, e.g., 25, 26, 32, 24]. For more details, we refer the reader to Morales et al. [22] or Schottler et al. [24]. Following Chillà et al. [33], the shape parameter

$$\lambda^2(\tau) = \frac{\ln(F(u_\tau)/3)}{4} \quad (2.6)$$

is used to quantify the shape of the distribution $p(u_\tau)$. $F(u_\tau)$ is the flatness of the time series of velocity increments:

$$F(u_\tau) = \frac{\langle (u_\tau - \langle u_\tau \rangle)^4 \rangle}{\langle u_\tau^2 \rangle^2} . \quad (2.7)$$

Equation (2.6) becomes zero for a Gaussian distribution; larger values correspond to broader, more heavy-tailed PDFs.

λ^2 is of practical relevance as it provides an analytical expression for the shape of $p(u_\tau)$. A discussion about the interpretation is given in Sect. 4. In this analysis, we compute λ^2 for timescales τ that relate to the rotor diameter D of the respective turbine. Using Taylor's hypothesis of frozen turbulence [34], the length scale $r = D$ is converted to the timescales τ :

$$\tau = r/\langle u \rangle = D/\langle u \rangle , \quad (2.8)$$

whereas $\langle u \rangle$ refers to the respective time series, resulting in varying values of τ within a wake. In order to compute $u_\tau(t)$ using Eq. (2.5), evenly spaced data are needed. The procedure applied to uniformly resample the non-uniform LDA data is described in the appendix. The approach results in a constant sampling rate for each wake.

3 Results

3.1 The non-yawed wakes

At first, we investigate wakes without yaw misalignment, $\gamma = 0^\circ$. Figure 3.1 shows the contour plots of the velocity component in mean flow direction $\langle u \rangle / u_{\text{ref}}$ for both turbines $6D$ downstream. The velocity deficits behind both turbines show a circular shape as expected, exceeding the rotor area, indicating a slight wake expansion. For both wakes, the minimum velocity is $\langle u \rangle / u_{\text{ref}} = 0.64$. Besides those general similarities, some differences are apparent. Both graphs show the tower wake, which is more strongly pronounced for the ForWind turbine. This can be explained by the larger tower diameter relative to the rotor diameter as shown in Fig. 2.3. Similarly, the four poles the ForWind turbine is placed on (cf. Fig. 2.1) are likely to enhance this effect. Figure 3.1 also reveals that the wake behind the ForWind turbine is slightly displaced vertically towards the ground. This effect can be linked to the tower wake, creating an uneven vertical transport of momentum as recently demonstrated by Pierella et al. [35]. Next, the NTNU wake shows areas of velocities exceeding $\langle u \rangle / u_{\text{ref}} = 1.1$ at the edges of the velocity deficit, especially in the corners of the contour plot. Very likely, this is a blockage effect as the measurement plane is significantly larger for the NTNU turbine, having a higher blockage ratio (13 % for the NTNU rotor, 5.4 % for the ForWind rotor). As suggested by Chen and Liou [36], blockage effects are expected for a cross-sectional blockage ratio exceeding 10 % when using model wind turbines, which is confirmed here for wake velocities. In order to better compare both contour plots, values exceeding $\langle u \rangle / u_{\text{ref}} = 1.1$ are masked. To further analyze the wake flows, Fig. 3.2 shows the contour plots of the TKE behind both turbines.

The contours of the TKE appear as circular shape, slightly larger than the rotor area. Behind the NTNU rotor, an outer ring of high TKE values appears more pronounced than in the center region. This observation is significantly less distinct for the ForWind turbine. The differences

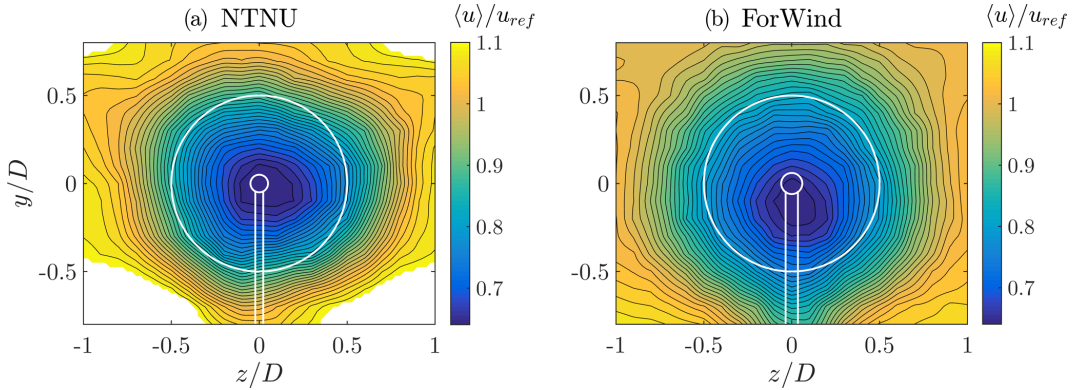


Figure 3.1: $\langle u \rangle / u_{ref}$ at $\gamma = 0^\circ$ for the NTNU turbine (a) and ForWind turbine (b). The white lines indicate the contours of the respective turbine. Values exceeding $\langle u \rangle / u_{ref} = 1.1$ are masked.

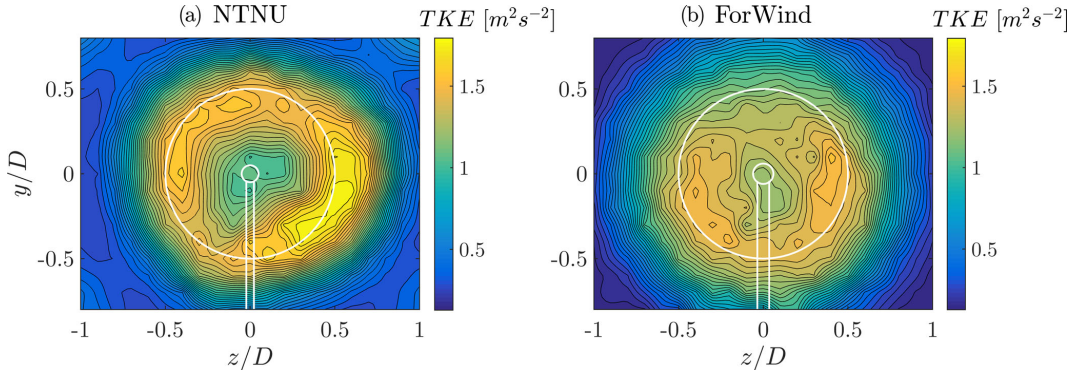


Figure 3.2: Turbulent kinetic energy (TKE) in $m^2 s^{-2}$ according to Eq. (2.4) for $\gamma = 0^\circ$. (a) NTNU turbine, (b) ForWind turbine.

of the pronounced ring arise most likely from the different blade geometries. The airfoil of the NTNU turbine (NREL S826) has higher lift coefficients for the relevant angles of attack and Reynolds numbers than the ForWind rotor (SD7003 airfoil). A comparison of both airfoils is given by Schottler et al. [29]. As a result, larger pressure differences between suction and pressure side of the blades are expected, resulting in more pronounced tip vortices shed from the NTNU rotor. Although those are already decayed at $x/D = 6$ [37], the tip vortices are likely to be the origin for a pronounced TKE at blade tip locations behind the NTNU rotor.

Further increasing in complexity and completeness of the wakes' stochastic description, Fig. 3.3 shows the contour plots of the shape parameter λ^2 behind both turbines. The length scale τ is related to the rotor diameter D of the respective turbine. The scale is transferred from space to time using Taylor's hypothesis; cf. Eq. (2.8). In both cases, the contours of λ^2 show a circular ring, whose diameter is significantly larger than the rotor diameter.

In order to quantify the qualitative shapes of the contours shown in Fig. 3.3, Fig. 3.4 shows the increment PDFs of the respective time series, $p(u_\tau)$, at the positions indicated by the red marks (\circ/\times) in Fig. 3.3. u_τ is normalized by the standard deviation, σ_τ , for better visual comparison. As shown in black, the positions behind the rotor tips, where $\lambda^2 \approx 0$, reveal increment PDFs very close to a Gaussian distribution, which holds for both turbines. For $z = D$, which lies within the ring of large λ^2 values, $p(u_\tau)$ strongly deviates from a Gaussian, showing a heavy-

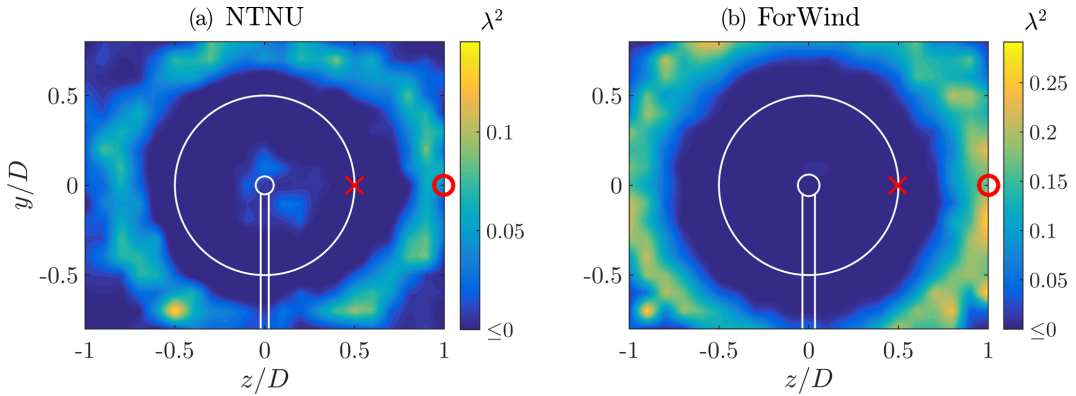


Figure 3.3: λ^2 for both turbines at $\gamma = 0^\circ$. The timescales τ correspond to the length scale of the rotor diameter; cf. Eq. (2.8). The red markings \times and \circ show measurement positions for which $p(u_\tau)$ were calculated as shown in Fig. 3.4. (a) NTNU turbine, (b) ForWind turbine. Note the different scaling.

tained distribution. Figure 3.4 further shows $p(u_\tau)$ based on the model proposed by Castaing [38]. Those distributions were evaluated based on the λ^2 values computed by Eq. (2.6) at $z = D$, visualizing exemplarily how well the distributions' shapes are grasped by λ^2 . Our results show that, depending on the examined quantity, different radial wake regions are of interest. To compare the varying spatial extensions of the three quantities' significant areas, Fig. 3.5 shows diagonal cuts through the respective contour plots for the non-yawed cases along the line $y = z$. The area of pronounced TKE approximately coincides with the rotor area. The notable peaks are separated by $\approx 0.86 D$ (NTNU) and $\approx 0.77 D$ (ForWind) and are significantly less pronounced behind the ForWind rotor as previously described. Clearly, the λ^2 peaks span a much larger distance: approximately $1.7 D$ (NTNU) and $2.0 D$ (ForWind). At their location, the velocity deficit has recovered to $\geq 90\%$ of the free-stream velocity in all cases. Thus, for a thorough description of wind turbine wakes, a much larger radial area is of interest as compared to a description restricted to mean values and the turbulent kinetic energy as often done in literature and wake models. An approximation of the lateral extension of high TKE and λ^2 values based on a Gaussian fit through the velocity deficit is given by $\mu \pm 1\sigma_u$ and $\mu \pm 2\sigma_u$, respectively, with μ being the mean value and σ_u the standard deviation of the fit. For illustration, the dotted lines in Fig. 3.5 mark the respective locations. It is shown that the radial areas of TKE and λ^2 can be related in this way to the velocity deficit. To get a feeling of the impact on potential downstream turbines, Fig. 3.6 compares $p(u_\tau)$ in absolute terms at a free-stream position ($y/D = 0.8$, $z/D = 1$) and at a position featuring high λ^2 values ($y/D = 0$, $z/D = 1$), exemplary for the ForWind turbine. It becomes clear that velocity increments exceeding 3 m s^{-1} occur much more frequently within the ring of high λ^2 values than in the free stream. Hereby we show that this radial position of the wake features significantly different flows than the free stream. To compare more visually, Fig. 3.7 shows the corresponding time series $u_\tau(t)$. Clearly, the spiky signature of extreme events becomes obvious in Fig. 3.7b, confirming that no free-stream condition is reached at $z/D = 1$.

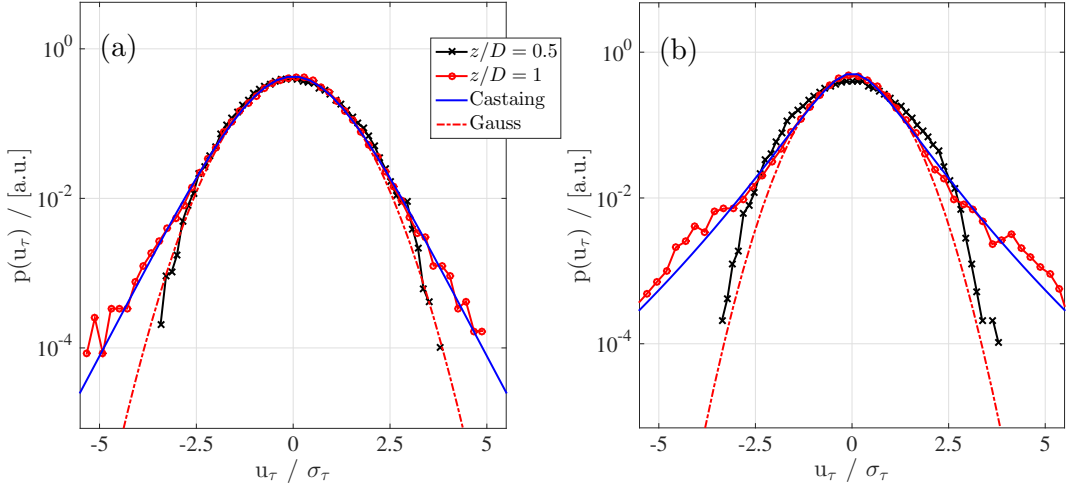


Figure 3.4: $p(u_\tau)$ of the time series at two measurement positions ($y = 0$, $z = D/2$; $y = 0$, $z = D$), corresponding to the red marks in Fig. 3.3. (a) NTNU turbine, (b) ForWind turbine, both at $\gamma = 0^\circ$. The timescales τ are related to the length scales of rotor diameters by Taylor's hypothesis using Eq. (2.8). For $z/D = 1$ (red curve) the Castaing distribution is shown with $\lambda_{\text{NTNU}}^2 = 0.046$ and $\lambda_{\text{ForWind}}^2 = 0.17$ [38]. A Gaussian fit is added to guide the eye.

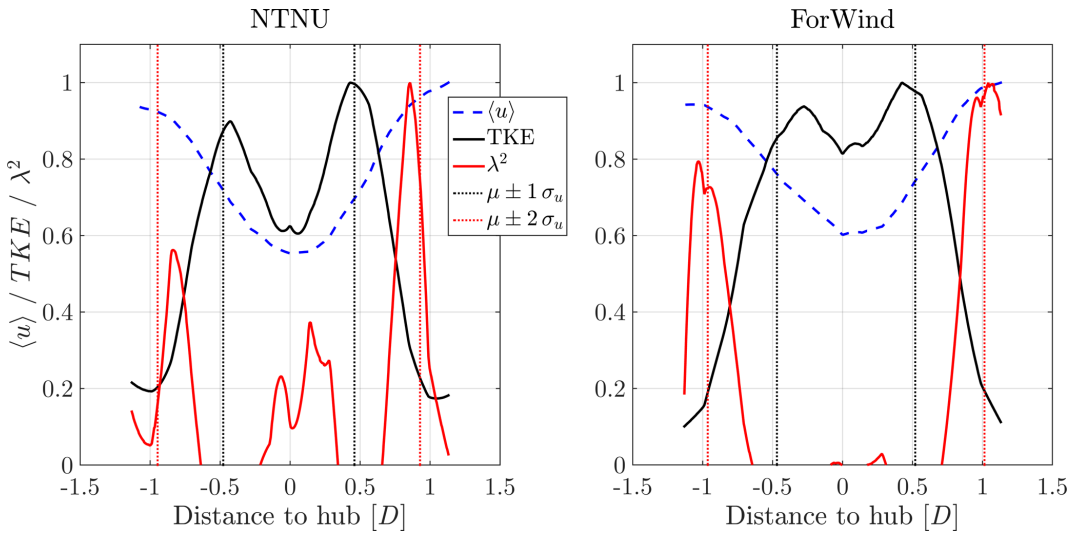


Figure 3.5: Diagonal cuts on the line $y = z$ through the contour plots for $\gamma = 0^\circ$. Values are normalized to their respective maximum. The vertical dotted lines mark $\mu \pm 1\sigma_u$ (black) and $\mu \pm 2\sigma_u$ (red) of a Gaussian fit through the velocity deficit shown in blue.

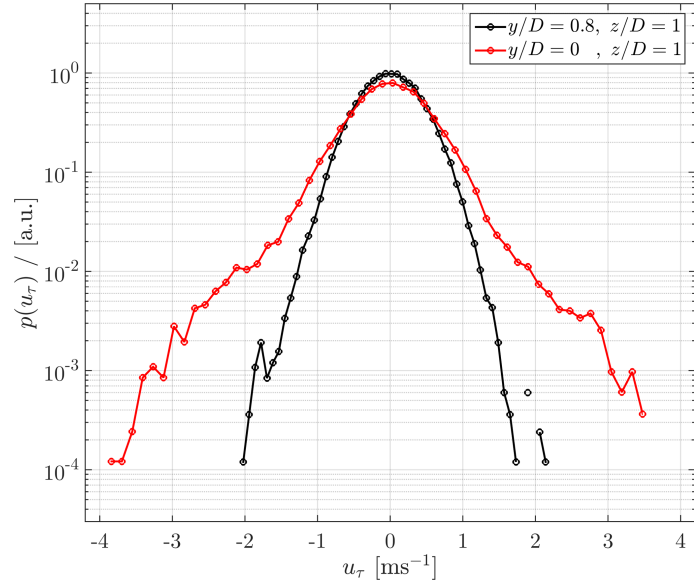


Figure 3.6: $p(u_\tau)$ of the free stream at $y/D = 0.8$, $z/D = 1$ and at $y/D = 0$, $z/D = 1$, exemplary for the ForWind turbine.

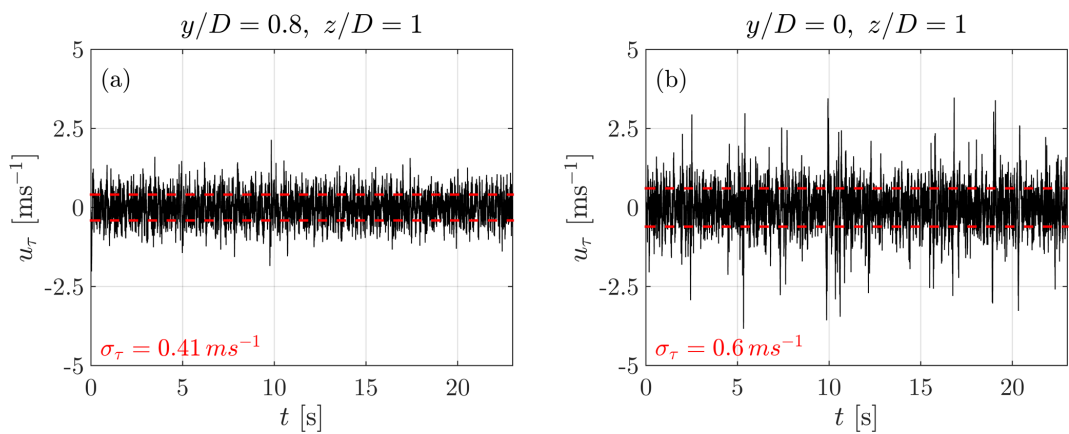


Figure 3.7: Time series of increments $u_\tau(t)$ for the positions $y/D = 0.8$, $z/D = 1$ (free stream, **a**) and $y/D = 0$, $z/D = 1$ (**a**). The standard deviations σ_τ are indicated in red.

3.2 Wakes during yaw-misalignment

During a yaw misalignment of $\gamma = \pm 30^\circ$, the velocity deficits behind both rotors are deflected and deformed as shown in Fig. 3.8 by the contours of the main flow component $\langle u \rangle / u_{\text{ref}}$.

The wakes are deflected sideways behind both turbines, whereas the lateral direction is dependent on the yaw angle's sign. This is expected due to a lateral thrust component of the rotor as a result of yaw misalignment, which has been observed and described in numerous studies, including Medici et al. [5], Jiménez et al. [3], Vollmer et al. [31] and Trujillo et al. [7]. The deflection of the velocity deficit is quantified using the approach described in Sect. 2.2; the results are listed in Table 3.1, including the resulting wake skew angles.

As Table 3.1 shows, the skew angles behind the ForWind turbine are equal apart from their sign for both directions of yaw misalignment. The NTNU rotor, however, shows slightly different deflection angles for $\gamma = 30^\circ$ and $\gamma = -30^\circ$, which is likely caused by blockage effects, which play a more significant role for the NTNU rotor due to the larger blockage ratio. This can also be seen in Fig. 3.8, where speed-up effects are visible in the corners. In Schottler et al. [29], where the same setup was used^a, the skew angle for the NTNU rotor decreased from $x/D = 3$ to $x/D = 6$, which is a further indication for wall effects due to blockage, especially during yaw misalignment. Furthermore, both values show smaller angles as for the ForWind turbine.

In Fig. 3.8, minimum $\langle u \rangle$ values are marked, showing a vertical transport of momentum in all cases. For $\gamma = 30^\circ$, the wake is moved upwards behind the NTNU turbines and downwards behind the ForWind rotor. Directions are reversed for $\gamma = -30^\circ$. Similar observations have been made by Bastankhah et al. [16]. The vertical transport is related to an interaction of a wake's rotation with the tower shadow/ground. Our results isolate this effect, as the direction of vertical transport is opposite comparing both turbines, having an opposite direction of rotation. The fact that the vertical transport is stronger behind the ForWind rotor further supports this explanation as the tower wake is more pronounced due to the larger tower diameter and the structure the turbine is placed on. A deformation of the velocity deficit to a curled "kidney" shape is observed for both turbines during yaw misalignment, whereas it is slightly more pronounced behind the ForWind turbine. The curled shape behind a wind turbine model in yaw has previously been observed by Howland et al. [12] using a drag disc of 30 mm diameter and by Bastankhah et al. [16] using a rotating turbine model of 150 mm diameter. Figure 3.8 confirms these findings on two further scales. For a better comparison of the curled shape of the velocity deficit during yaw misalignment, we apply the following parametrization, exemplarily shown in Fig. 3.9a for the ForWind turbine at $\gamma = 30^\circ$: data points of horizontal cuts through the wake, $\langle u \rangle_{y=\text{const.}}$, are fitted by a polynomial. The procedure is repeated for values of y ranging from $-0.4 D$ to $0.4 D$.

Turbine	Yaw angle [°]	Wake center [D]	Skew angle [°]
NTNU	30	-0.28	≈ -2.6
NTNU	-30	0.32	≈ 3.0
ForWind	30	-0.38	≈ -3.6
ForWind	-30	0.38	≈ 3.6

Table 3.1: Wake center location as computed by the approach described in Sect. 2.2 with corresponding skew angles.

^aIn Schottler et al. [29], the quantification was carried out for a sheared inflow. Other aspects of the setup were equal.

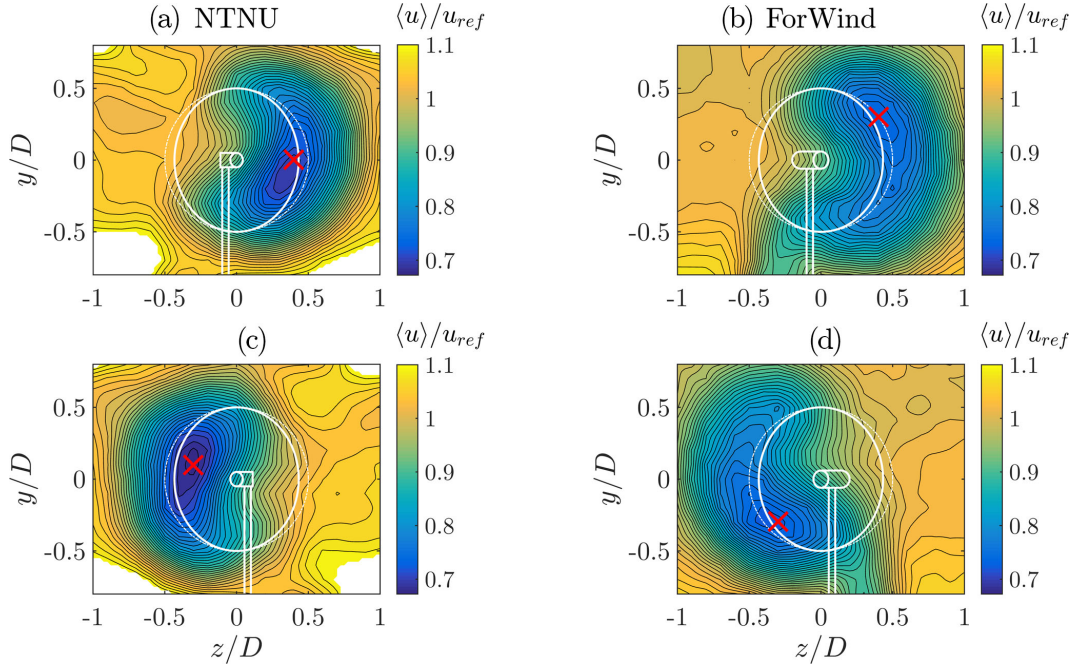


Figure 3.8: $\langle u \rangle / u_{ref}$ during yaw misalignment. (a, b) $\gamma = -30^\circ$, (c, d) $\gamma = 30^\circ$. (a, c) NTNU turbine, (b, d) ForWind turbine. The solid white lines indicate the contours of the respective turbine, while the dashed lines denote the rotor area without yaw misalignment. The red \times marks the position of minimum measured velocity $\langle u \rangle$. Values exceeding 1.1 are masked for better comparison.

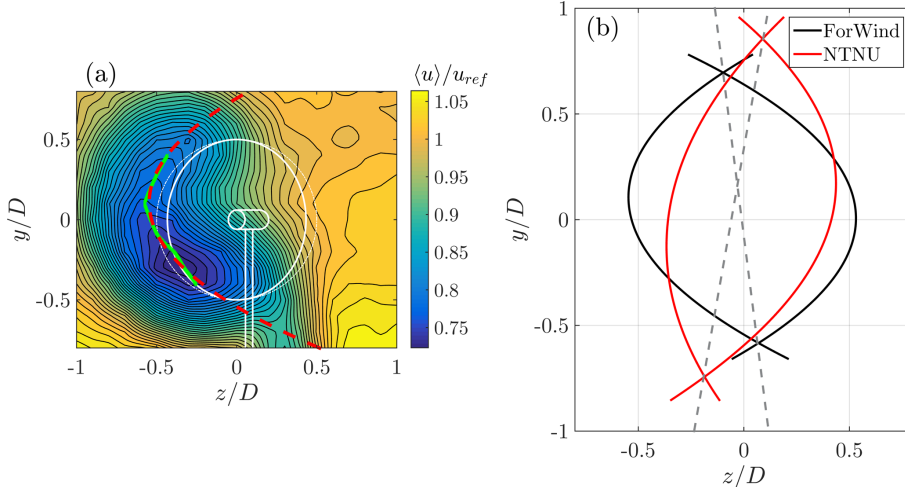


Figure 3.9: (a) Example of parameterizing the curled shape of the velocity deficit. The green markings show minimal velocities of a polynomial function used to fit the interpolated data points in a horizontal line; y is a constant. The red dashed line shows a quadratic fit based on the green markings. (b) Visualization of the curled shapes of the velocity deficits. For both turbines, the cases $\gamma = \pm 30^\circ$ are shown. Dashed lines show a visualization of the wakes tilt, connecting the respective intersections of the curves.

The positions of the polynomials' minima (green marks) are fitted by a quadratic function (red line). Figure 3.9b shows the comparison of both turbines for $\gamma = \pm 30^\circ$.

As already seen in Fig. 3.8, the wakes behind the ForWind turbine are deflected further and the curled shape is more strongly pronounced, which can be attributed to blockage effects. Figure 3.9b also shows that the wakes behind both turbines are slightly tilted. Looking at the black curves (ForWind turbine), an asymmetry can be noticed as the curves are tilted towards the left, while the red curves are tilted towards the right. This is illustrated by the gray dashed lines in Fig. 3.9b which connect the points of intersection for $\gamma = \pm 30^\circ$. Not shown in detail here, the same effect was observed for different inflow conditions and other downstream distances, using the same setup and methods as in this study. Similar asymmetries have been observed by Bastankhah et al. [16] for positive and negative yaw angles, which is explained by an interaction of a wake's rotation with the tower wake and the ground. By using turbines of opposite rotation direction, we can attribute the asymmetries in vertical transport and tilt in opposite direction for $\gamma = \pm 30^\circ$ to the rotation of rotor and wake.

Adding TKE and λ^2 contours during yaw misalignment, Fig. 3.10 shows all three examined quantities, exemplary at a yaw misalignment of $\gamma = -30^\circ$, for both turbines. The shapes of the TKE contours are deformed similarly to $\langle u \rangle$. A curled shape evolves, and the differences between both turbines as described for $\gamma = 0^\circ$ are still notable during yaw misalignment. Similarly, the circular rings of high λ^2 values are deformed to a curled shape at $\gamma = \pm 30^\circ$. Thus, the general effect of heavy-tailed increment PDFs surrounding the velocity deficit in a wake is stable against yaw misalignment and the resulting inflow variations at the rotor blades. Further, this finding is confirmed in large-eddy simulations (LES) performed at the Universidad de la Repùblica, Uruguay, shown in the Appendix. It is found to be a general effect as it is observed for all wakes considered, independent of yaw misalignment or turbine design. The red markings in Fig. 3.10 show the approximation of the radial extension of the TKE and λ^2 based on $\mu \pm 1\sigma_u$ and $\mu \pm 2\sigma_u$. μ and σ_u correspond to Gaussian fits of the velocity deficits at various horizontal cuts (y is a constant) from $y/D = -0.5$ to $y/D = 0.5$, with μ being the fit's mean value and σ_u the standard deviation. It is shown that the method results in quite good first-order approximations, even during yaw misalignment.

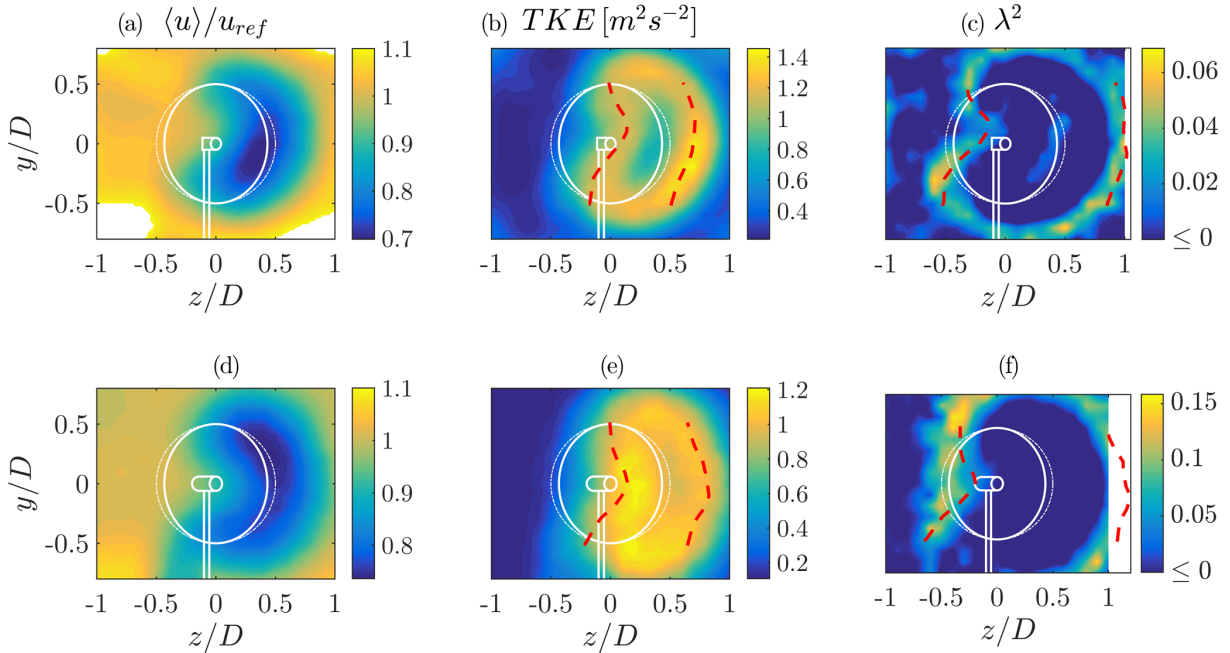


Figure 3.10: $\langle u \rangle / u_{ref}$ (a, d), TKE (b, e) and λ^2 (c, f) for $\gamma = -30^\circ$ behind the NTNU turbine (a–c) and the ForWind turbine (d–f). The timescale for λ^2 corresponds to the length scale of the rotor diameter. The red marks show the approximation of the respective parameter's radial extension based on $\mu \pm 1\sigma_u$ (TKE, b, e) and $\mu \pm 2\sigma_u$ (λ^2 , a, d) as described in Sect. 3.1.

4 Discussion

In this study the characterization of yawed and non-yawed wind turbine wakes is investigated and extended by taking into account a further turbulence measure, namely the intermittency parameter λ^2 . We find heavy-tailed distributions of velocity increments in a ring area surrounding the velocity deficit and areas of high TKE in a wind turbine wake. Thus, the definition of a wake width strongly depends on the quantities taken into account as the ring area features significantly different statistics than the free stream. The heavy-tailed distributions are the statistical description of large velocity changes over given timescales and are transferred to turbines in terms of loads and power output. This has been shown experimentally [24], numerically [25] and in a field study by Milan et al. [26]. Consequently, our findings should be considered in wind farm layout optimization approaches, where a wake's width is a crucial parameter for radial turbine spacing. As layouts are being optimized regarding power and loads, the latter might be significantly affected by taking into account intermittency and the resulting increased wake width. Possibly, the ring of non-Gaussian velocity increments is a result of instable flow states,

where the flow switches between a wake and free stream state. Behind a rotor, the wake characteristics dominate the flow. Outside the wake, free-stream properties are dominant. In the transition zone, a switching between both flow states is believed to result in heavy-tailed velocity increments and therefore high λ^2 values. Generally, λ^2 will be larger for smaller scales τ , which is a known feature of turbulence [19]. Care should be taken when interpreting λ^2 as an indicator for an increment PDF's shape. Here, we use the shape parameter as a qualitative indicator. For a more quantitative analysis, one has to consider the increment PDF of a time series directly. This is done in Fig. 3.4 exemplarily for chosen points; however, in order to include all time series of a wake, using λ^2 allows for a much better visualization and comparison.

Figure 3.10 shows that the velocity deficit is deflected laterally during yaw misalignment, so that a potential in-line downstream turbine would exhibit a power increase as more undisturbed flow hits the rotor area at $z/D \approx -0.5$. Looking at the λ^2 contours, however, shows that areas of non-Gaussian velocity increments are now deflected onto the rotor area. This becomes important when assessing the applicability of active wake steering approaches, as a gain in power has to be balanced with a potential load increase, affecting maintenance costs and the lifetime of turbines overall. It should be noted that it is to date not clear to what extent high TKE levels and intermittent force data are affecting common ways of fatigue and extreme-load calculations. This important aspect needs to be addressed in future works. It might depend quite strongly on details such as considered timescales. In our opinion, it is likely that non-Gaussian inflow is linked to drive train, gear box or pitch system failures, especially because those inflow characteristics are not accounted for in standard models used in the design process of wind turbines.

The velocity deficit in mean flow direction $\langle u \rangle$ deforms to a curled kidney shape during yaw misalignment. Consequently, horizontal cuts through the wake are insufficient when characterizing wakes behind yawed rotors, resulting in misleading and incomplete conclusions when quantifying wake deflections by yaw misalignment. The parametrization of the wake's curl shown in Fig. 3.9 should not be interpreted as a quantification. Instead, we use the described approach to better compare multiple curled wakes as done in Fig. 3.9b. Our analyses include the velocity deficit in mean flow direction, the turbulent kinetic energy and the shape parameter λ^2 . The turbulence intensity in the wakes revealed very comparable results to the TKE, which is why we restrict our analyses to the TKE. For the majority of wakes considered, only two flow components were recorded. For one exemplary wake, however, all three components are available, allowing the assumption of $\langle v'(t)^2 \rangle \approx \langle w'(t)^2 \rangle$ to be examined; cf. Eq. (2.4). Figure 4.1 shows the contours of k and k^* as well as $\langle v'(t)^2 \rangle$ versus $\langle w'(t)^2 \rangle$ for all measurement positions. Both contour plots show neglectable differences, confirming the approximation. This is further supported by a high correlation coefficient of 0.94 between $\langle v'(t)^2 \rangle$ and $\langle w'(t)^2 \rangle$. Besides the lateral deflection, a vertical transport of the velocity deficit is observed for both turbines during yaw misalignment. Using counter-rotating turbines, this effect could be attributed to the wake's rotation and its interaction with the tower wake. In full-scale scenarios, the ground, wind shear and rotor tilt would further contribute to the effect. For potential floating turbines, a pitch motion will deflect the wake upwards; see Rockel et al. [39]. This vertical deflection will interact with the vertical transport shown in Fig. 3.8. Consequently, the direction of yaw misalignment is believed to be of importance when applying the concept of wake steering to wind farm controls. This confirms findings by Fleming et al. [40] and Schottler et al. [41], reporting an asymmetric power output of a two-turbine case with respect to the upstream turbine's angle of yaw misalignment. One should bear in mind that the inflow turbulence intensities are different regarding both turbines. We want to point out that the influence of inflow turbulence on the wake deflection is investigated by Bartl et al. [27], showing no significant effects.

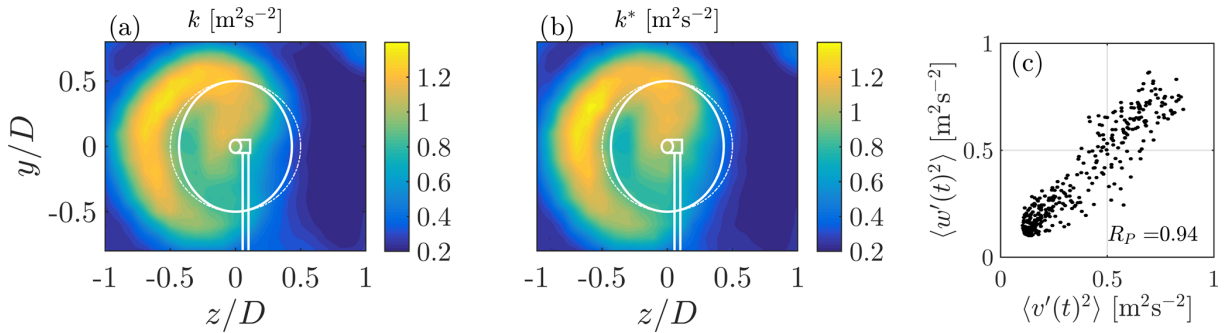


Figure 4.1: (a) TKE k (cf. Eq. 2.2), (b) TKE k^* (cf. Eq. 2.4) and (c) $\langle v'(t)^2 \rangle$ vs. $\langle w'(t)^2 \rangle$ for all measurement positions. R_P is Pearson's correlation coefficient. Data are based on a wake $6D$ behind the NTNU turbine and $\gamma = 30^\circ$.

5 Conclusions

This work shows an experimental investigation of wind turbine wakes, using two different model wind turbines. The analyses include the main flow component, the turbulent kinetic energy and two-point statistics of velocity increments, quantified by the shape parameter λ^2 . Yaw angles of $\gamma = \{0^\circ, \pm 30^\circ\}$ are considered at a downstream distance of $x/D = 6$. Generally, the results of $\langle u \rangle$, the TKE and λ^2 compare well for both model turbines. Minor differences could be ascribed to the more prominent blockage (12.8 vs. 5.4 %) in the NTNU setup, confirming findings by Chen and Liou [36] even for wake velocity measurements, who state blockage effects can be neglected for a blockage ratio $\leq 10\%$. An outer ring of heavy-tailed velocity increments surrounds the velocity deficit and areas of high TKE in a wind turbine wake. The wake features significantly non-Gaussian velocity increment distributions in areas where the velocity deficit recovered nearly completely. For $\gamma = 0^\circ$, the ring has a diameter of approximately $1.7D$ – $2D$, depending on the turbine. Based on a Gaussian fit through the velocity deficit, the radial location of intermittent increments can be approximated by $\mu \pm 2\sigma_u$ (μ being the mean value, σ_u the standard deviation of the fit), making a wake considerably wider when taking two-point statistics into account. This observation becomes important in wind farm layout optimization and active wake steering approaches through yaw misalignment. During yaw misalignment, the circular shape of a wake is deformed to a curled kidney shape. A method for parameterizing the curl shape was introduced. The lateral wake deflection was quantified, resulting in skew angles of $\pm 3.6^\circ$ at $\pm 30^\circ$ for the smaller rotor and 3.0 and -2.6° for the larger rotor. Furthermore, vertical momentum transport in the wake during yaw misalignment was observed. The direction of vertical transport is dependent on the direction of yaw misalignment. Using counter-rotating turbines, the effect could be attributed to an interaction of a wake's rotation with the tower wake in this study.

Appendix

Data preprocessing

In order to study intermittency using the shape parameter λ^2 , uniformly sampled data are needed when applying Eq. (2.5). As the LDA measurement result in non-uniformly sampled data points, appropriate preprocessing is necessary. In the following, the procedure is described that results in uniformly sampled data points. It is exemplarily applied to the data of an arbitrarily chosen wake. The time separating two samples of a time series is Δt . For one time series, $(\Delta t)^{-1}$ is plotted for all samples in Fig. 5.1a. The corresponding histogram is shown in Fig. 5.1b. The point corresponding to 40 % of all events is marked by the red dashed line and is referred to as F_S . In this example, $F_S \approx 1.17 \text{ kHz}$.

This procedure is repeated for all 357 time series contained in one plane of measurement. Figure 5.2 shows F_S for all time series, with the mean value indicated.

The mean value of all F_S values in one plane will be used as the sampling frequency to resample the time series in one plane uniformly; an exemplary result is shown in Fig. 5.3.

Data points are interpolated linearly onto a vector of uniformly spaced instants defined by the new sampling rate $\langle F_S \rangle$. It should be noted that the analyses of velocity increments were performed for different constant sampling rates without showing any significant effect on the results.

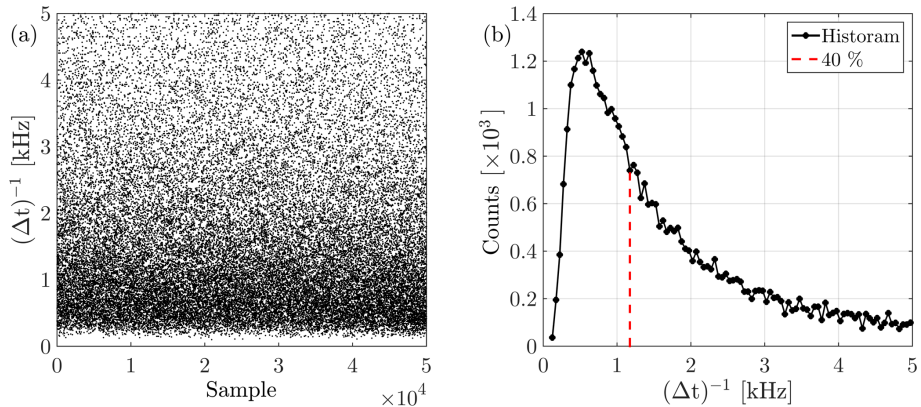


Figure 5.1: $(\Delta t)^{-1}$ for all samples (a) with the respective histogram (b), where the maximum value is marked by the red dashed line.

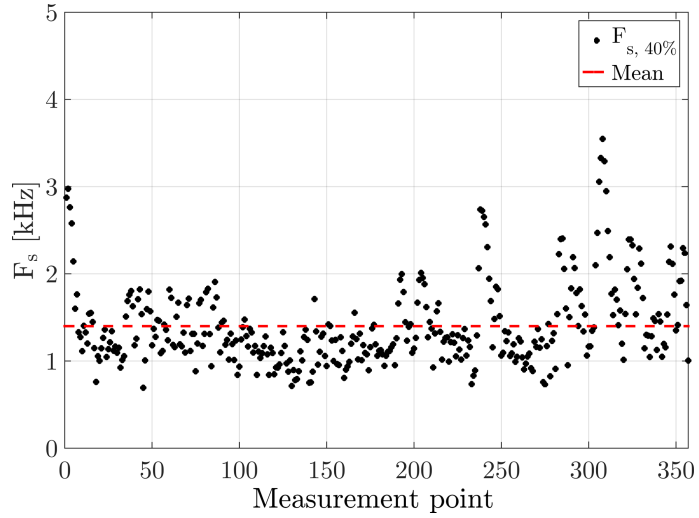


Figure 5.2: F_s for all 357 time series of one wake; the mean value is indicated in red: $\langle F_s \rangle = 1.4 \text{ kHz}$.

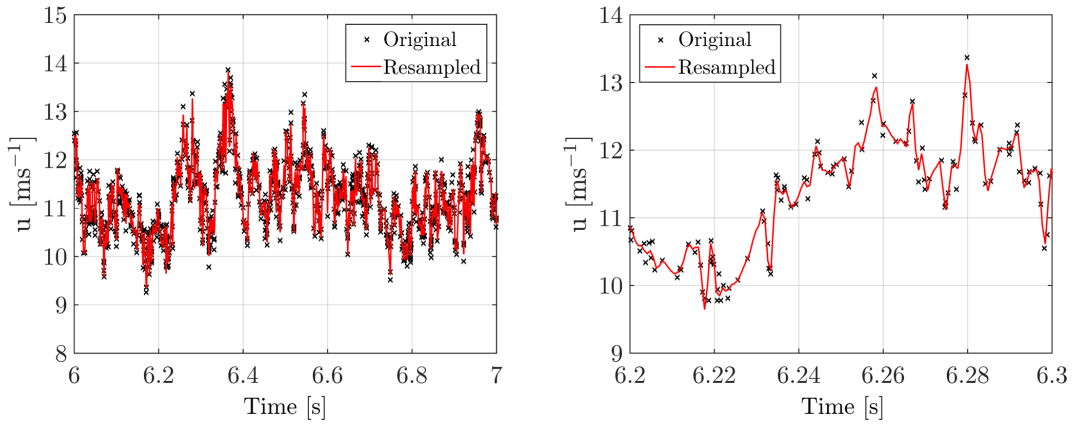


Figure 5.3: Examples of resampling the raw data $u(t)$ uniformly with $\langle F_s \rangle = 1.4 \text{ kHz}$.

LES simulations

Within the scope of the blind test 5 project, LES simulations of the ForWind turbine in a very comparable setup were performed, where the inflow features a vertical shear as opposed to the experiments shown in this paper. The incompressible flow solver caffa3d.MBRI as described by Mendina et al. [42] and Draper et al. [43] was used to obtain the results shown in Fig. 5.4. The turbine was modeled by actuator lines. The top row shows $x/D = 3$; $x/D = 6$ is shown beneath. The contours of $\langle u \rangle / u_{\text{ref}}$ and λ^2 reveal very similar results to the experimental data. Qualitatively, it can be concluded that the outer ring of high λ^2 values and thus heavy-tailed distributions of velocity increments that surrounds the velocity deficit of a wake can be correctly predicted in LES simulations.

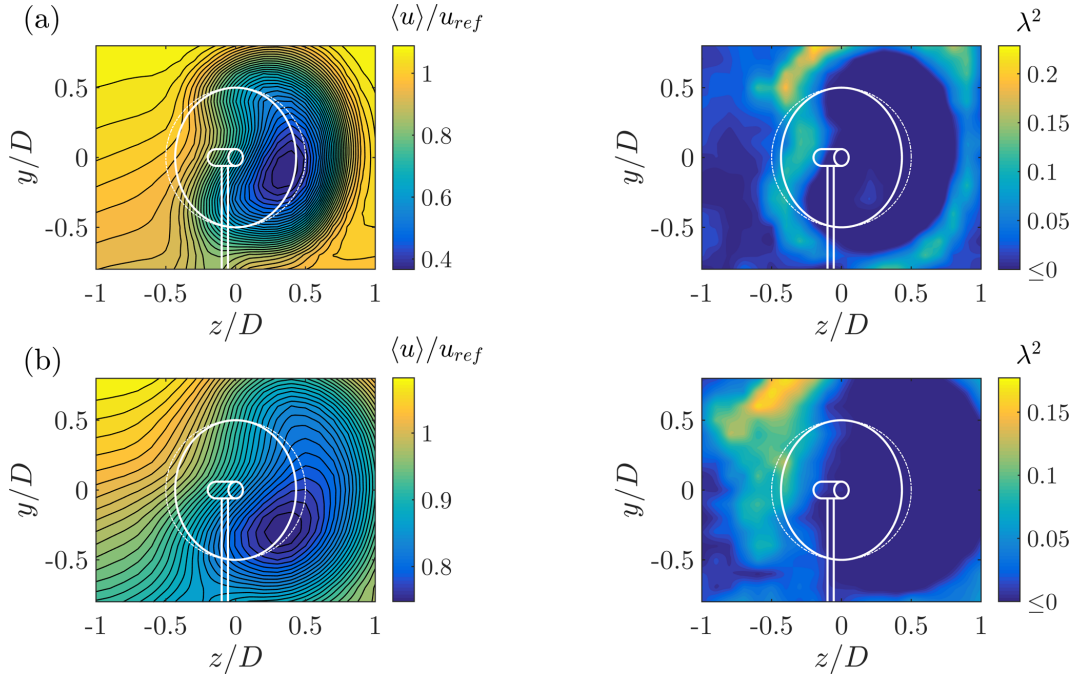


Figure 5.4: LES data of the wakes 3D (a) and 6D (b) behind the ForWind turbine at $\gamma = 30^\circ$. In contrast to the experiments presented in this paper, the inflow in the LES domain features a vertical shear with comparable turbulence intensity. The timescales of τ for the λ^2 calculations correspond to the length scale of the rotor diameter.

Bibliography

- [1] R. J. Barthelmie, S. Pryor, S. T. Frandsen, K. S. Hansen, J. Schepers, K. Rados, W. Schlez, A. Neubert, L. Jensen, and S. Neckelmann. Quantifying the impact of wind turbine wakes on power output at offshore wind farms. *Journal of Atmospheric and Oceanic Technology*, 27(8):1302–1317, 2010.
- [2] T. Burton, D. Sharpe, N. Jenkins, and E. Bossanyi. *Wind Energy Handbook*. John Wiley and Sons, 2001.
- [3] Á. Jiménez, A. Crespo, and E. Migoya. Application of a les technique to characterize the wake deflection of a wind turbine in yaw. *Wind energy*, 13(6):559–572, 2010.
- [4] P. a. Fleming, P. M. O. Gebraad, S. Lee, J. W. van Wingerden, K. Johnson, M. Churchfield, J. Michalakes, P. Spalart, and P. Moriarty. Evaluating techniques for redirecting turbine wakes using SOWFA. *Renewable Energy*, 70(June):211–218, 2014.
- [5] D. Medici and P. Alfredsson. Measurements on a wind turbine wake: 3d effects and bluff body vortex shedding. *Wind Energy*, 9(3):219–236, 2006.
- [6] F. Campagnolo, V. Petrović, C. Bottasso, and A. Croce. Wind tunnel testing of wake control strategies. In *Proceedings of the American Control Conference*, volume 2016-July, 2016.
- [7] J.-J. Trujillo, J. K. Seifert, I. Würth, D. Schlipf, and M. Kühn. Full field assessment of wind turbine near wake deviation in relation to yaw misalignment. *Wind Energy Science Discussions*, (January):1–17, 2016.

- [8] J. Schottler, A. Hölling, J. Peinke, and M. Hölling. Wind tunnel tests on controllable model wind turbines in yaw. *34th Wind Energy Symposium*, (January):1523, 2016.
- [9] P. M. O. Gebraad, F. W. Teeuwisse, J. W. van Wingerden, P. A. Fleming, S. D. Ruben, J. R. Marden, and L. Y. Pao. Wind plant power optimization through yaw control using a parametric model for wake effects-a CFD simulation study. *Wind Energy*, 19(1):95–114, jan 2014.
- [10] P. Fleming, J. Annoni, J. J. Shah, L. Wang, S. Ananthan, Z. Zhang, K. Hutchings, P. Wang, W. Chen, and L. Chen. Field test of wake steering at an offshore wind farm. *Wind Energy Science*, 2(1):229–239, may 2017.
- [11] G. España, S. Aubrun, S. Loyer, and P. Devinant. Wind tunnel study of the wake meandering downstream of a modelled wind turbine as an effect of large scale turbulent eddies. *Journal of Wind Engineering and Industrial Aerodynamics*, 101:24–33, 2012.
- [12] M. F. Howland, J. Bossuyt, L. A. Martínez-Tossas, J. Meyers, and C. Meneveau. Wake structure in actuator disk models of wind turbines in yaw under uniform inflow conditions. *Journal of Renewable and Sustainable Energy*, 8(4), 2016.
- [13] C. L. Bottasso, F. Campagnolo, and V. Petrović. Wind tunnel testing of scaled wind turbine models: Beyond aerodynamics. *Journal of Wind Engineering and Industrial Aerodynamics*, 127:11–28, 2014.
- [14] A. Abdulrahim, E. Anik, and O. Uzol. Experimental Investigation of the Wake Flow Field of a Model Wind Turbine Rotor with Tip Injection. In *33rd Wind Energy Symposium*, number January, pages 1–10, Reston, Virginia, jan 2015. American Institute of Aeronautics and Astronautics.
- [15] S. Rockel, J. Peinke, M. Hölling, and R. B. Cal. Wake to wake interaction of floating wind turbine models in free pitch motion: An eddy viscosity and mixing length approach. *Renewable Energy*, 85:666–676, 2016.
- [16] M. Bastankhah and F. Porté-Agel. Experimental and theoretical study of wind turbine wakes in yawed conditions. *Journal of Fluid Mechanics*, 806(1):506–541, nov 2016.
- [17] J. M. Jonkman, S. Butterfield, W. Musial, and G. Scott. *Definition of a 5-MW reference wind turbine for offshore system development*. National Renewable Energy Laboratory Golden, CO, 2009.
- [18] C. Bak, F. Zahle, R. Bitsche, and T. Kim. The DTU 10-MW reference wind turbine. *Danish wind power* . . . , 2013.
- [19] U. Frisch. *Turbulence : the legacy of A.N. Kolmogorov*, volume 1. Cambridge university press, 1995.
- [20] F. Boettcher, C. Renner, H. P. Waldl, and J. Peinke. On the statistics of wind gusts. *Boundary-Layer Meteorology*, 108(1):163–173, 2003.
- [21] L. Liu, F. Hu, X.-L. Cheng, and L.-L. Song. Probability Density Functions of Velocity Increments in the Atmospheric Boundary Layer. *Boundary-Layer Meteorology*, 134(2):243–255, 2010.

- [22] A. Morales, M. Wächter, and J. Peinke. Characterization of wind turbulence by higher-order statistics. *Wind Energy*, 15(3):391–406, 2012.
- [23] G. A. M. van Kuik, J. Peinke, R. Nijssen, D. Lekou, J. Mann, J. N. Sørensen, C. Ferreira, J. W. van Wingerden, D. Schlipf, P. Gebraad, H. Polinder, A. Abrahamsen, G. J. W. van Bussel, J. D. Sørensen, P. Tavner, C. L. Bottasso, M. Muskulus, D. Matha, H. J. Lindeboom, S. Degraer, O. Kramer, S. Lehnhoff, M. Sonnenschein, P. E. Sørensen, R. W. Künneke, P. E. Morthorst, and K. Skytte. Long-term research challenges in wind energy – a research agenda by the european academy of wind energy. *Wind Energy Science*, 1(1):1–39, 2016.
- [24] J. Schottler, N. Reinke, A. Hölling, J. Whale, J. Peinke, and M. Hölling. On the impact of non-Gaussian wind statistics on wind turbines – an experimental approach. *Wind Energy Science*, 2(1):1–13, jan 2017.
- [25] T. Mücke, D. Kleinhans, and J. Peinke. Atmospheric turbulence and its influence on the alternating loads on wind turbines. *Wind Energy*, 14(2):301–316, 2011.
- [26] P. Milan, M. Wächter, and J. Peinke. Turbulent character of wind energy. *Physical Review Letters*, 110(13):1–5, 2013.
- [27] J. Bartl, F. Mühle, J. Schottler, L. Sætran, J. Peinke, M. Adaramola, and M. Hölling. Wind tunnel experiments on wind turbine wakes in yaw: effects of inflow turbulence and shear. *Wind Energy Science*, 3(1):329–343, jun 2018.
- [28] J. Bartl and L. Sætran. Blind test comparison of the performance and wake flow between two in-line wind turbines exposed to different turbulent inflow conditions. *Wind Energy Science*, 2(1):55–76, feb 2017.
- [29] J. Schottler, F. Mühle, J. Bartl, J. Peinke, M. S. Adaramola, L. Sætran, and M. Hölling. Comparative study on the wake deflection behind yawed wind turbine models. *Journal of Physics: Conference Series*, 854:012032, may 2017.
- [30] I. Amidror. Scattered data interpolation methods for electronic imaging systems: a survey. *Journal of Electronic Imaging*, 11(2):157, 2002.
- [31] L. Vollmer, G. Steinfeld, D. Heinemann, and M. Kühn. Estimating the wake deflection downstream of a wind turbine in different atmospheric stabilities: an LES study. *Wind Energy Science*, 1(2):129–141, sep 2016.
- [32] J. Berg, A. Natarajan, J. Mann, and E. G. Patton. Gaussian vs non-Gaussian turbulence: impact on wind turbine loads. *Wind Energy*, 17(April 2013):n/a–n/a, 2016.
- [33] F. Chillà, J. Peinke, and B. Castaing. Multiplicative Process in Turbulent Velocity Statistics: A Simplified Analysis. *Journal de Physique II*, 6(4):455–460, 1996.
- [34] J. Mathieu and J. Scott. *An introduction to turbulent flow*. Cambridge University Press, 2000.
- [35] F. Pierella and L. Saetran. Wind tunnel investigation on the effect of the turbine tower on wind turbines wake symmetry. *Wind Energy*, 17(April 2013):657–669, jun 2017.
- [36] T. Chen and L. Liou. Blockage corrections in wind tunnel tests of small horizontal-axis wind turbines. *Experimental Thermal and Fluid Science*, 35(3):565–569, apr 2011.

- [37] P. E. Eriksen and P. Å. Krogstad. Development of coherent motion in the wake of a model wind turbine. *Renewable Energy*, 108:449–460, 2017.
- [38] B. Castaing, Y. Gagne, and E. J. Hopfinger. Velocity probability density functions of high Reynolds number turbulence. *Physica D: Nonlinear Phenomena*, 46(2):177–200, 1990.
- [39] S. Rockel, E. Camp, J. Schmidt, J. Peinke, R. B. Cal, and M. Hölling. *Experimental study on influence of pitch motion on the wake of a floating wind turbine model*, volume 7. 2014.
- [40] P. Fleming, P. M. Gebraad, S. Lee, J.-W. Wingerden, K. Johnson, M. Churchfield, J. Michalakes, P. Spalart, and P. Moriarty. Simulation comparison of wake mitigation control strategies for a two-turbine case. *Wind Energy*, 2014.
- [41] J. Schottler, A. Hölling, J. Peinke, and M. Hölling. Brief Communication : On the influence of vertical wind shear on the combined power output of two model wind turbines in yaw. (2016):1–5, 2017.
- [42] M. Mendina, M. Draper, A. P. Kelm Soares, G. Narancio, and G. Usera. A general purpose parallel block structured open source incompressible flow solver. *Cluster Computing*, 17(2):231–241, 2014.
- [43] M. Draper, A. Guggeri, and G. Usera. Validation of the Actuator Line Model with coarse resolution in atmospheric sheared and turbulent inflow. *Journal of Physics: Conference Series*, 753(8), 2016.

Paper 3

Wind tunnel tests on controllable model wind turbines in yaw^a

JANNIK SCHOTTLER, AGNIESZKA HÖLLING, JOACHIM PEINKE and MICHAEL HÖLLING

Abstract. The investigation of multiple wind turbine's interactions through their wakes remains of great relevance and needs further understanding. We present wind tunnel experiments on the influence of yaw misalignment on the power output of a two-turbine array. In this study, model wind turbines were used that comprise a collective pitch control system as well as a load control for partial load conditions. The two identical turbines were set up in the wind tunnel in streamwise displacement, whereas the yaw angle of the front turbine was varied systematically. The power output of the individual turbines and the array as a whole is investigated. We show that the power output of the downstream turbine is asymmetric with respect to the front turbine's yaw angle. Further, this asymmetry holds for the combined power of the turbine array, which could be increased by changing the yaw angle as opposed to the case of perfect yaw alignment.

1 Introduction

Nowadays, the majority of wind turbines is installed in wind farms in order to achieve an economical optimum of utilizing a certain area for wind energy purposes. Due to changing wind directions, this inevitably leads to aerodynamic interactions between the turbines. A downstream turbine operating in the wake of at least one upstream turbine is subjected to 'wake effects'. Those, most importantly, are: (i) a decreased wind speed causing a reduction in the energy yield of downstream turbines; and (ii) an increased turbulence level, which potentially increases loads and shortens the lifetime of turbines operating within wakes [1, 2, 3, 4]. Field studies have shown that average power losses in large-scale wind farms are of the order of 10-20 % [5], and can reach up to 40 % for individual turbines in extreme cases [6]. In order to reduce power losses in wind farms, different strategies of farm control have been proposed. In a study by Corten et al., a reduction of the axial induction factor by pitch variation showed the potential of a power increase within a wind farm experimentally [7]. Another concept is the wake deflection by a wind turbine in yaw, redirecting the velocity deficit partly around a downstream turbine. The concept of wake deflection has been studied in LES simulations [8] and was validated in wind tunnel experiments using model wind turbines [9]. Further, simulations have shown the potential of improving the power output of a wind farm by active wake control [10, 11]. As the previous works showed great potential of the concept, further investigations are necessary to gain a full understanding of the effect and the impact on downstream turbines. Experimental studies focused on quantifying the wake properties of a turbine in yaw [9, 12, 13]. Simulations included the impact on downstream turbines, focusing on the overall power generation, which showed a great relevance of the *direction* of a turbine's yaw [11]. This aspect, to our knowledge, has not been covered in previous experimental studies and therefore needs validation. This paper aims

^aPublished as JANNIK SCHOTTLER, AGNIESZKA HÖLLING, JOACHIM PEINKE and MICHAEL HÖLLING: Wind tunnel tests on controllable model wind turbines in yaw, *34th Wind Energy Symposium, San Diego, USA, 1523, 2016*.

to further understand the impact of a wind turbine in yaw on a second turbine operating in its wake and to approve our experimental methods. Hereby, the power output is in focus.

2 Model wind turbines

For experimental investigations, two identical model wind turbines as shown in Figure 2.1 were used, each with a rotor diameter D of 0.58 m and a hub height of 0.48 m. The clockwise rotating (facing downstream), horizontal axis turbines are equipped with a collective pitch and a load control system, which are described in sections 2.1 and 2.2. The nacelle comprises the pitching mechanism and a DC generator (Faulhaber 3863H048CR) equipped with a magnetic encoder that allows measurements of the rotational velocity. The rotor blades were produced by a vacuum-casting method and are based on the SD7003 airfoil profile with a twist of 31° from root to tip. This showed good results regarding the power coefficient for low Reynolds numbers in simulations [14] and experimental studies using model wind turbines [15].

Data acquisition and turbine control were realized by a National Instruments NI-9074 cRIO real time controller equipped with modules for stepper motor control (NI-9512), analog input (NI-9215), analog output (NI-9264) and digital input/output (NI-9401) in combination with in-house built LabView software. The power of the model turbines, $P = \omega T$, is based on the generator's torque T , which is proportional to the electric current I according to the generator's specifications. I is obtained by measuring the voltage drop U_S across a shunt-resistor of 0.1Ω . Therewith, the power becomes $P := \omega k \frac{U_S}{0.1 \Omega}$, where $k = 79.9 \text{ mN A}^{-1}$ is the proportionality constant relating the generator's electric current to its torque.



Figure 2.1: Model wind turbine.

2.1 Pitching Mechanism

An encoder-equipped stepper motor (Faulhaber AM2224-R3-4.8-36) initiates the collective pitching of the blades. Via a coupling, the stepper motor's shaft is connected to a thread, whose counter part is placed in a slider on the turbine's main shaft. The rotation of the motor's shaft is transmitted to a linear movement of the slider, which causes the rotation of the blade mountings by connecting links. This principle is in accordance with cyclic blade pitching as it is used in helicopter flight control. Figure 2.2 shows a schematic drawing of this principle. The optical encoder (Faulhaber PE 22-120) of the stepper motor allows precise adjustment and monitoring of pitch angle changes using a feedback loop. Changes of the pitch angle of $\Delta\beta \leq 30^\circ$ can be obtained. In this study, a closed loop pitch control was not used. However, the main advantage of being able to finely tune the pitch angle in this study, is the possibility to precisely adjust a turbine's point of operation prior to the experiment.

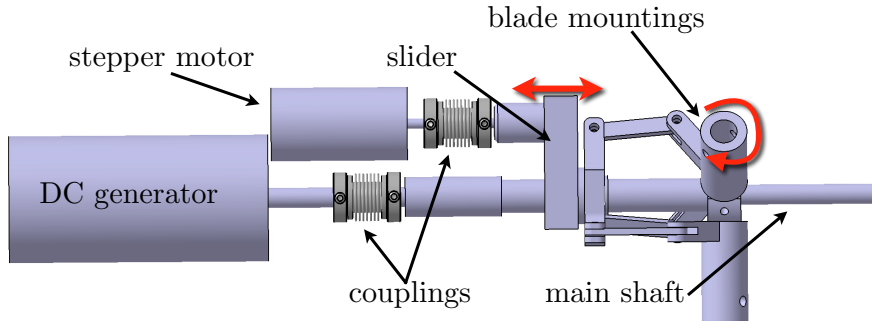


Figure 2.2: Principle of the pitching mechanism.

2.2 Load Control

The objective of a control system in partial load conditions is to maximize the energy yield of a wind turbine for the prevailing wind speed. Consequently, the power coefficient c_p is maximized [16]. In case of the model turbine, the load control is realized using a field-effect transistor (FET). The generator's electrical load, and thereby its torque, is influenced by adapting the voltage U_{FET} applied to the FET (HITFET BTS 141), which alters the electric circuit's current. Exemplary, Figure 2.3 shows the effect of changing U_{FET} during constant inflow conditions on the torque, rotational velocity, tip-speed ratio (TSR) and the power output of the turbine. The setup allows

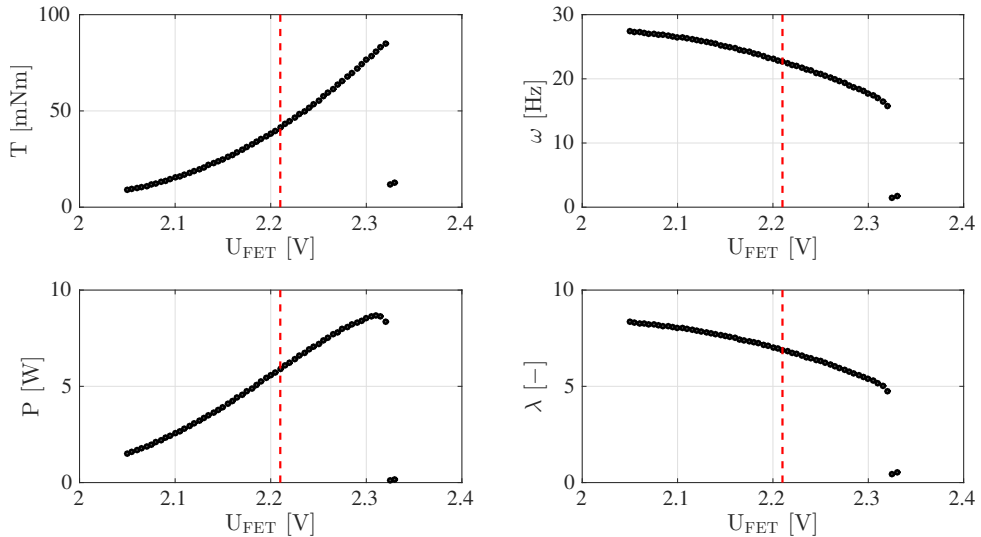


Figure 2.3: Examples of the effect of varying U_{FET} on the model turbine at $u = 6 \text{ m s}^{-1}$. Each data point is the mean value of 60 s measurements at 2 kHz. For reasons of accuracy, ω was recorded at 100 Hz. The dashed red lines indicate $U_{\text{FET}} = 2.21 \text{ V}$, which is the fixed voltage used in the tests shown in Figure 2.4, left column.

an accurate tuning of the quantities presented in Figure 2.3. This concept is the basis of the load control, which is using a standard PI-controller, whereas the manipulative variable is the voltage U_{FET} . The process variable is the TSR, in this example based on the hub height wind speed obtained by a hot wire probe 0.4 m upstream of the rotor. Figure 2.4 shows the turbine's reaction to step-like velocity changes with inactive (left column) and active (right column) load

control. In the controlled case, the set point was $\lambda_{set} = 5.5$. During the inactive case, U_{FET} was kept constant at 2.21 V exemplary, which is marked in Figure 2.3.

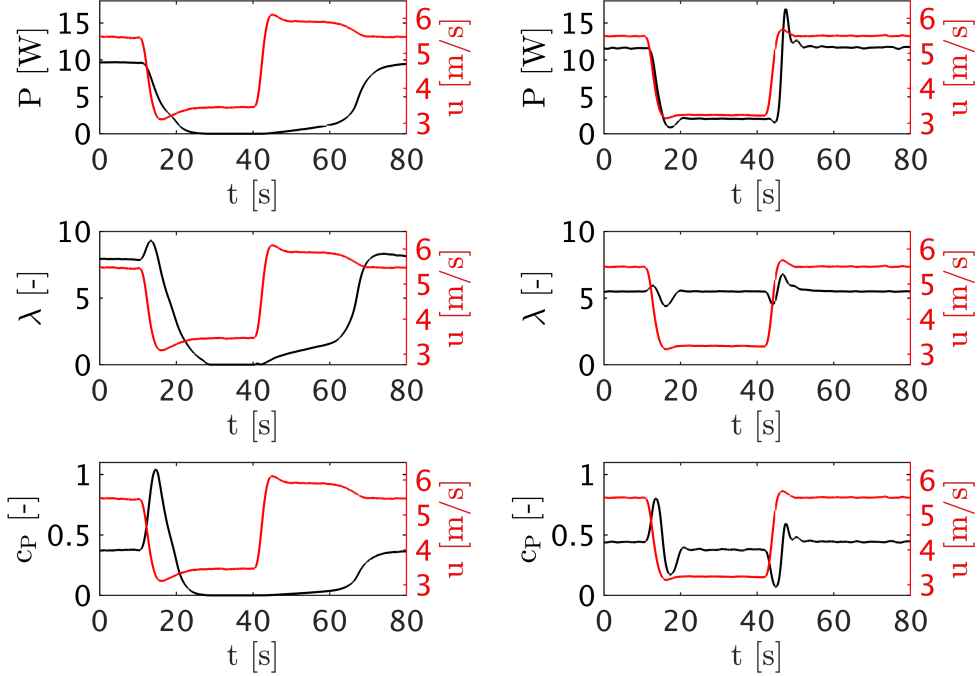


Figure 2.4: Tests of the control system in partial load conditions. The left column shows the power, TSR, power coefficient and velocity over time with the load control being inactive and $U_{FET} = \text{const.} = 2.21 \text{ V}$. The right column shows the same quantities for the active control case, whereas $\lambda_{set} = 5.5$.

Without active control (left column, Figure 2.4), the turbine cannot follow the sudden decrease in wind speed as the TSR drops into stall and finally to zero as the rotor is stagnating. Consequently, P and c_P become zero as well. After the velocity change at $t \approx 40 \text{ s}$, λ and therewith the power and c_P slowly increase until the initial values are reached again, approx. 30 s after the velocity increase. With active control however (right column, Figure 2.4), the power output follows the velocity changes with a certain inertia- and controller-caused time lag of approx. 1.5 s. The TSR remains constant as expected since it is the process variable of the controller and the set point remains constant. As a result, the power coefficient is maximized, revealing slightly larger values for higher velocities ($\approx 44\%$ for 5.5 m s^{-1} as opposed to $\approx 39\%$ for 3.3 m s^{-1})^a. The comparison with the non-controlled case strengthens the advantage of an adaptive control system for investigations of changing inflow conditions.

^aFurther characterizations showed that the maximal power coefficient achievable increases with the prevailing wind speed. Most likely, this is caused by mechanical losses, whose impact becomes less significant with increasing velocity.

3 Experimental Setup

Both turbines were placed in the wind tunnel of the University of Oldenburg with an outlet of $1\text{ m} \times 0.8\text{ m}$ (width \times height) and an open test section of 5 m length, displaced in streamwise direction as sketched in Figure 3.1. The distance x is variable, in this study we investigate the

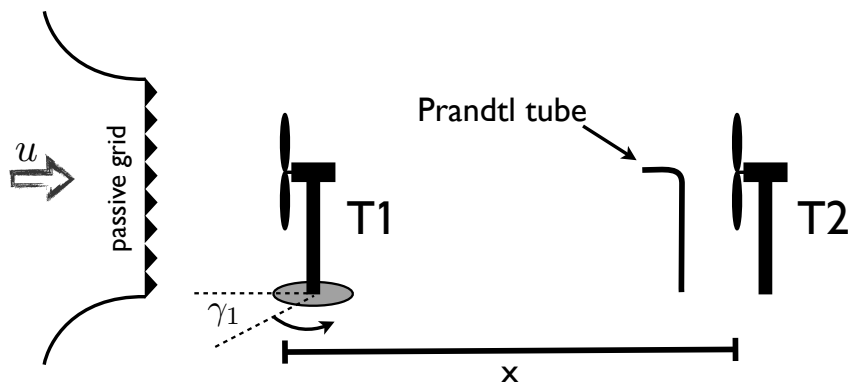


Figure 3.1: Sketched wind tunnel setup. The scales do not match for visualization purposes. γ_1 indicates a positive yaw angle.

case $x/D = 3$. The outlet of the wind tunnel was equipped with an active grid as described by Weitemeier et al. [17]. The grid was used passively in open configuration with a blockage of nearly 4.8 %, which resulted in a turbulence intensity of approx. 3 % at hub height and $u \approx 8\text{ m s}^{-1}$. The front turbine T1 was placed on a stepper motor driven turning table that allows a variation of the yaw angle. The wind speed u_2 , which was the input wind speed for the load control of T2 as described in section 2.2, was measured by a Prandtl tube 0.35 m in front of the downstream turbine at hub height^a. Thereby, T2 maximized its power coefficient while the inflow conditions were subject to change due to varying yaw angles of the front rotor.

At $u < 8\text{ m s}^{-1}$ and optimal point of operation of T1, the velocity prevailing at the downstream turbine was below cut-in. At the same time, at $u \geq 8\text{ m s}^{-1}$, the front turbine would operate above rated power, which was defined as $P_r := 25\text{ W}$. Consequently, the power of T1 had to be limited by pitching the blades so that $P_1 \leq P_r$, to ensure that both turbines are exposed to conditions between cut-in and cut-out. During the experiments, the pitch angles of both turbines were kept constant, while U_{FET} of T1 was constant at 2.46 V. The downstream turbine T2 utilized the load control as described in section 2.2, whereas $\lambda_{\text{set}} := 6.5$ in this case.

In this study, yaw angles of the front turbine of $-40^\circ \leq \gamma_1 \leq 40^\circ$ in steps of $\Delta\gamma_1 = \pm 2^\circ$ were examined. Positive yaw angles are defined by a rotation of the turbine to the left hand side around

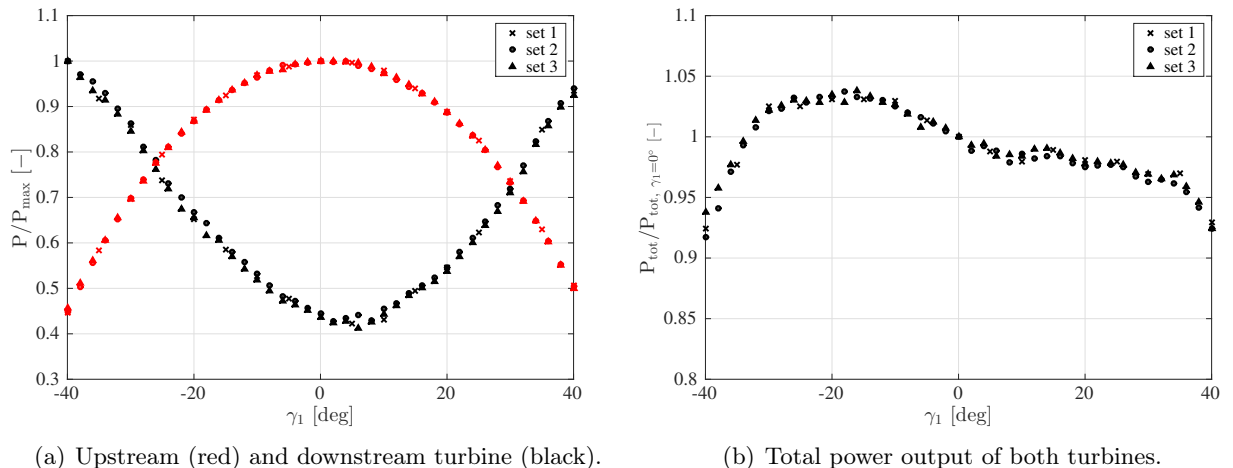
^aThe position where the wind speed is measured is a trade-off between two aspects. If the distance from sensor to turbine is too large, the control is based on flow conditions that do not match the actual inflow of the turbine. However, closer to the downstream turbine, the velocity measurement becomes more effected by the blockage of the rotor.

its vertical axis, facing upstream (comp. Figure 3.1). For each value of γ_1 , data was acquired at 1 kHz for 60 s. For reasons of accuracy, the rotational velocity was measured at 100 Hz. A time lag of 20 s between a change of γ_1 and data acquisition ensured stable flow conditions while data was recorded. Due to this procedure, the stand-alone control of the downstream turbine becomes convenient, as the torque and thereby the TSR do not have to be set manually to the optimal operating point. Thus, this automatized setup allows reproducible investigations of the depicted scenario.

4 Results

Figure 4.1 shows the power output of T1, T2 and the total power output of both turbines combined at the distance $x/D = 3$. P_1 and P_2 are normalized to their respective maximal value while P_{tot} is normalized to $P_{\text{tot}}(\gamma_1 = 0^\circ)$. Measurements were carried out three times to ensure reproducibility. Further, during set one and set three, yaw angles were changed from -40° to $+40^\circ$ while set two examined the vica verca direction in order to judge hysteresis effects. As all three sets follow the same pathway, no evidence of hysteresis effects are found and reproducibility is seen as confirmed.

Figure 4.1(a) clearly shows that changing T1's yaw angle significantly influences the performance



(a) Upstream (red) and downstream turbine (black).

(b) Total power output of both turbines.

Figure 4.1: Normalized power output of the upstream turbine (**a, red symbols**), downstream turbine (**a, black symbols**) and the total power output (**b**) for changing yaw angles of the front turbine γ_1 at $x/D = 3$.

of the downstream turbine operating in the wake. This is in accordance with basic rotor theory, as changing the yaw angle to $\gamma_1 \neq 0^\circ$ reduces the axial induction factor of the rotor, which is directly linked to its wake velocity [16]. Additionally, a rotor in yaw induces a thrust component orthogonal towards the axis of rotation. Consequently, the wake is deflected sideways as the orthogonal thrust component is compensated [16].

Further, Figure 4.1(a) shows an asymmetry of P_2 with respect to γ_1 . The minimal power

is measured at $\gamma_1 \approx 6^\circ$. Consequently, the *direction* of a change in yaw becomes relevant as $P_2(\gamma_1) \neq P_2(-\gamma_1)$. Exemplary, $P_2/P_{2,\max}$ at $\gamma_1 = 30^\circ$ is approx 0.71, while it is nearly 0.86 at $\gamma_1 = -30^\circ$.

Figure 4.1(b) shows the total power of both turbines combined, normalized to $P_{\text{tot}}(\gamma_1 = 0^\circ)$. In contrast to P_2 , P_1 is symmetric with respect to γ_1 . Consequently, the sum of both becomes asymmetric. One further result is that the maximum of the total power P_{tot} is not located at $\gamma_1 = 0^\circ$, which means that the concept of wake deflection by yawing the upstream rotor is increasing the overall power output of the array under the described setup and conditions, compared to the initial case of $\gamma_1 = 0^\circ$. The maximum power is located at $\gamma_1 \approx -18^\circ$, revealing a power increase of nearly 4% compared to the non-yawed case. Further, it can be seen that the direction of the upstream rotor's yaw angle is of great relevance, as $\gamma_1 = +18^\circ$ does not increase the total power output, but decreases it.

5 Discussion

It is important to be aware of the shortcomings of the work presented. As for all scaled wind tunnel experiments, upscaling is a valid concern. Due to wind tunnel limitations, the highest achievable Reynolds number of this study is $Re \approx 3.2 \times 10^5$ (based on the rotor diameter and the wind speed at hub height). Compared to full scale turbines, the Reynolds number is smaller by a factor of nearly 170. The vast majority of experimental investigations using model wind turbines face similar issues, however, previous studies showed that general effects including wake deflection by yaw misalignment can be reproduced [9]. Next, the ratio between the rotor area and the cross-sectional area of the test section is about 33%. This may cause an interference between the non-accelerated air outside the measuring volume and the wake behind the rotor, which expands orthogonally with respect to the main flow direction. Despite the limitations, the results show a good agreement with findings of Fleming et al.[11] and Gebraad et al.[10], who investigated a comparable scenario in CFD studies. Especially the general shapes and the asymmetries of both graphs in Figure 4.1 are in accordance as well as the possibility to increase the combined power by the concept of yaw misalignment. However, although the general shapes are alike, the asymmetries occur at yaw angles of opposite sign, e.g. the total power is increased at negative yaw angles in the experiment presented, and at positive yaw angles in the CFD study. In accordance, the minimal power of the downstream turbine is found at $\gamma_1 > 0^\circ$ in the experiment, while it is minimal at $\gamma_1 < 0^\circ$ in the simulations. A likely cause of this finding is the vertical wind shear of both setups: In the CFD study, a neutral atmospheric boundary layer, with a relatively low surface roughness (0.001) is used[11]. In the experiment, the hub height was not in the vertical center of the wind tunnel outlet but slightly above it. As a result, the top tip of the blades was closer to the edge of the open test section than the bottom tip. Consequently, the upstream turbine was exposed to a 'reversed' vertical velocity profile. Figure 5.1 shows the inflow condition at the position of the upstream rotor without any turbine installed.

Here it can be seen that due to the shorter distance to the edge of the test section, the velocity near the rotor's top tip is decreased to a further extend as compared to the bottom tip. As the asymmetry in Figure 4.1 may be caused by the interaction of a vertical wind shear and the wake's rotation, the inverse profile shown in Figure 5.1 may explain the difference between the presented experiments and the CFD study by Fleming et al. [11] and Gebraad et al.[10]. Previous studies

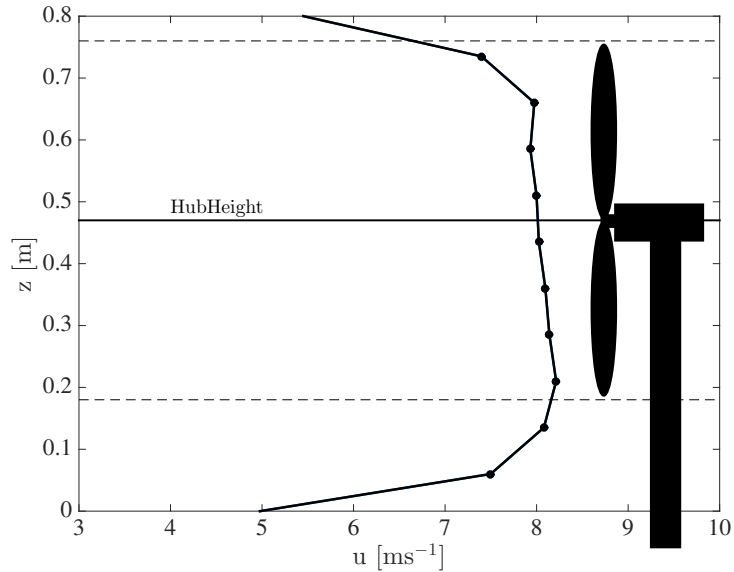


Figure 5.1: Inflow condition at the upstream rotor's position, without any turbine installed. The solid line indicates the hub height, the dashed lines the edges of the rotor tips. The ordinate corresponds to the extension of the wind tunnel outlet of 0.8 m in vertical direction. Data points (black circles) are mean values of simultaneous hot wire measurements at 2 kHz.

showed a strong influence of the boundary layer on the wake development of wind turbines [2]. Supplementary, our results motivate further research on the influence of different boundary layer properties, such as vertical velocity shear, on wake development and the concept of active wake control by yaw misalignment.

6 Conclusion and Future Work

Two pitch and load controlled model wind turbines were used to investigate the effect of yaw misalignment on the power output of a downstream turbine and the array as a whole. The turbines were installed in the wind tunnel in streamwise displacement. Yaw angles of the upstream turbine of $\pm 40^\circ$ were examined, while the downstream turbine utilized a standalone load control. In this PI-controller based approach, the TSR is the constant set point, allowing an automatic adaption of the turbines point of operation during varying inflow conditions. We present a convenient setup that allows the investigation of the effect of multiple turbine parameters on the performance of both turbines. In this study, an asymmetry of the downstream turbine's power with respect to the upstream turbine's yaw angle was found, which is in accordance with numerical simulations of a comparable scenario. However, differences to simulation results motivate a more detailed investigation of the influence of a vertical velocity shear on the examined setup, which is planned in future studies. Furthermore, the concept of wake deflection by yawing resulted in a power increase of the array compared to the initial case without yaw misalignment for this scenario.

Bibliography

- [1] A. Crespo, J. Hernandez, and S. Frandsen. Survey of modelling methods for wind turbine wakes and wind farms. *Wind energy*, 2(1):1–24, 1999.
- [2] L. P. Chamorro and F. Porté-Agel. A wind-tunnel investigation of wind-turbine wakes: boundary-layer turbulence effects. *Boundary-layer meteorology*, 132(1):129–149, 2009.
- [3] M. Luhur, J. Peinke, J. Schneemann, and M. Wächter. Stochastic modeling of lift and drag dynamics under turbulent wind inflow conditions. *Wind Energy*, 2014.
- [4] P. Milan, M. Wächter, and J. Peinke. Stochastic modeling and performance monitoring of wind farm power production. *Journal of Renewable and Sustainable Energy*, 6(3):033119, 2014.
- [5] R. J. Barthelmie, K. Hansen, S. T. Frandsen, O. Rathmann, J. Schepers, W. Schlez, J. Phillips, K. Rados, A. Zervos, E. Politis, et al. Modelling and measuring flow and wind turbine wakes in large wind farms offshore. *Wind Energy*, 12(5):431–444, 2009.
- [6] R. J. Barthelmie, S. Pryor, S. T. Frandsen, K. S. Hansen, J. Schepers, K. Rados, W. Schlez, A. Neubert, L. Jensen, and S. Neckelmann. Quantifying the impact of wind turbine wakes on power output at offshore wind farms. *Journal of Atmospheric and Oceanic Technology*, 27(8):1302–1317, 2010.
- [7] G. Corten, P. Schaak, and E. Bot. More power and less loads in wind farms:‘heat and flux’. In *European Wind Energy Conference & Exhibition, London, UK*, 2004.
- [8] Á. Jiménez, A. Crespo, and E. Migoya. Application of a les technique to characterize the wake deflection of a wind turbine in yaw. *Wind energy*, 13(6):559–572, 2010.
- [9] D. Medici and P. Alfredsson. Measurements on a wind turbine wake: 3d effects and bluff body vortex shedding. *Wind Energy*, 9(3):219–236, 2006.
- [10] P. Gebraad, F. Teeuwisse, J. Wingerden, P. Fleming, S. Ruben, J. Marden, and L. Pao. Wind plant power optimization through yaw control using a parametric model for wake effects—a cfd simulation study. *Wind Energy*, 2014.
- [11] P. Fleming, P. M. Gebraad, S. Lee, J.-W. Wingerden, K. Johnson, M. Churchfield, J. Michalakes, P. Spalart, and P. Moriarty. Simulation comparison of wake mitigation control strategies for a two-turbine case. *Wind Energy*, 2014.
- [12] W. Haans. Wind turbine aerodynamics in yaw: unravelling the measured rotor wake. 2011.
- [13] M. Adaramola and P.-Å. Krogstad. Experimental investigation of wake effects on wind turbine performance. *Renewable Energy*, 36(8):2078–2086, 2011.
- [14] J. N. Counsil and K. Goni Boulama. Low-reynolds-number aerodynamic performances of the naca 0012 and selig-donovan 7003 airfoils. *Journal of Aircraft*, 50(1):204–216, 2013.
- [15] Y. Odemark. Wakes behind wind turbines-studies on tip vortex evolution and stability. 2012.
- [16] T. Burton, D. Sharpe, N. Jenkins, and E. Bossanyi. *Wind Energy Handbook*. John Wiley and Sons, 2001.

- [17] S. Weitemeyer, N. Reinke, J. Peinke, and M. Hölling. Multi-scale generation of turbulence with fractal grids and an active grid. *Fluid Dynamics Research*, 45:061407, 2013.

Paper 4

Brief Communication: On the influence of vertical wind shear on the combined power output of two model wind turbines in yaw^a

JANNIK SCHOTTLER, AGNIESZKA HÖLLING, JOACHIM PEINKE and MICHAEL HÖLLING

Abstract. The effect of vertical wind shear on the total power output of two aligned model wind turbines as a function of yaw misalignment of the upstream turbine is studied experimentally. It is shown that asymmetries of the power output of the downstream turbine and the combined power of both with respect to the upstream turbine's yaw misalignment angle can be linked to the vertical wind shear of the inflow.

1 Introduction

Lately, different concepts of active wake control have been discussed throughout the research community. One promising concept is the wake deflection by intentional yaw misalignment of single wind turbines. The principle of deflecting the velocity deficit behind a wind turbine was observed in field measurements by [1], in wind tunnel experiments [2, 3] and in numerical simulations [4, 5, 6]. Further, [5] and [7] applied the concept to wind farm control strategies using large-eddy simulation (LES) methods, showing a potential power increase in wind farm applications.

[6] report on an asymmetric deflection of a turbine's wake with respect to its direction of yaw misalignment in numeric studies. Similarly, [8] found that a wake moves upwards or downwards depending on the direction of a yaw misalignment using PIV (particle image velocimetry) measurements behind a small turbine model. This observation is explained by an interaction of the wake's rotation and a pair of counter-rotating vortices formed in yawed conditions with the ground.

[6] studied the influence of atmospheric stabilities on the wake deflection by yaw misalignment. The results show that different stratifications do indeed result in varying deflections of the wake behind the rotor of a numeric turbine model. More precisely, disparities between wake deflections due to yaw misalignments of $+30^\circ$ and -30° were significantly different considering different atmospheric stratifications and thus different shears. It is believed that a combination of a vertical inflow gradient, the wake's rotation and the wind veer causes asymmetric wake deflections with respect to the rotor's yaw angle.

Examining the power of a turbine array, [9] and [5] showed that only one direction of yaw misalignment resulted in a power increase in a two-turbine array, while the exact opposite direction caused a power decrease. These observations were confirmed by [10] experimentally using two model wind turbines. As those findings impact the applicability of the concept significantly, the reasons for the asymmetry need to be understood. In this study, we show that vertical wind

^aPublished as JANNIK SCHOTTLER, AGNIESZKA HÖLLING, JOACHIM PEINKE and MICHAEL HÖLLING: Brief communication: On the influence of vertical wind shear on the combined power output of two model wind turbines in yaw, *Wind Energ. Sci.*, **2**, 439-442, 2017

shear has a direct effect on the power's asymmetry in two model wind turbines during yaw misalignment.

2 Methods

The experiments were performed in a wind tunnel of the University of Oldenburg, with an open test section of $1\text{ m} \times 0.8\text{ m} \times 5\text{ m}$ [$w \times h \times l$]. Two model wind turbines as described by [10] were used in streamwise displacement. The turbines were separated by $3D$, with $D = 0.58\text{ m}$ being the rotor diameter and rotation being clockwise when observed from upstream. The upstream turbine is placed on a turning table allowing for yaw misalignment, where a positive yaw angle is a counterclockwise rotation of the rotor when seen from above. The downstream turbine utilizes a partial load control and thus adapts to the changing inflow conditions. Power measurements are based on the rotational speed and the torque, being proportional to the electric current of the generator. Further details about the setup, power measurements and turbine control are described by [10]. In order to isolate the effect of vertical wind shear in the inflow, the horizontal axes of an active grid (see [11]) at the wind tunnel outlet were set statically to create two different inflow profiles, which were characterized prior to the experiments. Thirteen hot-wire probes were used simultaneously in a vertical-line arrangement with a distance of 75 mm separating two sensors. For both settings of the grid, data were recorded for 120 s at a sampling frequency of 2 kHz . The array was installed 1 m downstream from the grid at the position of the upstream turbine's rotor, which was installed after characterizing the inflow. Fig. 2.1 shows mean wind speeds over the height z , whereas $z = 0\text{ m}$ corresponds to the bottom of the wind tunnel outlet. The reproducibility of time-averaged velocity profiles for one grid setting has been investigated and confirmed. Further, mean values have been checked for statistical convergence. For the remainder of this paper, we refer to the inflow conditions shown in Fig. 2.1 as "profile 1" and "profile 2". Using two inflows which feature vertical wind shear of opposite direction over the rotor area allows for an investigation of the gradient's influence on the asymmetric power output of the two turbines with respect to the upstream turbine's yaw angle, γ_1 .

3 Results

Mean values of the upstream turbine's power P_1 , the downstream turbine's power P_2 and their sum P_{tot} are shown as a function of the yaw angle γ_1 in Fig. 3.1. Data points are normalized to the respective maximum of P_{tot} . Looking at Fig. 3.1a, asymmetries of P_2 and P_{tot} with respect to γ_1 become obvious during inflow profile 1. The minimum of the downstream turbine's power P_2 is shifted towards positive angles. The maximum of the combined power P_{tot} is at $\gamma_1 \approx -18^\circ$, being approx. 4% larger compared to the case of no yaw misalignment, $\gamma_1 = 0^\circ$. Also, the combined power shows a distinct asymmetry with respect to γ_1 . While the power is maximal at $\gamma_1 \approx -18^\circ$, it further decreases for larger values of γ_1 . For positive yaw angles, the total power output is smaller compared to the case of no yaw misalignment. The results support the

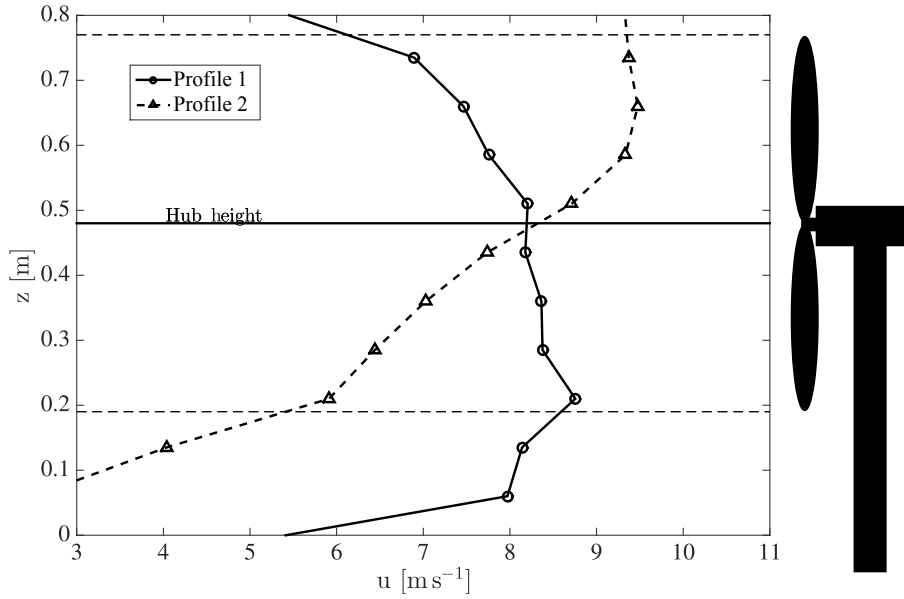


Figure 2.1: Mean velocity values of the vertical wind speed profiles 1 and 2 that were used as inflow conditions. The dashed, vertical lines mark the heights of the rotor tips of the turbine that was installed after characterizing the inflow profiles.

direction of a purposeful yaw misalignment being of great relevance regarding the application of this concept to wind farm control. Further, the general shape of the graphs is in good agreement with numeric simulations of full-size turbines reported by [5] and [9]. Figure 3.1b shows the results of the same experiment; nothing was changed in the setup, except for the inflow profile, which was changed to profile 2. Since the reproducibility of results was proven by [10], the effect of the changed inflow is isolated. As can be seen, asymmetric shapes of P_2 and P_{tot} are still observed. More importantly, the direction of the asymmetry changed with the direction of the inflow's vertical shear. Now, in Fig. 3.1b, the minimum of P_2 is located at negative yaw angles ($\gamma_1 \approx -4^\circ$). Moreover, the yaw angle direction at which the combined power is at a maximum changes, being positive ($\gamma_1 \approx 12^\circ$) for inflow profile 2. Our results show that the reason for the asymmetric shapes of the graphs in Fig. 3.1 is related to the inflow's vertical wind shear, which is further discussed in Sect. 4.

4 Discussion and conclusion

The vast majority of model wind turbine experiments face a Reynolds number mismatch between the laboratory and full-scale cases, which is nearly a factor of 170 in this study. However, due to the good agreement of the general shapes of the turbines' normalized powers comparing the present study and [10] with simulations of a full-scale case [9, 5], the Reynolds number dependence is assumed to be rather insignificant when judging general effects of wake deflection. It should be noted that the LES simulations performed in [9] and [5] include wind veer, which was not reproduced experimentally and should be kept in mind when comparing the numerical and

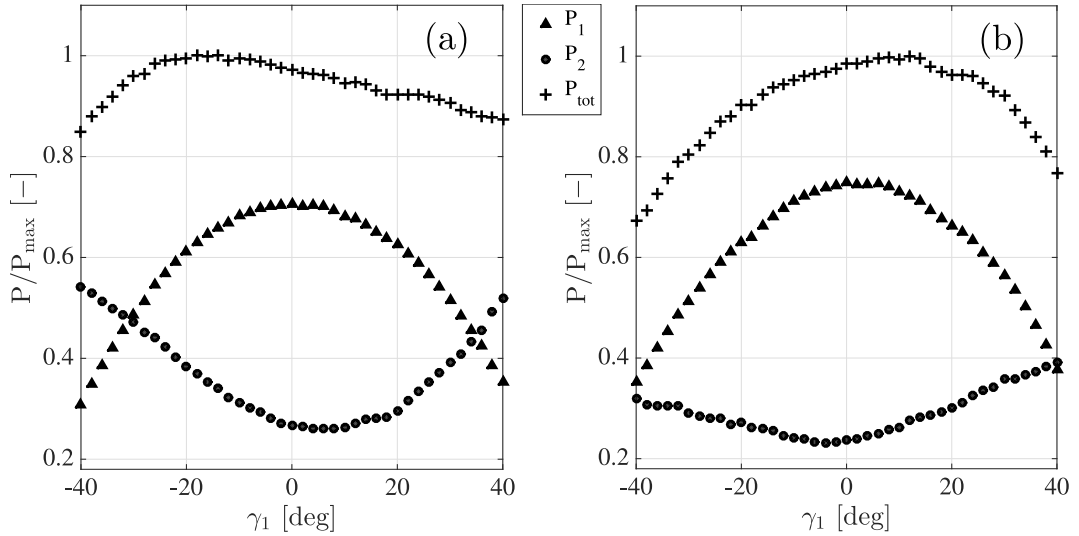


Figure 3.1: Mean values of P_1 , P_2 and P_{tot} for each examined value of γ_1 during the inflow condition profile 1 **(a)** and profile 2 **(b)**.

experimental studies. Further, due to spatial limitations of the wind tunnel, the profiles shown in Fig. 2.1 are not expected to be fully developed. Therefore, their downstream development, which was not investigated in this study, might impact the wake deflections. This effect could not be isolated. Next, the inflow profiles vary regarding their turbulence intensity. This is expected to impact the wake recovery [12] but not the asymmetries in power reported. It should also be noted that the upstream turbine's tip speed ratio (TSR) is not constant for varying angles γ_1 . As shown by [3], the TSR maximizing the power is subject to change with the yaw angle. Therefore, the load control utilized by the downstream turbine was not used for the upstream turbine, which was operated at constant electrical load for both profiles. However, as the upstream turbine's TSR is symmetric with respect to γ_1 , this is not expected to affect the asymmetries observed in this work.

This study investigates the influence of vertical wind shears on the power output of two aligned model wind turbines. An asymmetry of the power output with respect to the upstream turbine's yaw angle was found in prior experiments on a laboratory scale [10] as well as in full-scale numeric simulations [5, 9]. Only one direction of yaw misalignment resulted in a power increase, whereas the exact opposite direction caused a power decrease in the turbine array. For a potential application of active wake control by intentional yawing, this effect needs to be understood. With the present methods, we investigate the reasons for the asymmetric power output of a two-turbine array and isolate the effect of a vertical inflow gradient's orientation. A strong linkage between the asymmetry and the velocity gradient's orientation was found. If the reported asymmetry depends on boundary conditions of the surroundings, which our results suggest, then this drastically impacts the applicability to real-world wind farm control scenarios. In this study, the downstream turbine's power is used as indicator. The interesting results regarding the asymmetry and its linkage to the inflow conditions motivate further examinations, such as detailed wake measurements during different inflow gradients and yaw errors. As the yaw angle is a distribution in full-scale cases, future works should address this issue and its impact on active wake redirection strategies.

Bibliography

- [1] J.-J. Trujillo, J. K. Seifert, I. Würth, D. Schlipf, and M. Kühn. Full field assessment of wind turbine near wake deviation in relation to yaw misalignment. *Wind Energy Science Discussions*, (January):1–17, 2016.
- [2] D. Medici and P. Alfredsson. Measurements on a wind turbine wake: 3d effects and bluff body vortex shedding. *Wind Energy*, 9(3):219–236, 2006.
- [3] P.-Å. Krogstad and M. S. Adaramola. Performance and near wake measurements of a model horizontal axis wind turbine. *Wind Energy*, 15(5):743–756, 2012.
- [4] Á. Jiménez, A. Crespo, and E. Migoya. Application of a les technique to characterize the wake deflection of a wind turbine in yaw. *Wind energy*, 13(6):559–572, 2010.
- [5] P. M. O. Gebraad, F. W. Teeuwisse, J. W. van Wingerden, P. A. Fleming, S. D. Ruben, J. R. Marden, and L. Y. Pao. Wind plant power optimization through yaw control using a parametric model for wake effects-a CFD simulation study. *Wind Energy*, 19(1):95–114, jan 2014.
- [6] L. Vollmer, G. Steinfeld, D. Heinemann, and M. Kühn. Estimating the wake deflection downstream of a wind turbine in different atmospheric stabilities: an LES study. *Wind Energy Science*, 1(2):129–141, sep 2016.
- [7] P. A. Fleming, A. Ning, P. M. O. Gebraad, and K. Dykes. Wind plant system engineering through optimization of layout and yaw control. *Wind Energy*, 19(2):329–344, feb 2016.
- [8] M. Bastankhah and F. Porté-Agel. Experimental and theoretical study of wind turbine wakes in yawed conditions. *Journal of Fluid Mechanics*, 806(1):506–541, nov 2016.
- [9] P. Fleming, P. M. Gebraad, S. Lee, J.-W. Wingerden, K. Johnson, M. Churchfield, J. Michalakes, P. Spalart, and P. Moriarty. Simulation comparison of wake mitigation control strategies for a two-turbine case. *Wind Energy*, 2014.
- [10] J. Schottler, A. Hölling, J. Peinke, and M. Hölling. Wind tunnel tests on controllable model wind turbines in yaw. *34th Wind Energy Symposium*, (January):1523, 2016.
- [11] S. Weitemeyer, N. Reinke, J. Peinke, and M. Hölling. Multi-scale generation of turbulence with fractal grids and an active grid. *Fluid Dynamics Research*, 45:061407, 2013.
- [12] Y. T. Wu and F. Porté-Agel. Atmospheric turbulence effects on wind-turbine wakes: An LES study. *Energies*, 5(12):5340–5362, 2012.

Appendix

A: Software

A.1 Hierarchy

To control the model wind turbine(s) and record data, a National Instruments Compact RIO (cRIO-9074) system was used. A cRIO system consists of a real time processor (RT) and a fully programmable FPGA^a chip. Thus, the system can either run totally independent with software running on the FPGA chip and/or the RT or in connection with PC based software as done in this application. Figure A.1 shows the hardware hierarchy schematically, whereas arrows indicate data streams. The advantages of software running on the FPGA chip or on the RT are real time characteristics, thus determinism. This means that, up to a certain speed limit, loops run at desired rates that are not affected by disturbances as it would be the case for a PC/Windows application. In best-practice, time-critical software parts should be implemented on deterministic systems.

Data streams, can be implemented in numerous ways, which are well documented on the National Instruments website, www.ni.com. In the following, the principle implementation of the described hierarchy, data acquisition and turbine control are described.

A.2 Data acquisition

In the software environment LabView, a program is called Virtual Instruments (VI). The analog/digital conversion (analog I/O) as well as the measurement of the rotational speed of the turbine is implemented on the FPGA chip, allowing for a great programming flexibility. The FPGA-VI consists of two loops, one being responsible for measuring the rotational frequency, one for analog I/O and data streaming as described below. The generator of the model wind turbine is equipped with a magnetic encoder, whereas 1024 (hardware) edges correspond to one revolution. Two channels with a face shift of 90° are implemented, so that the output of the encoder are two rectangular signals, face shifted 90°. Counting rising and falling edges of both

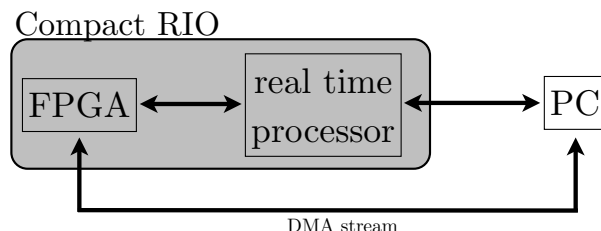


Figure A.1: Hierarchy of the software parts used to run the model wind turbine(s).

^aField Programmable Gate Array

channels results in 4096 counts per revolution of the main shaft. To count these digital signals, the hardware module NI-9401 is used, whose inputs are read in a *single cycle timed loop* on the FPGA chip, which is a loop running at the speed of the chip itself, which is 40 MHz. Per turbine, both channels A and B are read, whereas a change from logic 1 to 0 or vice versa within one loop iteration corresponds to a counter increment of one. The current counter value is stored within the scope of the VI in a local variable. A boolean local variable resets the current counter value to zero whenever being `true` for a maximum time of one loop iteration. A screen shot of the single cycle timed loop running on the FPGA to measure the rotational speed is shown in Figure A.2.

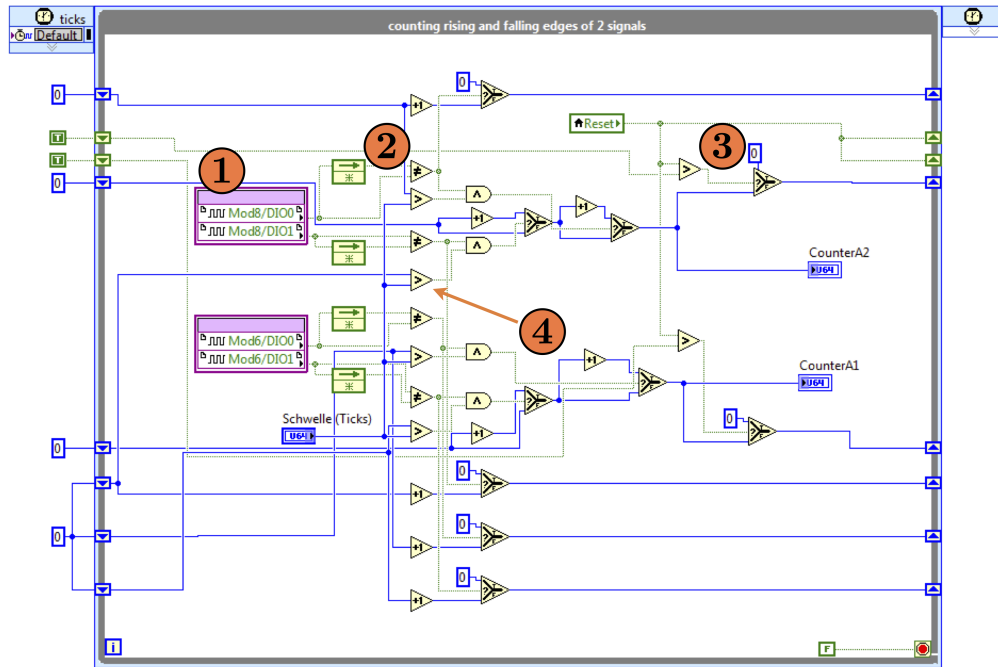


Figure A.2: Screen shot of the FPGA-VI: Single cycle timed loop to read the encoder signals.

The loop is set up for two model turbines, the following brief explanation is limited to one turbine:

- ① The digital lines of two channels are read, corresponding to channel A and B of the encoder.
- ② The actual counting process: The current state is compared to the state of the previous loop iteration, thus $1/40\text{MHz} = 2.5 \times 10^{-8}\text{s}$ ago. Whenever unequal, the counter is incremented. That way, rising *and* falling edges of the TTL signal are counted.
- ③ A local variable within the VI resets the current counter value whenever switched from `false` to `true`. The current counter value is stored in the indicator `CounterA1` or `CounterA2`, respectively, which correspond to both turbines when used simultaneously.
- ④ The main part of the counting process is implemented in steps 1)-3). Additionally, an approach called *debouncing* is applied, acting similar as a low pass filter. The time interval between two counts (two edges) is measured and compared to a threshold values specified

in the variable **Schelle(Ticks)**. The counter value is incremented only if the time interval between two counts is larger than the threshold. This value has to be set corresponding to the maximum expected rotational speed of the turbine. This way, counts that cannot originate from the turbines rotation (e.g. noise) are ignored. The unit of the threshold value is **ticks**, which is the loop iteration time of 2.5×10^{-8} s.

On the same VI on the FPGA, next to the loop shown in Figure A.2, a second loop is running at the speed specified by the user, corresponding to the sampling frequency of the analog signals. A screen shot is shown in Figure A.3, with the description below. The analog signals and the rotational frequency are measured at different rates, because the rotation speed has an upper limit regarding sampling frequency due to the limited rotational speed of the turbine. Furthermore, using a certain time interval and a counter of TTL pulses results in a trade off between measurement speed and accuracy. Generally, a sampling rate of 200 Hz for ω gave satisfying results throughout the experiments.

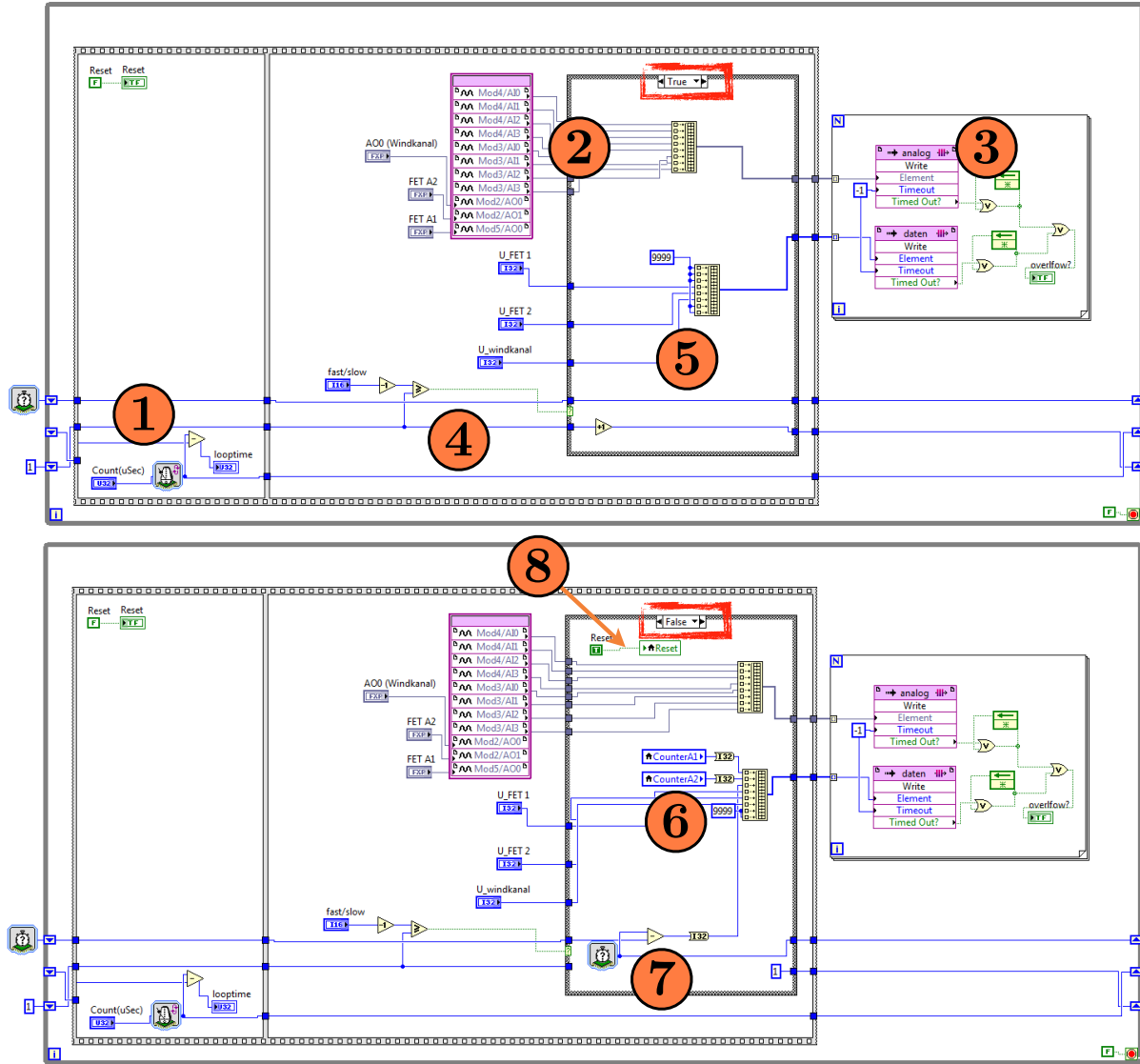


Figure A.3: Screen shot of the FPGA-VI: While loop running at the speed of analog sampling. Top and bottom screen shots correspond to both cases, **True** and **False**, of the case structure, indicated by the red box.

- 1 The loop rate and therewith the analog sampling frequency is specified in μs (loop time).
- 2 Analog I/O. Each loop iteration, one sample per channel are read, and output values are sent to the AO module. Input values are combined in a 1D array of Fixed-Point data type.
- 3 The analog values are sent in the FIFO^b DMA^c stream **analog**.
- 4 Analog signals are sampled faster than the rotational speed. The ratio of both sampling rates is the variable **fast/slow**. Every x loop iterations, the case structure switches, where x is the ratio **fast/slow**.

^bFirst In, First Out

^cDirect Memory Access

- 5 In the **True** case, on rotational speed values are recorded, thus **9999** is written to the array instead, while the counter in the since cycle timed loop is counting edges of the generator's encoder.
- 6 When the case structure switches to **False**, the current counter values from the single cycle timed loop, **CounterA1** and **CounterA2** are read through a local variable and written to a 1D array.
- 7 Additionally, the time elapsed since the last reading of counter values/reset is measured and stored in the array. Therewith, both parameters necessary for calculating the rotational speed, counter value and time interval, are available.
- 8 Whenever the counter values are read, they are reset by switching the local variable **Reset** to **True**, cf. Figure A.2, marker 3.

The described VI consisting of two loops runs on the FPGA target, streaming the analog samples, counter values and time intervals in two different FIFOs. These streams can be either read on the Real Time target or on a host PC. The latter was done in the majority of experiments throughout this thesis. Data processing, plotting, turbine control, data logging and many more aspects were also realized on the host PC. A principle example of accessing the two data streams on the host is shown in Figure A.4, the description follows below.

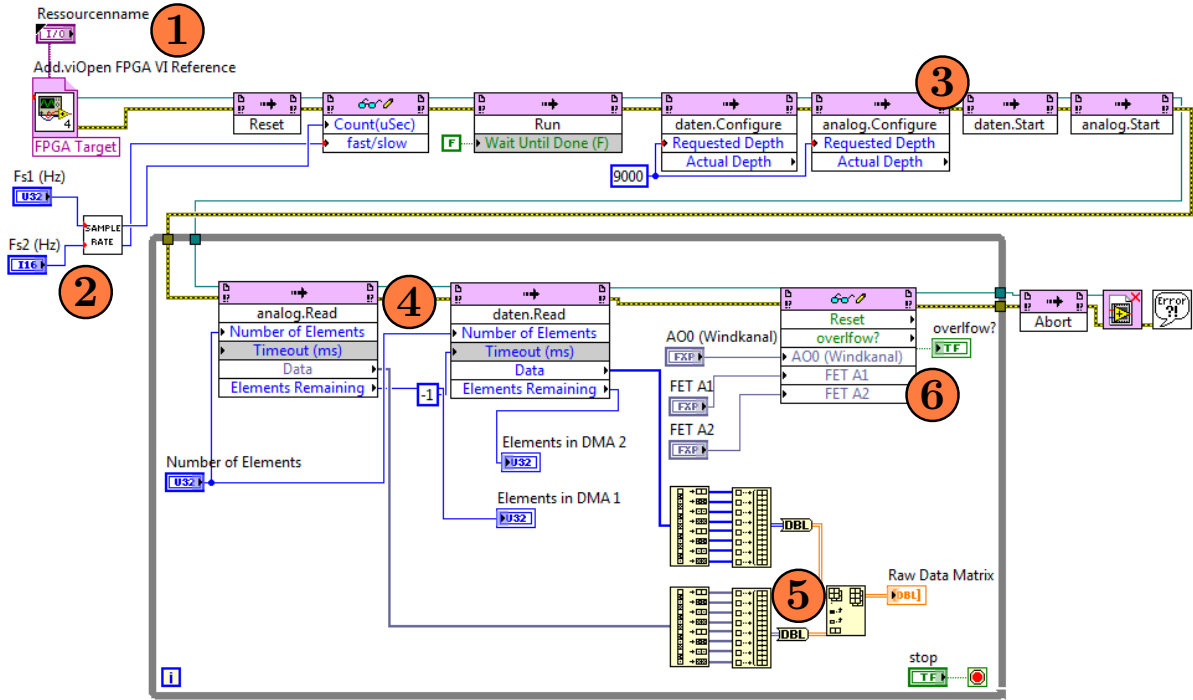


Figure A.4: Minimal code example of accessing the two data streams coming from the FPGA target. This principle example could run on the RT or the host PC.

- 1**: A reference to the FPGA-VI on the FPGA target is established before the VI is reset to default values.
- 2**: The rate of the loop as described in Figure A.3 is specified. Therefore, the sampling frequency of analog signals (F_{s1}) and the rotational frequency (F_{s2}) are converted to a loop time in μs and the ratio F_{s1}/F_{s2} . Thus, F_{s1} has to be a multiple of F_{s2} .
- 3**: After the FPGA-VI is run, both DMA streams are configured to a depth of 9000 samples before both streams are started outside the while loop.
- 4**: Both streams are read, whereas for each stream, as many samples as specified in the variable **Number of Elements** are read each loop iteration. Because the stream is a one dimensional array, it has to be kept in mind that per loop iteration on the FPGA-VI, 8 (in this example) samples are being sent to the stream. Thus, the **Number of Elements** specifies the number of time stamps (analog sampling rate) \times 8.
- 5**: Here the 8 values per time step are split again into the 8 channels. Both 1D arrays are combined into one 2D array, which is the matrix of raw data.
- 6**: Analog output values (here: AO0, (U_{FET1} and U_{FET2} , the latter two being the manipulated variables of the load controller as described in Section 2.2) are being sent to the FPGA-VI. After the while loop, the FPGA-VI is stopped, the reference closed and errors are displayed.

A.3 State machine architecture & application

For the characterization of the model turbine described in Chapter 3 as well as for the experiments performed **paper 3** and **paper 4**, a loop comprising a so-called state machine architecture is added to the host VI on the PC. A state machine programming architecture is useful whenever certain algorithms, “states” of the program, are repeated throughout execution. The principle is explained thoroughly at <http://www.ni.com/white-paper/3024/en/> and <http://www.ni.com/white-paper/2926/en/>. In the following, one simple application example is described.

During turbine characterization for the load control approach described in Section 3.5, torque- ω curves for a range of wind speeds need to be recorded. Thus, turbine data has to be recorded for a specified range of U_{FET} and $\langle u \rangle$. The program can now be divided in 6 different states:

1. Initializing.
Set up communication to the FPGA/RT, creating files, etc.
2. Wind tunnel.
Set the wind tunnel to the first/next velocity.
3. Changing U_{FET} .
Set the voltage U_{FET} to the first/next value, previously defined in state 1.
4. Data acquisition.
Turbine data are recorded for a previously specified time span and sampling rate.
5. Logging & plotting of the data.
6. Shut down.
Clearing the FPGA/RT connection, shutting down the wind tunnel, closing references, ending the program.

After state 2 and 3, a waiting time is implemented that accounts for inertia etc. and ensures a steady state operation. This principle can be extended arbitrarily, adding more variables to investigate, such as pitch or yaw angles. Figure A.5 shows a screen shot of the program’s front panel for turbine characterization, recording the torque- ω curves with a polynomial fit through the respective power maxima.

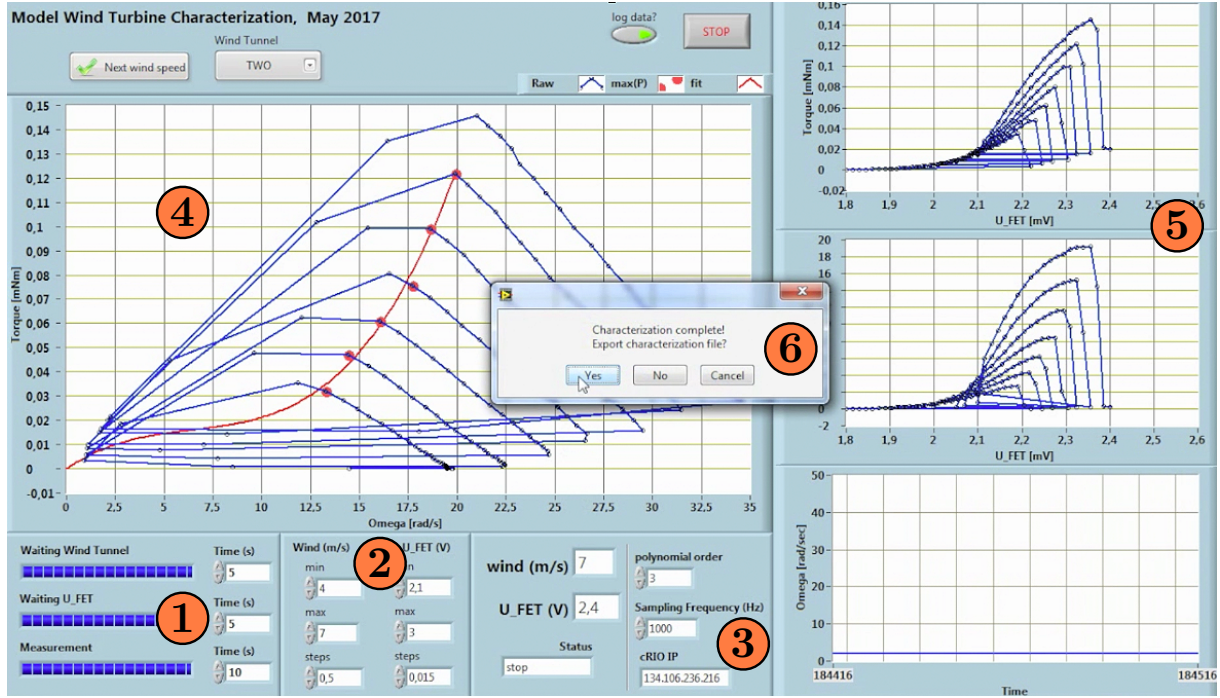


Figure A.5: Screen shot of the characterization software recording mean values of $T(\omega)$ for various wind speeds. A characterization file is exported for later use during turbine control.

- 1 Time spans fore waiting intervals after a change in wind speed or U_{FET} as well as measuring time can be specified. During execution, the time is displayed in the progress bar.
- 2 The range of wind speeds and voltages U_{FET} are specified by the minimum, maximum and step size.
- 3 The sampling frequency and the IP address for communication with the cRIO system are specified. At time of writing, the sampling frequency refers to the analog values, while the rotational speed is recorded at a rate of 200 Hz. Additionally, the order of a polynomial fit through the $c_{P,max}$ values (red circles) is specified.
- 4 Mean values of $T(\omega)$ are plotted (blue) for each wind speed and U_{FET} , maximum power values are marked by the red circles. A polynomial fit is shown in red.
- 5 Similarly to point 4, the upper graph shows $T(U_{FET})$, the lower graph $P(U_{FET})$.
- 6 After all data was recorded, a characterization file containing the coefficients of the polynomial fit can be exported. Another program for turbine control can simple input this file and the load control can be used.

It should be noted that when using only the FPGA (data acquisition, see Section A.2) and the PC, two separate loops are implemented on the host PC VI that run in parallel. One loop for reading the DMA streams as shown minimalistic in Figure A.4 and one loop encapsulating the state machine. Thus, during data acquisition state of the state machine, communication between the loop reading the DMA streams and the state machine loop has to be implementing.

Exemplary, data can be streamed from the DMA reading loop to the state machine, where **queues** would be recommended for lossless inter-loop communication. Another approach is to use also the Real Time target in addition to the FPGA chip and the PC, as illustrated in Figure A.1. This is done in the the program shown in Figure A.5. In the following, the state machine architecture of the characterization program is explained. Every state machine consists of a case structure in a while loop, whereas the states are switched every loop iteration. Before entering the loop, some references such as file paths are established as shown in Figure A.6:

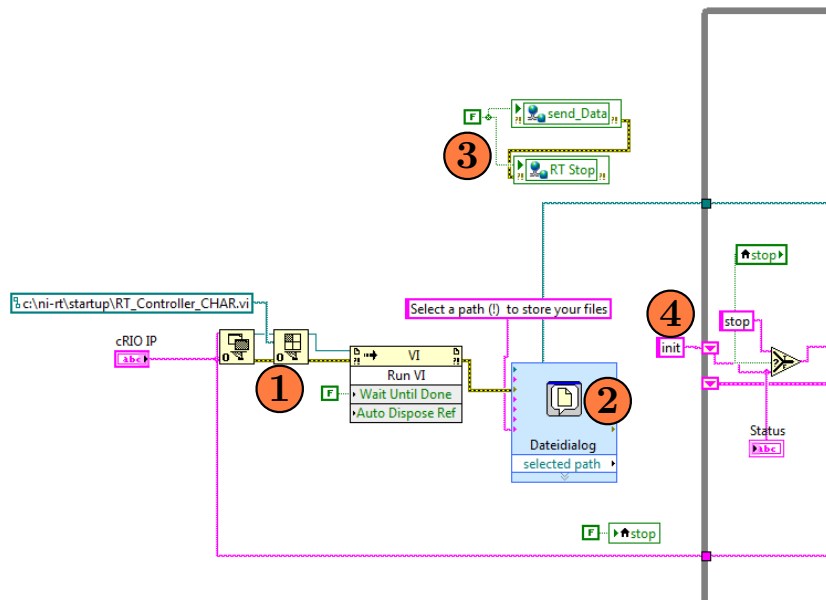


Figure A.6: Block diagram before the while loop containing the actual state machine structure.

- ① The VI on the real time target **RT_Controller_CHAR.vi** is started at first. This is where the DMA stream from the FPGA is read, similarly as shown in Figure A.4.
- ② A user prompt asks to select a file path (not a file) to store the measurement data in. Because this might take a certain time, it is carried out outside of the loop.
- ③ The boolean network variables **send_Data** and **RT_stop** are **false** in the beginning. They trigger the data streams from the RT to the host as well as loop termination, thus stopping the VI on the RT.
- ④ The first state of the state machine is **init**, entering the shift register of the loop. The state **init** is described in Figure A.7.

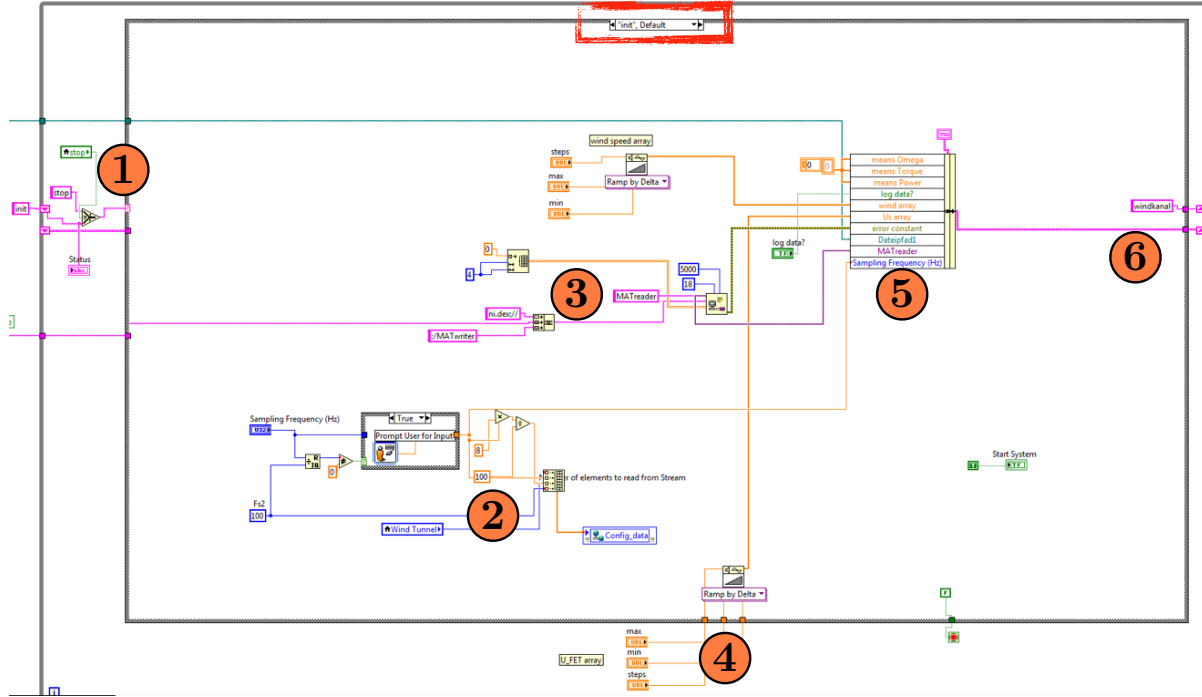


Figure A.7: The first state **init** of the state machine.

- ① Before entering the case structure, the **stop** variable is checked, which would execute the **stop** state instead of what is stored in the shift register, **init** in this case. As this is done outside the case structure, it is executed every loop iteration.
- ② Basic configurations such as sampling frequencies and wind tunnel selection are sent to the RT via a network variable. The ratio of both sampling rates is checked to be a multiple of 8. If violated, the user is informed and asked to correct the input.
- ③ Communication between RT and host is implemented by network streams, which are well documented on ni.com. Here the connection is established based on the RT's IP address.
- ④ The array of *UFET* values is created here. This is done outside the loop in order to adjust the range during execution. As the range of interest varies with wind speed, this saves a significant amount of time. A similar array is created for all wind speeds that should be investigated.
- ⑤ All variables of interest are stored in one cluster, that is looped throughout execution in a shift register. Here, default values are established. The setup of the cluster is done in the constant above the actual cluster, which can be expanded and edited. That way, only two shift registers are required in the state machine, increasing clarity.
- ⑥ Lastly, the next state is defined, which is **windkanal** here, setting the wind tunnel to the first speed of the array, which is shown in Figure A.8

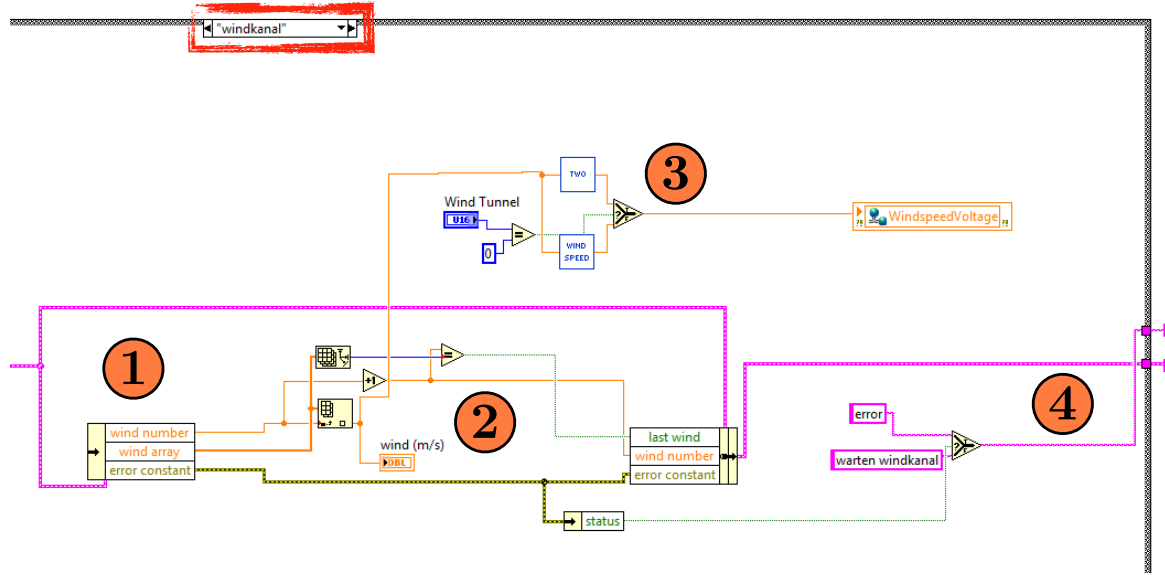


Figure A.8: The case `windkanal`, which sets the wind tunnel to the appropriate speed.

- ① From the array containing all variables, the array of wind speeds `wind_array`, the current index `wind_number` and the error cluster are accessed. All other variables remain in the cluster with their current value.
- ② The wind speeds array is accessed at the index, defining the desired wind speed. The index is increased afterwards. It is also checked whether the current wind speed is that last of the array, defining the boolean variable `last wind`.
- ③ The desired wind speed is converted to a voltage by the respective wind tunnel characteristic and then sent to the RT, from where the value is sent to the FPGA chip and ultimately to the analog output terminal of the respective module.
- ④ Lastly, the error cluster is checked for errors, defining the next state to be either `error` or `warten windkanal`. The latter is simply a waiting time allowing for the wind tunnel to reach the desired speed. The case is not further described. It follows the case `Us einstellen`, which sets the voltage U_{FET} of the model turbine.

The case `Us einstellen` is not explained because it is very comparable to the `windkanal` case. After another waiting time allowing for the turbine to adjust the point of operation, the data acquisition is performed in the case `messung`, explained in Figure A.9

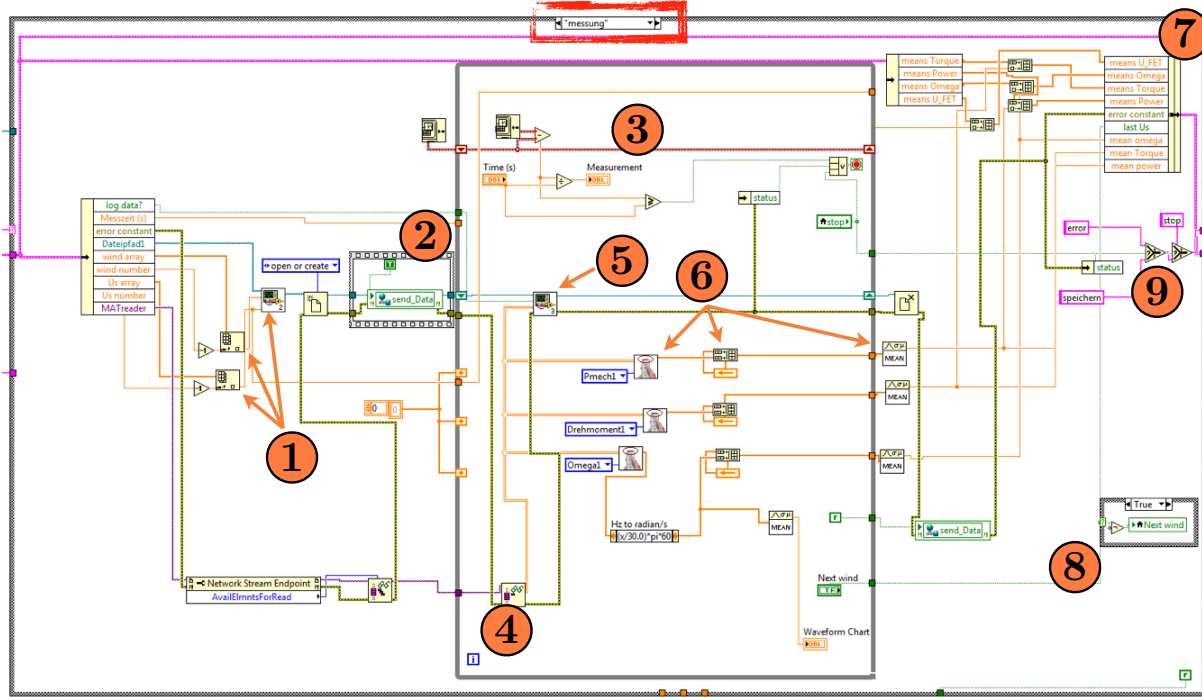


Figure A.9: The state **messung**, performing data acquisition.

- ① The subVI creates a new file path within the directory chosen in the beginning. The file name is based on the current wind speed and U_{FET} value and is used for logging the time series of each combination in a separate file.
- ② The **send_Data** boolean is set to **true**, triggering the data stream from the RT to the host.
- ③ Using a shift register, the time stamp before the measurement loop is compared with the time stamp within each loop iteration. The elapsed time is compared with the defined time of measurement for each configuration. After the time elapsed, the measurement loop is stopped. It is also stopped during an error occurrence and if the **stop** boolean is true.
- ④ Here, the raw data matrix is streamed from the RT in a network stream that was established in the **init** case.
- ⑤ The subVI logs the raw data as it is in the file created in point ①.
- ⑥ The subVI extracts the 1D array of a chosen parameter (here: power, torque („Drehmoment“) and rotational speed ω). The array fetched each loop iteration is added to the previous array, resulting in one array containing the data of each parameter at the end of the measurement loop. After the loop, that array is averaged to one mean value of that particular configuration of wind speed and U_{FET} .
- ⑦ The mean values are added to arrays of all mean values of previous configurations.
- ⑧ Within the measurement loop, the user has the opportunity to make the current configuration the last measured value of U_{FET} , jumping straight to the next wind speed. This saves time when the turbine already stalled and no higher values of U_{FET} are of interest. Accordingly, the boolean **last Us** becomes **true**.

- 9 As usual, it is checked for errors, jumping to the error state of the next state **speichern**, where mean values are logged and plotted. This is shown in Figure A.10. Additionally, the **stop** variable is checked.

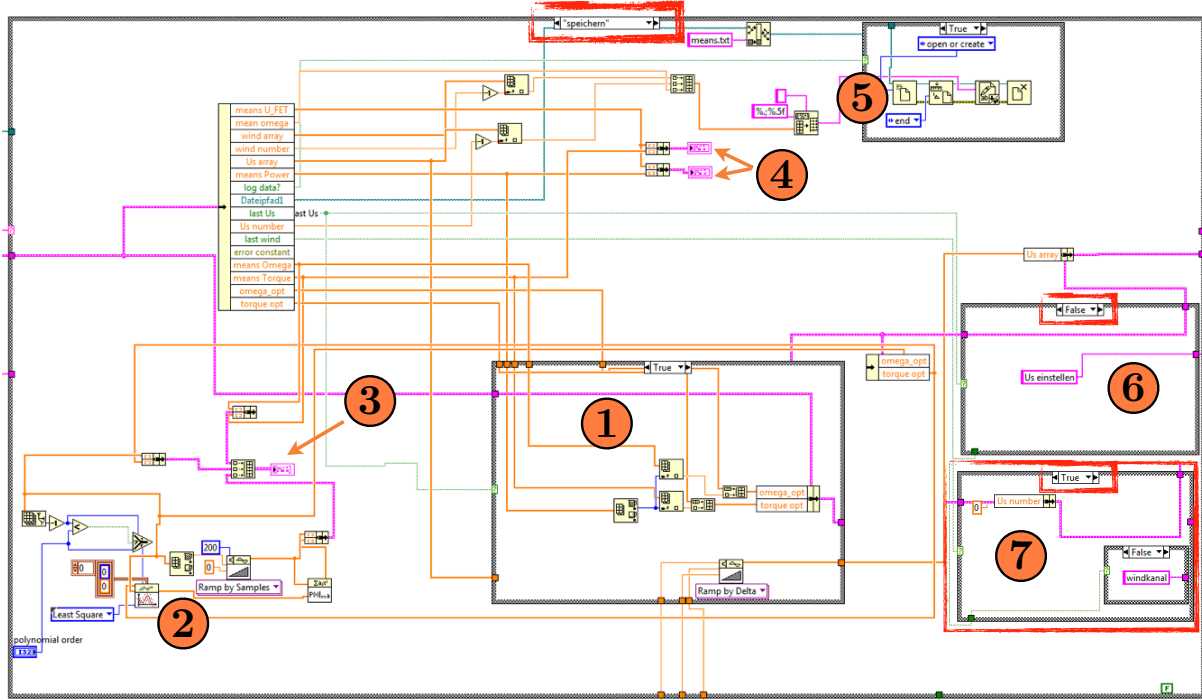


Figure A.10: The state **speichern**, performing data logging and plotting.

- 1 In case the previous measurement was for the last values of U_{FET} , the current array of mean power values is checked for its maximum. Thus, for each wind speed, the respective mean values of ω and torque maximizing the power are stored in the arrays **omega_opt** and **torque_opt**.
- 2 The data points contained in the arrays **omega_opt** and **torque_opt** (Torque- ω curve) are fitted by a polynomial of the order specified in the control **polynomial_order**. Order 3 gave good results, cf. Figure A.5.
- 3 Data of interest (Torque- ω curves) are plotted as shown in Figure A.5.
- 4 Further data visualization, cf. Figure A.5, marker 5.
- 5 The mean values are logged in a separate file **mean.txt** within the same directory as the time series.
- 6 The boolean **last Us** is checked. If **false**, the next case is **Us einstellen**, setting U_{FET} to the next value until the last is reached. The respective **true**-case is shown below.
- 7 If **last Us** is **true**, the index of the U_{FET} array is reset to zero. Further, the wind speed index is checked to be the last one and a similar principle is executed as previously described, resulting in setting the wind tunnel to the next speed or finishing the program with the state **stop**, explained in Figure A.11.

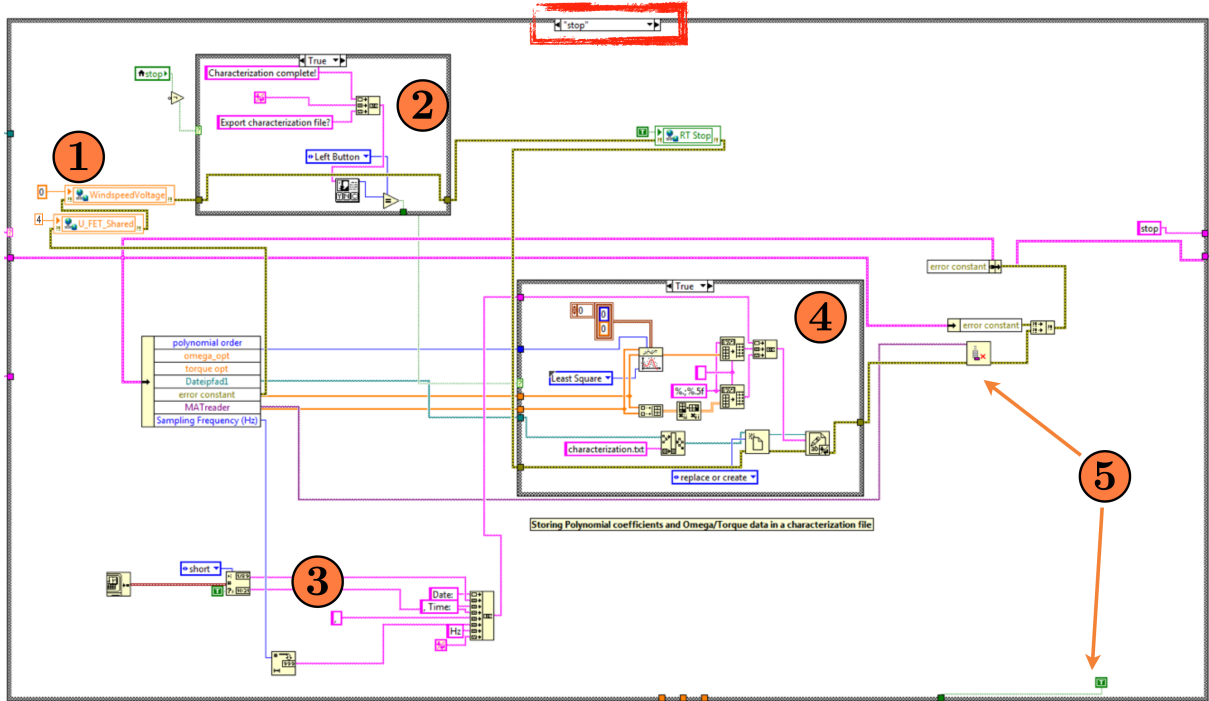


Figure A.11: The state `stop`, performing the shut down of the program, the turbine and the wind tunnel.

- ① At first, the wind tunnel is shut down and the voltage U_{FET} set to 4V, breaking the turbine as much as possible.
- ② The user gets informed that the characterization is complete (or aborted) and is asked if a characterization file should be exported.
- ③ The header of this characterization file is created here, including the time and date as well as the sampling rate.
- ④ Data the polynomial fit is based on, thus the arrays `omega_opt` and `torque_opt` are logged as well as the coefficients of the polynomial fit.
- ⑤ The network stream reference is cleared and the loop termination boolean set to `true`, stopping the while loop containing the case structure.

B: Blade specifications

The rotor blades of the model wind turbines are made of an SD-7003 airfoil, which was specifically designed for low Reynolds number operation. A detailed documentaiton is given by Selig et al. [1] and Counsil et al. [2]. Figure B.1 shows the airfoil's shape, while the respective coordinates are listed in Table B.2. Polars computed by Xfoil^a for Reynolds numbers of $Re = 5 \times 10^4$ and $Re = 10 \times 10^4$ are shown in Figure B.2. Assuming a TSR of $\lambda = 6$ at a mean velocity of $u_\infty = 8 \text{ m s}^{-1}$, the chord based Reynolds number at the blade tips is $Re_{\text{tip}} \approx 6.4 \times 10^4$.

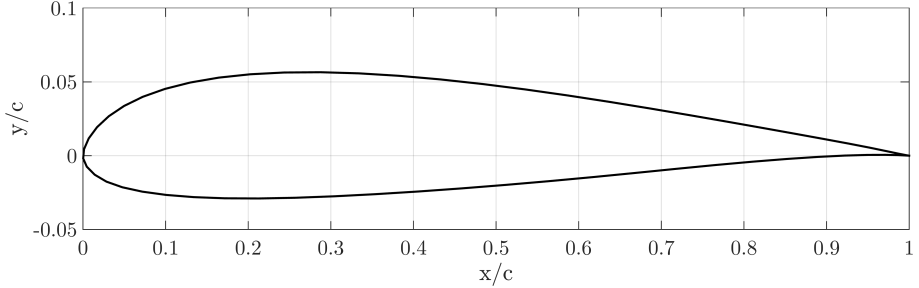


Figure B.1: Shape of the SD-7003 airfoil used for the model wind turbines. c is the chord length.

^aIn the simulation setup, the Mach number was 0 and $N_{crit} = 9$, which is a Xfoil specific parameter, being the logarithm of the amplification factor of the most-amplified frequency which triggers transition. Simply spoken, it quantifies the disturbance of the inflow. A value of 9 is used for an average wind tunnel.

Blade element	radius [mm]	chord [mm]	twist angle [°]
1	0	3.88	0.00
2	10	18.22	0.19
3	20	24.34	0.45
4	30	28.32	0.76
5	40	31.21	0.97
6	50	33.46	1.22
7	60	35.32	1.50
8	70	36.96	1.83
9	80	38.52	2.18
10	90	40.04	2.58
11	100	41.59	3.05
12	110	43.22	3.58
13	120	44.96	4.17
14	130	46.83	4.79
15	140	48.86	5.57
16	150	51.06	6.48
17	160	53.46	7.41
18	170	56.04	8.58
19	180	58.75	9.85
20	190	61.57	11.27
21	200	64.47	12.93
22	210	67.23	14.76
23	220	69.53	16.70
24	230	68.68	18.53
25	240	51.24	21.94

Table B.1: Blade geometry data of the model wind turbine.

x/c	y/c (suction side)	x/c	y/c (pressure side)
0.00127	0.00438	0.00025	-0.00186
0.00697	0.01172	0.00457	-0.00741
0.01702	0.01932	0.01408	-0.01285
0.03130	0.02677	0.02839	-0.01759
0.04978	0.03372	0.04763	-0.02141
0.07244	0.03993	0.07182	-0.02438
0.09921	0.04526	0.10073	-0.02660
0.12993	0.04961	0.13407	-0.02809
0.16442	0.05292	0.17150	-0.02888
0.20240	0.05518	0.21268	-0.02900
0.24358	0.05639	0.25719	-0.02852
0.28760	0.05658	0.30456	-0.02752
0.33405	0.05581	0.35426	-0.02608
0.38250	0.05415	0.40572	-0.02428
0.43249	0.05171	0.45837	-0.02217
0.48350	0.04859	0.51161	-0.01980
0.53499	0.04494	0.56484	-0.01723
0.58641	0.04086	0.61748	-0.01450
0.63717	0.03649	0.66898	-0.01167
0.68673	0.03197	0.71883	-0.00887
0.73449	0.02744	0.76644	-0.00628
0.77985	0.02304	0.81118	-0.00403
0.82224	0.01884	0.85241	-0.00220
0.86112	0.01494	0.88957	-0.00082
0.89600	0.01139	0.92210	0.00008
0.92639	0.00824	0.94952	0.00052
0.95193	0.00547	0.97134	0.00057
0.97235	0.00310	0.98718	0.00037
0.98745	0.00132	0.99679	0.00011
0.99681	0.00031	1.00001	0.00000
1.00000	0.00000	0.00000	0.00000

Table B.2: Coordinates of the SD-7003 airfoil. c is the chord length.

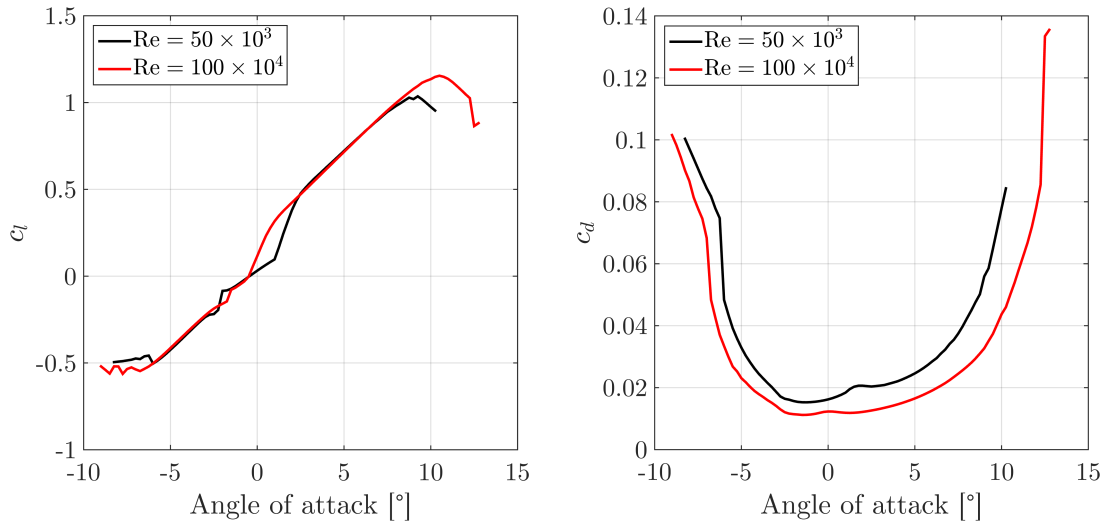


Figure B.2: Polars of the SD-7003 airfoil for $Re = 5 \times 10^3$ and $Re = 100 \times 10^4$ computed with XFOIL.

Bibliography

- [1] M. S. Selig and B. D. McGranahan. Wind Tunnel Aerodynamic Tests of Six Airfoils for Use on Small Wind Turbines. *Journal of Solar Energy Engineering*, 126(4):986, 2004.
- [2] J. N. Counsil and K. Goni Boulama. Low-reynolds-number aerodynamic performances of the naca 0012 and selig–donovan 7003 airfoils. *Journal of Aircraft*, 50(1):204–216, 2013.

C: Technical drawings

Technical drawings of the model wind turbine are shown in Figure C.1. It should be noted that the four-pole support structure was only used in **paper 2** to increase the hub height. Further C.2 shows the technical drawing of the NTNU turbine used for the experiments in **paper 2**.

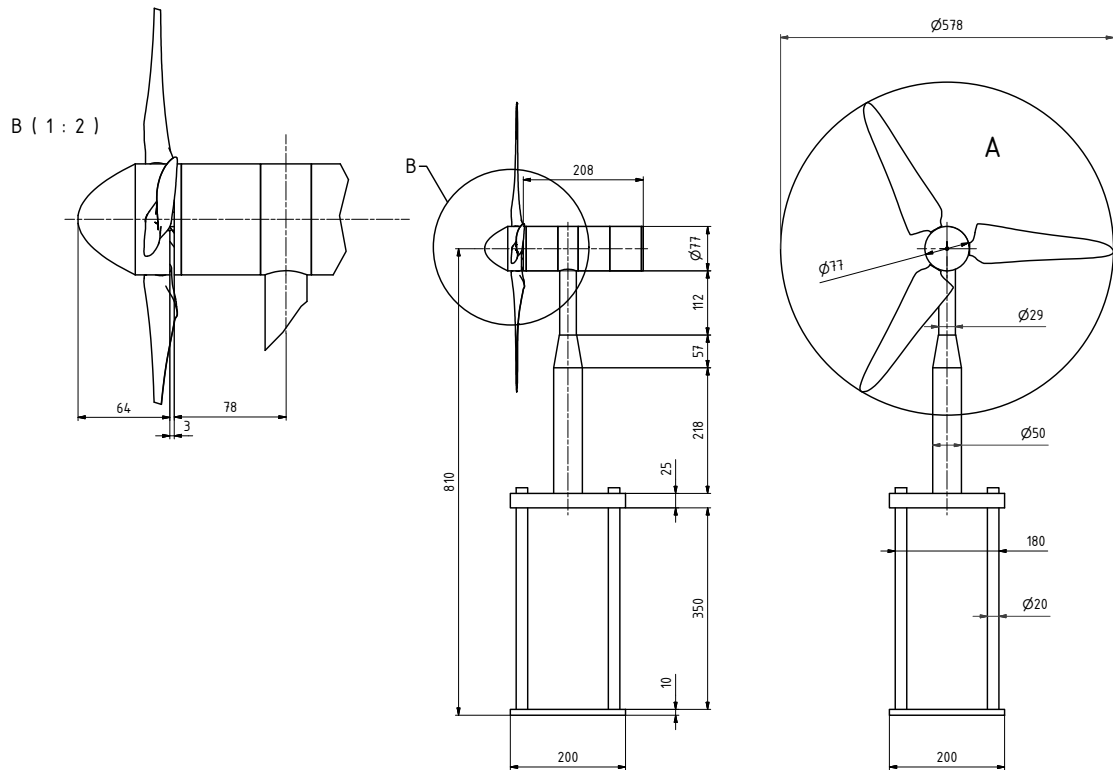


Figure C.1: Technical drawings of the model wind turbine. The four-pole support structure was used in **paper 2** only. Values in mm.

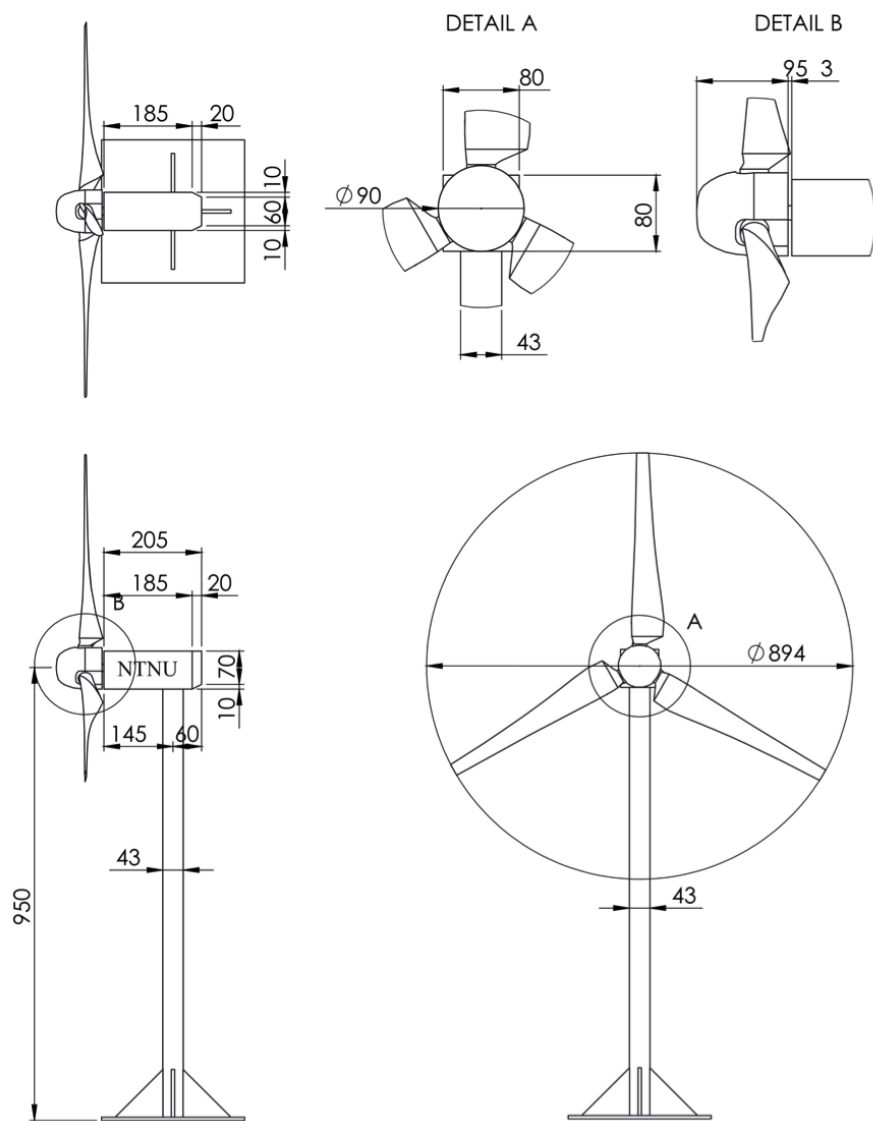


Figure C.2: Technical drawing of the NTNU turbine used in **paper 2**. Values in mm.

Acknowledgements / Danksagung

Beim gesamten Team von ForWind in Oldenburg möchte ich mich für die gute Zusammenarbeit und die schöne Zeit bedanken. Besonders gilt dies für die Arbeitsgruppe Turbulenz, Windenergie & Stochastik für das Aufnehmen in die Gruppe, für die ständige Bereitschaft zur Hilfe und zur Unterstützung sowie für das angenehme Miteinander, innerhalb und außerhalb der Universität. Ebenfalls möchte ich mich für die Möglichkeit bedanken, an diversen internationalen Konferenzen und Forschungsaufenthalten teilzunehmen.

Bei Prof. Dr. Joachim Peinke bedanke ich mich für das Ermöglichen dieser Arbeit. Vielen Dank für das Vertrauen, für die vielen inspirierenden Diskussionen und für die Sichtweise über den Tellerrand hinaus. Auch die Freiheit, meine eigenen Ideen verfolgen und umsetzen zu können, habe ich immer sehr geschätzt. Vielen Dank.

Ein großes Dankeschön an Dr. Michael Hölling für die Betreuung meiner Arbeit, für die vielen kritischen Anregungen und Einschätzungen in diversen Gesprächen und Diskussionen sowie für die Motivation. Ohne all das, hätte ich wohl nie eine Promotion begonnen.

I would like to thank Prof. Dr. Raúl Bayoán Cal for the time and willingness to evaluate this thesis as second reviewer. Thank you!

A special thanks to Jan Bartl, Franz Mühle and Prof. Dr. Lars Sætran for the hospitality and the great times we had in Trondheim, in and out the wind tunnel. It was great working with you and sharing the experience of being a phd student. Keep up the good work ☺!

I want to thank Dr. Jonathan Whale for the hospitality at Murdoch University in Perth, which was very inspiring.

Recht herzlich bedanken möchte ich mich bei dem Vorstand sowie dem Kuratorium der Reiner Lemoine Stiftung. Vielen Dank für das mir entgegengebrachte Vertrauen, für die finanzielle Förderung dieser Arbeit, für all die Inspiration sowie nicht zuletzt für die persönliche, familiäre Atmosphäre. Auch ein großer Dank an Lutz Plöttner für das unkomplizierte Begleiten durch die Zeit des Stipendiums. Danke!

Vielen Dank an Frederik Berger und Dr. Michael Hölling für die Zeit und für die Bereitschaft, Teile dieser Arbeit auf sprachliche und inhaltliche Fehler hin zu überprüfen.

Nicht zuletzt ein großer Dank an meine Familie und Freunde für die Unterstützung, für den Rückhalt, für den Ruhepol zu Hause und die sicherlich gesunde „Machst dat schon“ - Einstellung.

Curriculum

Personal information:

Name Jannik Schottler
Birthday 12 May 1989
Place of birth Bad Segeberg
Citizenship German

Education and scientific experience:

- 03/2015 – present Doctoral scholarship holder, Reiner Lemoine Stiftung
- 01/2015 – present Doctoral candidate, ForWind - Center for Wind Energy Research
University of Oldenburg
- 10/2012 – 10/2014 Master's degree, Engineering Physics, University of Oldenburg
M. Sc.
- 08/2011 – 01/2012 Renewable Energy Engineering, Murdoch University, Perth, Australia
- 10/2009 – 02/2013 Bachelor's degree, Engineering Physics, University of Oldenburg
B. Eng.
- 07/2005 – 08/2006 Chesterton High School, Chesterton, IN, USA
- 08/1999 – 08/2008 Städtisches Gymnasium Bad Segeberg
Abitur

Erklärung

Ich erkläre hiermit, dass

- eine Promotion zum Dr. rer. nat. angestrebt wird,
- ich diese Arbeit selbständig verfasst und nur die angegebenen Hilfsmittel benutzt habe,
- die Dissertation in Teilen bereits veröffentlicht ist, wie in der Publikationsliste dargestellt,
- diese Dissertation weder in ihrer Gesamtheit noch in Teilen einer anderen Hochschule zur Begutachtung in einem Promotionsverfahren vorliegt oder vorgelegen hat,
- ich die allgemeinen Prinzipien wissenschaftlicher Arbeit und Veröffentlichungen, wie sie in den Leitlinien guter wissenschaftlicher Praxis der Carl von Ossietzky Universität Oldenburg festgelegt sind, befolgt habe,
- im Zusammenhang mit dem Promotionsvorhaben keine kommerziellen Vermittlungs- oder Beratungsdienste (Promotionsberatung) in Anspruch genommen worden sind.

.....

(Jannik Schottler)

List of publications

Peer-reviewed journal publications

JANNIK SCHOTTLER, NICO REINKE, AGNIESZKA HÖLLING, JONATHAN WHALE, JOACHIM PEINKE, MICHAEL HÖLLING: On the impact of non-Gaussian wind statistics on wind turbines – an experimental approach, *Wind Energ. Sci.*, **2**, 1-13, 2017

JANNIK SCHOTTLER, JAN BARTL, AGNIESZKA HÖLLING, LARS SÆTRAN, JOACHIM PEINKE, MICHAEL HÖLLING: Wind tunnel experiments on wind turbine wakes in yaw: redefining the wake width, *Wind Energ. Sci.*, **3**, 257-273, 2018

JANNIK SCHOTTLER, AGNIESZKA HÖLLING, JOACHIM PEINKE, MICHAEL HÖLLING: Brief Communication: On the influence of vertical wind shear on the combined power output of two model wind turbines in yaw, *Wind Energ. Sci.*, **2**, 439-442, 2017

Conference proceedings

JANNIK SCHOTTLER, AGNIESZKA HÖLLING, JOACHIM PEINKE, MICHAEL HÖLLING: Wind tunnel tests on controllable model wind turbines in yaw, *34th Wind Energy Symposium*, **1523**, 2016

JANNIK SCHOTTLER, AGNIESZKA HÖLLING, JOACHIM PEINKE, MICHAEL HÖLLING: Design and implementation of a controllable model wind turbine for experimental studies, *Journal of Physics: Conference Series*, Vol. 753, No. 7, 2016

JANNIK SCHOTTLER, FRANZ MÜHLE, JAN BARTL, JOACHIM PEINKE, MUJIWA ADARAMOLA, LARS SÆTRAN, MICHAEL HÖLLING: Comparative study on the wake deflection behind yawed wind turbine models, *Journal of Physics: Conference Series*, Vol. 854, No. 1, 2017

Additional publications

HAUKE HÄHNE, JANNIK SCHOTTLER, MATTHIAS WÄCHTER, JOACHIM PEINKE, OLIVER KAMPS: The footprint of atmospheric turbulence in power grid frequency measurements, *Europhysics Letters*, in review, 2017

JAN BARTL, FRANZ MÜHLE, JANNIK SCHOTTLER, LARS SÆTRAN, JOACHIM PEINKE, MUWIWA ADARAMOLA, MICHAEL HÖLLING: Wind tunnel experiments on wind turbine wakes in yaw: Effects of inflow turbulence and shear, *Wind Energ. Sci.*, **3**, 329-343, 2018

INGRID NEUNABER, JANNIK SCHOTTLER, JOACHIM PEINKE, MICHAEL HÖLLING: Comparison of the Development of a Wind Turbine Wake Under Different Inflow Conditions, *Progress in Turbulence VII - Proceedings of the iTi Conference in Turbulence 2016* (pp. 177-218), Springer Proceedings in Physics 196, 2017

FRANZ MÜHLE, JANNIK SCHOTTLER, JAN BARTL, ROMAIN FUTRZYNSKI, STEVE EVENS, LUCA BERNINI, PAOLO SCHITO, MARTÍN DRAPER, ANDRÉS GUGGERI, ELEKTRA KLEUSBERG, DAN S. HENNINGSON, MICHAEL HÖLLING, JOACHIM PEINKE, MUWIWA SAMUEL ADARAMOLA, LARS SÆTRAN: Blind test comparison on the wake behind a yawed wind turbine, in preparation for *Wind Energy Science*, 2018

VLAHO PETROVIC, JANNIK SCHOTTLER, MICHAEL HÖLLING, MARTIN KÜHN: Wind tunnel validation of a closed loop active power control for wind farms, in preparation for *Journal of Physics: Conference Series*, 2018